



Exploring the surface properties of the liquid metals

A thesis submitted in fulfilment of the requirements for the degree of Doctor of Philosophy

Ali Zavabeti

Bachelor of Telecommunications Engineering (with Honours), Monash University

Master of Engineering Science (Research), Monash University

School of Engineering

College of Science, Engineering and Health

RMIT University

October, 2018

Abstract of Thesis

Gallium based liquid metal alloys feature unique properties that set promising pathways for developing future technologies. In contrast to mercury, gallium is considered a non-hazardous option as a liquid metal. A variety of metals can be alloyed into gallium in order to create mixtures with exciting physical and chemical properties. Galinstan is a eutectic liquid metal alloy, consisting 68.5 wt% gallium, 21.5 wt% indium, and 10 wt% tin which possesses a lower (below 0 °C) freezing point and higher surface tension than that of gallium liquid metal. Surface tension manipulations of liquid metals in electrolyte environments play an important role in the development of their emerging applications in electrochemical systems and microfluidics. However, the effects of electrolytes on the surface tension of liquid metals were not fully explored and an opportunity existed for a comprehensive study of such liquids. Due to significant potential outcomes, exploring the effects of different electrolyte types and concentrations on gallium based liquid metal dynamics was chosen as one of the main foci of this research. In this PhD thesis, the author establishes a new framework to study the effects of different acidic and basic electrolytes on dynamics of galinstan droplets. The droplet is placed in a recess between two microfluidic channels. Each of the channels carries different acidic and basic electrolytes to induce pH gradient across the droplet. Adjusting pH gradient by changing the concentrations of electrolytes on either side of droplets is shown to change the potential of zero charge and the chemical potentials. The author of this thesis hypothesises that according to the Lippmann's equation this condition should induce surface tension gradient to the droplet. The PhD candidate observes two distinct dynamics of deformation and surface Marangoni flow. To measure the deformation, the author mathematically modelled the change in shape as an

aspect ratio between major and minor axes. The surface Marangoni flow is measured by adding micro particles to the electrolytes and tracking their velocities on the surface of the droplet. When low concentrations of electrolytes are used, the hydroxides are less dominant on the surface to enable the deformation of the liquid metal. Instead, when concentrations of both acidic and basic electrolytes are increased, the surface hydroxides are thickened. The formation of thicker surface hydroxides leads to less droplet deformability. Under this condition, the surface tension gradient appears mostly as surface Marangoni flows. The deformation and surface Marangoni flows are replicated and characterised by applying external potentials. The PhD candidate derives theoretical equations for both dynamics which are in good agreement with the experimental results. The author also became involved in the development of applications in low pH gradients when the deformation is the more dominant dynamic. The author discovers that under the deformation dominant conditions, self-propulsion of the droplets is possible. Applications including pumping and switching are demonstrated by only changing the electrolytes surrounding the droplet without the need for an external power supply.

After investigating the surface manipulation of liquid metals using electrolyte environments, this PhD research is extended to explore the fundamental understanding of the oxide compounds that form on the surface of gallium liquid metals. In ambient conditions, self-limiting layers of metal oxides spontaneously form on the surface of liquid metal alloys. These oxide layers are naturally occurring two-dimensional (2D) materials. The author of this PhD thesis demonstrates two novel methods for delaminating the surface oxides. In the first method, surface oxides are directly transferred onto a substrate *via* a van der Waals exfoliation technique. In the second method, a reactor is devised for the large scale production of the 2D sheets. During this process, compressed air is injected into the liquid metal and the 2D exfoliated sheets are collected in a solvent that is situated above the liquid metal. PhD candidate then investigates the possibility of modifying the composition of the surface oxides. To achieve this, the author of the thesis uses galinstan liquid metal as a reaction solvent and incorporates other metals, such as transition metals, post transition metals and lanthanides. The author hypothesised that the surface oxide composition is dominated by the metal

oxide with more favourable Gibbs energy of oxide reaction in comparison to the base alloy. Author uses this method to synthesise the thinnest ever reported 2D hafnium oxide sheets and develops insulating layers for applications in electronics.

In the final stage of this PhD project, the author of this PhD thesis furthers this concept to grow low dimensional materials at the interface of galinstan liquid metal with water molecules. 2D sheet and One-dimensional (1D) fibre morphologies of aluminium oxide compounds are successfully produced by exposing galinstan-aluminium alloy to liquid and vapour phases of water molecules, respectively. Annealing is shown to retain both 1D and 2D morphologies when aluminium oxide hydroxides are converted into aluminium oxides. Both 1D and 2D oxide hydroxides of aluminium feature very large surface areas. The author demonstrates that each of the morphologies have exciting and unique characteristics. 1D morphologies that are grown from the surface of liquid metal are presented to have high transparency. Instead, the 2D grown morphologies are of strong stiffness. Freestanding membranes are made from the self-assembled 2D structures for the filtration of lead contaminated water and oil-water separation. Membranes demonstrate extraordinary high flux rates which author believes to be due to the highly wrinkled structures of the 2D sheets. A green and sustainable synthesis method is presented to reuse liquid metal for many synthesis cycles. The synthesis cycle is shown to repeat several times with negligible loss of liquid metal and a yield of 100%. The synthesis cycles are shown to only require aluminium and water as pre-cursors.

Altogether the author successfully demonstrates several significant discoveries in the course of this PhD research, developed new concepts based on liquid metals and also created a few unique devices with extraordinary properties. It is expected that the outcomes of this PhD research to impact future of many industries including electronics, optics and also filtration.

Declaration

I certify that except where due acknowledgement has been made, the work is that of the author alone; the work has not been submitted previously, in whole or in part, to qualify for any other academic award; the content of the thesis is the result of work which has been carried out since the official commencement date of the approved research program; any editorial work, paid or unpaid, carried out by a third party is acknowledged; and, ethics procedures and guidelines have been followed.

I acknowledge the support I have received for my research through the provision of an Australian Government Research Training Program Scholarship.

Ali Zavabeti

October 2018

Acknowledgements

This PhD thesis would not have been possible without the support of all the great people involved in my research. I would like to thank the Australian government for the Australian postgraduate award (APA) and school of engineering at RMIT University for the top up scholarship award. I would like to acknowledge Australian research council (ARC) centre for future low-energy electronics technologies (FLEET) for providing me the opportunity to participate in several valuable educational programs.

First and foremost, I offer my sincerest gratitude to my supervisors Professor Kourosch Kalantar-zadeh, Dr. Torben Daeneke, Dr. Jian Zhen Ou and Dr. Khashayar Khoshmanesh providing me with the opportunity to undertake this exciting work. Thank you for your invaluable initiatives and inputs to my work. I have been blessed to have your unconditional support and motivation to complete this thesis.

Many appreciations to the research facilities at RMIT University including the MicroNano Research Facility (MNRF), the RMIT microscopy and Microanalysis Facilities (RMMF) and RMIT chemistry laboratories. My sincere thanks to the approachable and supportive technical staff Dr. Zeyad Nasa, Dr. Chenglong Xu, Mr Yuxun Cao, Dr. Edwin Mayes, Mr Philip Francis, Mrs Nadia Zakhartchouk, Mr Frank Antolasic and Mr Paul Morrison.

I am also grateful to Dr. Joel Van Embden and Dr. Enrico Della Gaspera for offering me access to use facility and space at nanostructures laboratory at RMIT University.

I would like to thank my collaborators for their insights to my research Associate Professor Anthony O'Mullane (Queensland University of Technology), Professor Richard Kaner (University of California Los Angeles), Distinguished Professor Arnan Mitchell (RMIT University), Adrian P. Mouritz (RMIT University) and Christopher F. McConville (RMIT University).

I would like to thank several of my fellow students at centre for advance electronics and sensors (CADES) at RMIT University for their contribution to my work. You have made my PhD journey

more productive and joyful, Bao Yue Zhang, Nripen Dhar, Azmira Jannat, Farjana Haque, Hareem Khan, Md Mohiuddin, Naresh Pillai, Nitu Syed, Rebecca Orrell-Trigg, Robi Datta and Kibret Messalea.

Lastly, I thank all my friends and family for their love and encouragements. Thank you for your unconditional kindness despite having less time to spend with you during my PhD candidature.

Table of contents

Abstract of Thesis	ii
Declaration	v
Acknowledgements	vi
Table of contents	viii
List of Figures	xi
List of Tables	xx
Abbreviations	xxi
Motivations and Objectives	1
3.3.1. Motivations.....	1
1.1. Objectives	3
1.2. Organisation of thesis	4
References	5
Literature Review.....	9
2.1. Introduction	9
2.1.1. Surface of gallium based liquid metals in aqueous electrolytes	10
2.1.2. Exploring the surface composition of complex alloys of gallium.....	12
2.1.3. Surface composition of complex liquid gallium alloys in H ₂ O	15
References	17
Ionic imbalance induced self-propulsion of liquid metals	26
3.1. Introduction	26
3.2. Experimental details	27
3.2.1. Ionic Imbalance Framework.....	27
3.2.2. Voltage Characterization	27
3.2.3. Self-propelling Droplet.....	27
3.3. Results and Discussions	28
3.3.2. pH imbalance.....	28
3.3.3. Droplet dynamics under pH imbalance	30
3.3.4. Deformation of liquid metal droplets	30
3.3.5. Marangoni flow of liquid metal droplets.....	31
3.3.6. Dynamics regions	35
3.3.7. Effect of mixed salt concentration on liquid metal droplet dynamics	39
3.3.8. Voltage characterizations	41
3.3.9. Energy calculations of the surface Marangoni flow	44
3.3.10. Applications of liquid metal based on ionic imbalance self-propulsion.....	46

3.4.	Surface tension measurement between galinstan and aqueous ionic electrolytes	51
3.5.	Conclusion.....	52
	References	56
A liquid metal reaction environment for the room temperature synthesis of atomically thin metal		
	oxides	58
4.1.	Introduction	58
4.2.	Experimental details	59
4.2.1.	Eutectic gallium indium tin alloy (galinstan) preparation	59
4.2.2.	Co-alloying process	60
4.2.3.	Van der Waals exfoliation synthesis	60
4.2.4.	Gas injection synthesis	63
4.2.5.	Instrumentation and characterization.....	64
4.2.6.	Fitting of I-V data: The Schottky emission model	65
4.2.7.	Band Gap determination using electron energy loss spectroscopy (EELS)	67
4.3.	Results and Discussions	68
4.4.	Conclusion.....	78
	References	79
Green synthesis of low dimensional aluminium oxide hydroxide and oxide using liquid metal		
	reaction media: Ultra-high flux membranes	81
5.1.	Introduction	81
5.2.	Experimental details	82
5.2.1.	Alloy preparation.....	82
5.2.2.	Liquid based synthesis.....	83
5.2.3.	Vapour based synthesis	84
5.2.4.	Repetition, evidencing green synthesis	85
5.2.5.	Membrane preparation.....	86
5.2.6.	Emulsion preparation.....	86
5.2.7.	Annealing for conversion of γ -AlOOH to γ -Al ₂ O ₃	87
5.2.8.	Instrumentation and characterization.....	87
5.3.	Results and discussions	88
5.4.	Conclusions	105
	References	105
Conclusions and Future Work.....		
6.1.	Conclusions	110
6.2.	Stage 1	111
6.3.	Stage 2	111
6.4.	Stage 3	112

6.5.	Future Work.....	114
6.5.1.	Kinetics of the EDL.....	114
6.5.2.	Marangoni flow regiment applications.....	114
6.5.3.	Dynamics of liquid metal marbles electrolytes	115
6.5.4.	Synthesis of other 2D oxides using other liquid metal melts	115
6.5.5.	Functionalised membranes	116
6.5.6.	Low dimensional oxide hydroxides of other material	116
6.6.	Journal Publications.....	116
6.6.1.	First-author Publications (presented in this thesis).....	117
6.6.2.	Co-author Publications (not presented in this thesis)	117

List of Figures

- Figure 3.1.** EDL schematic and experimental framework for analysing liquid metal droplet dynamics under ionic imbalance. (a) Top view schematic of the droplet and arrangement of ions, forming the EDL. (b) Schematic of the experimental setup showing two U-shaped open-top (see inset) PMMA inlet channels which extend in parallel and join at an outlet. Two channels carry different types of electrolytes represented in distinct colours, acidic in yellow and basic in blue. Two parallel flows come in contact with the Galinstan droplet of 3 mm diameter residing in a recess. (c) Actual experimental set up. (d) Close up view of c. Scale bars are 5 mm. 29
- Figure 3.2.** Effect of the droplet size on droplet dynamics. (a and b) In three sets of experiments with varying droplet diameter, dynamics of the droplet in deformation dominant regions did not change significantly. Molarities are constant at 2.4 mol L⁻¹ acid and 0.3 mol L⁻¹ of base. Error bars indicated s.e.m. (n=6). 30
- Figure 3.3.** Reference diagram of the dynamics of the liquid-metal droplets under different HCl and NaOH concentrations. (a) Schematic of the deformation ratio measurements for D₁/D₂ assessment. ‘Black square’ indicates experiments with deformation dominating the dynamics and Marangoni flow dominant experiments are represented by ‘red circles’. (b) Demonstration of Marangoni flow and sequential snap shots shows a micro particle transferring from NaOH to HCl. The tangential skin flow displaced component, as a result of the Marangoni effect, contains a Galinstan layer near the surface of the droplet, an oxide layer and a layer of electrolyte also near the surface. A thickness of δ is used to define the effective thickness of this layer. (c) Selected enlarged images showing droplet deformation (in black arrows) towards NaOH while Marangoni flow (in red arrows) direction is towards HCl. Scale bars are 1 mm. 32
- Figure 3.4.** Reference diagram of liquid metal droplet dynamics under a pH imbalance. Each ‘black square’ or ‘red circle’ presents an experiment with measurable deformation ratio or Marangoni flow, respectively (overlapped ‘black square’ and ‘red circle’ indicates experiments with both measurable Marangoni flow and deformation ratios without a distinct dominating effect), in various ionic concentrations of HCl and NaOH between 0.3 to 3 mol/L (pH of ~0.5 to ~ -0.5 for HCl and ~13.5 to ~14.5 for NaOH

respectively). The background of the reference diagram is coloured blue, green and yellow accordingly, to represent each of the regions (deformation, deformation-Marangoni, and Marangoni regions) discussed in the text..... 33

Figure 3.5. Galinstan surface oxidation in high molarities of acid and base. (a) At high HCl and NaOH concentrations, relatively large and thick oxide flakes are formed on the surface of droplets and delaminated. These flakes move along the surface of Galinstan droplet toward the acidic side. The oxide flakes can be mechanically exfoliated simply by tweezers (inset). Scale bars are 0.5 and 0.1 mm in a and inset respectively. (b) To understand the composition and nature of the oxide flakes, the surface of the two sides of the droplet were analysed using Raman microspectroscopy. Results indicate five distinct peaks (P1-5) matching Raman spectra of α -gallium oxyhydroxide⁶. The peaks' intensities increased significantly when droplet was exposed to higher imbalanced concentrations, which indicates the formation of much thicker α -gallium oxyhydroxide flakes (at least 4-5 times thicker comparing 0.3 and 3 mol L⁻¹ concentrations if the relation is considered linear). Peak intensities are different for skins in NaOH and HCl areas due to the difference of hydration and surface charges. Due to the damping effect of liquid metal under the surface of flakes, peaks located in wavenumbers lower than 500 cm⁻¹ are weakened. (c) In higher molarities of electrolytes, thicker layers of α -gallium oxyhydroxide flakes form on the NaOH side of the droplet. These thick layers delaminate from the surface, with the help of bubbles that are produced by the chemical reactions on the surface of droplet and move toward the HCl side under the effect of surface tension difference. This causes a tangential skin flow. These flakes are eventually released into the aqueous solution as the effect of the flow in the channels..... 34

Figure 3.6. Mercury droplet dynamics under ionic imbalance. (a) At low concentrations of electrolyte, droplet deformation is observed, similar to that of Galinstan. (b) At high concentrations of electrolytes, the mercury droplet does not exhibit any tangential skin flow due to Marangoni effect, as opposed to the Galinstan liquid metal. This is evidenced as the micro particles deposited over the surface of mercury droplet remain stationary. Scale bars are 0.5 mm. 37

Figure 3.7. Changes of deformation and Marangoni flow under different conditions. (a) Graph of the experimental measurements with varying NaOH and constant HCl molarities. (b) Graph of the experimental measurements with varying

HCl and constant NaOH molarities. Black and red lines indicate droplet deformation ratio and Marangoni flow rates respectively. Background colours correspond to regions of the reference diagram in Fig. 3.4. Error bars are s.e.m. (N=6). (c-f) Graphs present the deformation ratio and Marangoni flow in varying concentrations of NaCl while concentrations of NaOH and HCl are kept constant. NaCl is mixed with NaOH in all experiments. Error bars are s.e.m. (N=6)..... 38

Figure 3.8. Effect of pH imbalance of different acid and base solutions on droplet dynamics. (a) Varying concentration of H₂SO₄ is used with constant 0.3 mol L⁻¹ of NaOH. As expected, droplet deformation was more dominant. Background is coloured in blue to indicate the droplet is operating in region 1 of the reference diagram of Fig. 3.4. (b) Region 2 and 3 are tested with varying concentration of KOH and constant concentration of 3.4 mol L⁻¹ HCl. The Marangoni dominant region is shifted to higher concentrations of KOH solution than that of NaOH. 39

Figure 3.9. Droplet dynamics under imbalanced mix ionic solution of low NaOH molarity. NaCl mixed solutions are prepared in low molarities of 0.3 mol L⁻¹ NaOH. HCl is kept constant at 0.6 mol L⁻¹. Error bars indicated s.e.m. (n=6). (a and b) Graphs present deformation ratio and Marangoni flow in varying concentrations of NaCl while concentrations of NaOH and HCl are kept constant. NaCl is mixed with NaOH in all experiments. In a Maximum deformation is seen in 0.3 mol L⁻¹ of NaCl while Marangoni flow maximum in b is located at 0.6 mol L⁻¹ of NaCl..... 40

Figure 3.10. Characterization of droplet dynamics with an external applied electrical potential. (a) Electrodes are covered with Galinstan and placed in rectangular recesses (b) Marangoni flow and deformation direction of droplet created by the electrical potential. Scale bar is 0.5 cm. (c and d) Graphs of deformation ratios and Marangoni flow velocities under the applied electrical potential. Applied potentials that are greater than presented here cause the oxidation of the liquid metal. Error bars indicate s.e. (N=6). Calculated: (e) surface tension of the Galinstan droplet using Lippmann's equation (PZC value for EGaIn has been used in the simulation as the PZC of Galinstan¹²) and (f) the kinetic energies of Marangoni flows per unit area of a surface's cross section. Insets in d and f show graphs in linear scales. 46

Figure 3.11. Liquid metal self-propulsion. (a) Droplet propels from 1.2 mol/L HCl to 0.6 mol/L NaOH reservoir. (b) The instantaneous droplet velocity profile of experiment a. Error bars indicate the s.e. (N=2). (c) Average velocity of

droplets under different acidic and basic solutions. (d and e) Droplets velocities at different NaCl concentrations. Error bars indicate the s.e. (N=3). I, II, III in d indicate constant 0.6 mol/L NaOH (pH of ~13.8) and 0.6, 1.2 and 2.4 mol/L HCl (pH of 0.2, ~ -0.1 and ~ -0.4), respectively. I, II, III in e indicate constant 1.2 mol/L NaOH (pH of ~14.1) and 0.6, 1.2 and 2.4 mol/L HCl (pH of ~0.2, ~ -0.1 and ~ -0.4), respectively. (f) Metal droplet pushes the liquid to produce a 6.5 mm difference in height. According to the ρgh (in which ρ is the density, g is the gravitation acceleration constant and h is the liquid height) this amount of liquid equates to a pressure exceeding ~1 mbar for 1/8 inch diameter tubing. By reducing the area, this headpressure can be significantly increased. (g) The concept of a switch based on the motion induced by the electrolyte difference on either side of the droplet. The pH difference across the liquid metal droplet induces a motion towards the basic liquid and opens the inlet to the liquid with DI water/yellow dye after 10 s. The liquid in the middle reservoir then mixes with the acidified liquid in the top reservoir. Snapshots taken at: 0, 10, 20, 60 and 120 s. Scale bars are 1 cm. 47

Figure 3.12. Self-propelling droplet with instantaneous velocity. Graph of three experimental velocity profiles with droplet velocities exceeding 20 mm s⁻¹..... 48

Figure 3.13. Channel Configuration to obtain high velocity profile of the self-propelling droplet. (a) Self-propelling droplet was tested in a longer serpentine channel. Configuration has total channel length of 18.3 cm and reservoir sizes of 5.5 cm. Experiment is conducted as explained in experimental methods. (b) Configuration is selected from region 2 of Fig. 3.3c to demonstrate the velocity profile in a region with measurable Marangoni flow and less deformation ratio. The droplet velocity profile shows a cyclic behaviour and descends regularly due to the mixing effect caused by the Marangoni flow. 50

Figure 3.14. Droplet contact angle. (a) Droplet contact angle on a silicon substrate after the exposure to relatively low molarity imbalance, which results in soft and deformable skin. (b) Droplet contact angle after the exposure to molarities, which produce the maximum propulsion. (c) Droplet showing asymmetric contact angles when placed in ionic imbalance condition in b. (d) Droplet contact angle after the exposure to relatively high molarity imbalance which results in contact angles for producing less wettability and deformability than that of a. d represents an example of the Marangoni region. 54

- Figure 3.15.** Surface tension measurement between Galinstan and aqueous ionic electrolytes. (a) Surface tension was measured using pendant drop method¹⁶. (b) Surface tension of Galinstan in contact with aqueous solutions of different HCl and NaOH concentrations. Error bars are s.e.m. (N=4).55
- Figure 4.1.** Fundamental principles and synthetic approach. (A) Gibbs free energy of formation for selected metal oxides (5, 6). Oxides to the right of the red dashed line are expected to dominate the interface. (B) A cross-sectional diagram of a liquid metal droplet, with possible crystal structures of thin layers of HfO₂, Al₂O₃, and Gd₂O₃ as indicated. (C) Schematic representation of the van der Waals exfoliation technique. The pristine liquid metal droplet is first exposed to an oxygen-containing environment. Touching the liquid metal with a suitable substrate allows transfer of the interfacial oxide layer. An optical image is shown at the right. (D) Schematic representation of the gas injection method (left), photographs of the bubble bursting through the liquid metal (centre), and an optical image of the resulting sheets drop-cast onto a SiO₂/Si wafer (right). 62
- Figure 4.2.** Characterization of the dispersion of co-alloyed elements in the liquid metal using EDXS. Colour maps were used to confirm the successful dispersion of the added elements within galinstan. The scale bars are 2 μm. Since all precursor metals were purchased as micron sized powders (sizes between 5 and ~500 μm, depending on the metal), successful amalgamation is observed. No micron sized inclusions of the added metal were observed throughout EDXS characterization. The EDXS data were utilised to determine the overall concentration of the added metal within the melt which was ~1% in all cases as expected. 69
- Figure 4.3.** Characterization of materials derived from the exfoliation method. Left: AFM images, with thickness profile (inset) determined at the red line as indicated. Centre: TEM characterization, with selected-area electron diffraction (SAED) (top inset) and HRTEM images (bottom inset; scale bar, 0.5 nm). Right: Elemental composition determined by XPS²²⁻²⁷. (A) Results obtained from a eutectic gallium-indium-tin alloy. (B to D) Alloys containing approximately 1% of added hafnium, aluminium, and gadolinium, respectively. See Fig. 4.2 for characterization of the alloys before use. The lattice parameters in SAED and HRTEM images were indexed using literature reports¹⁸⁻²⁰. The lack of crystallinity in the gallium oxide sample might be beam-induced. See Fig. 4.4 for XPS spectra used to determine the oxide composition. The sample derived from pure galinstan

features metallic inclusions, which are visible as dark dots and elongated nodules. The other materials feature no inclusions. The lateral dimensions of the 2D sheets are extraordinarily large and exceed the AFM field of view..... 71

- Figure 4.4.** XPS spectra of the exfoliated sheets as shown in Figure 4.3. The XPS results indicate that the oxides exfoliated from the surface of the liquid metal consist of single element oxides. Other elements that were present in the precursor alloy have no measurable signals. Peak positions and binding energy ranges were auto selected by the Avantage software. Due to the thin nature of the oxide layers, signals from the substrates may mask the sample signal. Therefore, different binding energy ranges were selected featuring high sensitivity factors and no overlap between possibly present elements. According to the Avantage database, Ga⁰ peaks are located at 18.7 eV (Ga3d), 159.5 eV (Ga3s) and 1117 eV (Ga2p) eV. In⁰ and Sn⁰ have peaks at 444 eV (In3d) and 484.8 eV (Sn3d), respectively. Hf⁰, Al⁰ and Gd⁰ have peaks at 382 eV (Hf4p), 72.9 eV (Al2p) and 1186 eV (Gd3d), respectively. The corresponding peaks of the oxides are expected to appear at slightly higher binding energies²²⁻²⁷. The absence of peaks in the regions associated with possibly present side products leads to the conclusion that the produced nanosheets are pure within the resolution of the measurement. The small peak in the Gd3d region next to the Gd₂O₃ peak is a satellite feature. The results are summarised in Figure 4.3. 73
- Figure 4.5.** XPS results for the control experiment on liquid metal alloys containing added Ag and Cu. The exfoliation synthesis was utilised in order to exfoliate the surface oxide onto SiO₂ substrate. The XPS results confirm the absence of Cu (A) and Ag (B) oxides. 74
- Figure 4.6.** Characterization of materials derived from the gas injection method. Left: AFM images, with thickness profile (inset) determined at the red line as indicated. Centre: TEM characterization, with SAED (top inset) and HRTEM images (bottom inset; scale bar, 0.5 nm). Right: Raman spectra of the resulting oxides. (A) Results obtained from a eutectic gallium-indium-tin alloy. (B) Alloy containing approximately 1% of added hafnium. The Raman spectra match well with literature reports for Ga₂O₃ (A) and HfO₂ (B)¹⁸. 75
- Figure 4.7.** Gas injection synthesis of Ga₂O₃ results in metal inclusions. The inclusions are well separated and spread throughout the nanosheets. (A) and (B) show AFM and TEM images of these inclusions. The AFM height profile in (A) reveals that the height of these nano-sized inclusions is ~10-15 nm once the

	thickness of the oxide sheet is considered. TEM imaging (B) confirms that the width of these inclusions is roughly 16 nm.....	76
Figure 4.8.	Characterization of HfO ₂ as a dielectric. (A) Schematic of the peak force tunnelling AFM (PF-TUNA) setup. (B) AFM height (top) and current (bottom) maps for the edge region of an HfO ₂ sample directly deposited onto a Pt-coated wafer by the exfoliation method. Both maps are 300 nm wide. The profiles at the right correspond to the regions indicated by the red lines. The HfO ₂ and Pt sides are labelled. (C) Current-voltage curve measured through the HfO ₂ layer. Inset: Fit to the Schottky emission model and the determined dielectric constant (see section 4.2.6). (D) Plot of the low-loss EELS spectrum, which provides an estimate of the band gap. Inset: Analysis of the nature of the band gap, indicating a direct gap ((see section 4.2.7).....	77
Figure 4.9.	I-V curve using the PF-TUNA experimental set up shown in Fig 4.8A, measuring the I-V curve of the conductive tip when in direct contact with the platinum substrate.	78
Figure 5.1.	(a) DI water is added to a drop of a liquid metal alloy of galinstan-Al. After 30 min of exposure to water a hydrogel is formed. The proposed growth mechanism of the product shows that the skin is delaminated by hydrogen bubbles in the form of sheets into the DI water. The photo shows the final product from adding 2 ml DI water to 0.5 g of a 3.3 wt% galinstan-Al alloy. (b) Vapour is fed into the glass vial containing 0.5 g of 3.3 wt% galinstan-Al. After 30 min an aerogel has grown from the liquid metal. The growth mechanism shows the emergence of fibrous structures from the vapour nucleation sites. The photo shows the aerogel that has grown from the surface of the liquid metal. (c) The reaction stops after the consumption of all the aluminium but the galinstan remains unchanged after producing the aluminium hydroxides. Therefore, a green process is adopted to reuse the galinstan for the next synthesis cycle.....	84
Figure 5.2.	SEM image of the perpendicular growth of the fibres from the surface of the liquid metal in vapour based synthesis.	90
Figure 5.3.	Characterization (a-f) of 2D and (g-l) 1D γ -AlOOH. (a-c) TEM, SEM, and AFM images of 2D sheets that are as-obtained products of water-based synthesis dried at 170 °C. (d-f) HRTEM with SAED (inset), XRD and Raman spectroscopy, respectively, show that the dried 2D sheets are γ -AlOOH. ⁸ (h-i) TEM, SEM, and AFM images of the obtained products from vapor-based synthesis that include 1D fibers. (j-l) HRTEM with SAED	

	(inset), XRD and Raman spectroscopy, respectively, clearly show that the 1D fibres are poorly crystalline γ -AlOOH.....	92
Figure 5.4.	Raman spectrum of bayerite α -Al(OH) ₃ ⁸ which is produced during water based synthesis.....	93
Figure 5.5.	Characterization of annealed γ -Al ₂ O ₃ . Left and right columns present 2D and 1D γ -Al ₂ O ₃ respectively. (a and d) low resolution TEM images and (b and e) high resolution TEM images of a selected crystalline section. (c and f) show the associated XRD patterns.....	94
Figure 5.6.	(a and b) Peak force quantitative nanomechanical mapping (PF-QNM) AFM characterization of 2D γ -AlOOH and 2D γ -Al ₂ O ₃ flakes, respectively. Corresponding DMT modulus maps are shown above the histogram. (c) Optimisation of the BET of surface area of the 2D γ -AlOOH by changing the aluminium concentration. (d) Green synthesis shown in Fig. 5.1c with three repetitions showing an increase in surface area after two repetitions. (e) EDXS elemental composition results for the low centrifuged products demonstrate no metal inclusions and (f) no aluminium is found on the surface of the liquid metal after completion of three synthesis cycles.	97
Figure 5.7.	Photos of the obtained hydrogels from water based synthesis when the concentration of aluminium in the galinstan liquid metal is changed. Weight percentages of aluminium in galinstan are shown above each photo. Each photo was taken after 30 min from the start of the reaction with DI water. Products from these photos were used for BET analysis and the optimisation of surface area in Fig. 5.6.	98
Figure 5.8.	TEM image (left) and two high resolutions SEM images (right). Products from higher concentrations of aluminium (≥ 5 wt%). The structures include cone shaped bayerite somatoids ¹⁰ in addition to the two-dimensional (2D) sheets.....	98
Figure 5.9.	(a and b) BJH adsorption, desorption and isotherm plot of the liquid water grown boehmite shown in Fig. 5.6d (second cycle of the synthesis). (c and d) BJH adsorption, desorption and isotherm plot of the vapour grown boehmite. The surface area measurement is shown as a hollow circle in Fig. 5.6c.....	99
Figure 5.10.	Energy-dispersive X-ray spectroscopy (EDXS) of boehmite after centrifuge (Figure 5.6e). Metal inclusions in the product such as liquid metal droplets can be removed by a slow centrifuge at 50 RCF for 15 min. EDXS results show no liquid metal inclusion in supernatant after this protocol. This sample is associated with the Raman analysis in Figure 5.3f. Substrate is Au	

coated Si substrate with an adhesion layer of Cr which appears in the EDXS spectrum.....	100
Figure 5.11. EDXS analysis of the galinstan droplet after 3 repetitions in Figure 5.6f shows no detectable aluminium on the surface of the liquid metal.	101
Figure 5.12. (a) Vapour grown and (b) water grown γ -AlOOH self-assembled structures, respectively. As shown in a , self-assembled structures grown on a galinstan droplet form 1D fibres of γ -AlOOH which result in a translucent material. The photo on the bottom of a demonstrates the transparency of the material on graph paper with 5×5 mm grid sizes. b shows the grown and delaminated layers of self-assembled 2D structures of γ -AlOOH. Synthesis process is detailed in section 5.2.5. (c) Schematic of the membrane adsorption of lead ions during filtration and a photo of the experiment and fabricated membrane (top). (d) Schematic of oil-in-water emulsion separation in which water permeates through the membrane however, oil is retained. The photo shows the experimental setup in which the arrows indicate the direction of the flow to/from a multi-channel peristaltic pump. (e) TGA analysis of the oil-in-water emulsion separation performance of the membrane is shown in d	103

List of Tables

Table 2.1.	Tabulated thermodynamic properties of single element oxides ⁵⁸⁻⁵⁹	13
Table 3.1.	Ionic coefficients: List of experimental measurements of the Marangoni flow coefficient α , threshold potential φ_{Th} and potential of zero charge φ_0 . R^2 is the coefficient of determination of the linear regression trend line gradient of the Marangoni flow velocity against potential.	43
Table 3.2.	Values of A and B_i for pendant drop shape analysis.....	52

Abbreviations

1D	One-dimensional
2D	Two-dimensional
3D	Three-dimensional
AFM	Atomic force microscopy
BET	Brunauer Emmett Teller
CVD	Chemical vapour deposition
DI	Distilled water
DMT	Derjaguin Mueller Toporov
EDL	Electrical double layer
EDSX	Energy dispersive X-ray spectroscopy
EELS	Electron energy loss spectroscopy
ESEM	Environmental scanning electron microscope
FIB	Focused ion beam
HRTEM	High resolution transmission electron microscopy
ICP-MS	Inductively coupled plasma mass spectrometer
ITO	Indium tin oxide
I-V	Current-voltage
LDH	Layered double hydroxides
PFA	Perfluoroalkoxy
PF-QNM	Peak force quantitative nanomechanical mapping
PF-TUNA	Peak force tunnelling atomic force microscopy
PMMA	Polymethyl methacrylate
PZC	Potential of zero charge
SAED	Selected area electron diffraction
SEM	Scanning electron microscopy
TEM	Transmission electron microscopy
TGA	Thermal gravimetric analysis
XPS	X-ray photoelectron spectroscopy
XRD	X-ray diffraction

Chapter 1

Motivations and Objectives

3.3.1. Motivations

Recently, gallium based liquid metals have attracted considerable attention in research and industry. With the emergence of gallium as a non-hazardous option comparing to mercury, the possibility of utilising gallium based liquid metals in practical applications has become more attractive¹⁻². Gallium and its liquid metal alloys feature diverse and remarkable properties for emerging applications in microfluidics, 3D printing, flexible and stretchable electronics and reconfigurable devices, optics and reversible electrochemical systems³⁻¹⁴. Liquid metals interact with the environment through their surfaces. Therefore, the investigation of liquid metal's surface chemical and physical properties is of utmost importance for understanding and determination of characteristics such as wettability, electrical double layer formation, droplet actuation mechanisms, deformability, surface composition and corrosion behaviour.

For specific applications, liquid metals can be immersed in aqueous electrolyte environments^{7, 15-23}. When liquid metals are submerged into such aqueous electrolytes an electrical double layer (EDL) forms on their interfaces with the environments²⁴. The EDL gives rise to the surface capacitive

properties by accumulating charges²⁴. The energy stored within the EDL can be converted into mechanical motions²⁵⁻²⁶. The EDL formation and surface capacitive properties are strong functions of electrolyte types and concentrations. However, these surface effects have not been fully investigated in literature. These investigations are used for discovering the answers to the fundamental research questions including: What is the effect of aqueous electrolyte solutions on dynamics of the liquid metal droplets based on the surface formed EDL? and how to manipulate this EDL for inducing surface Marangoni flow and deformation? If surface manipulations are found to induce substantial effects on droplet dynamics, it can lead to significant applications in microfluidics.

Both in the air and aqueous solutions, atomically thin layers of gallium oxide and hydroxide are formed on the surface of gallium liquid metal at its interface with oxygen containing environments and water molecules, respectively²⁷⁻²⁸. These formed thin layers are naturally of two-dimensional (2D) nature and are shown to be useful for the applications in electronics, optics and catalysis²⁷⁻²⁸. However, there is no study that explores these liquid metal surface oxides to obtain desired layered compounds other than gallium. Fundamental understanding of methods for the modifications and isolation of these surface oxides will present substantial technological potentials. These explorations will help to answer research questions such as: Can the surface oxide layers on liquid gallium alloys be isolated as 2D layers and can a liquid gallium reactor be devised for their production? How does the composition of the surface oxide depend on the alloys composition and can co-alloying of metals with different energy of oxide formations? These questions can be expanded to metal hydroxides growth at interfaces with water molecules. Discovering the answers can potentially lead to new methods for synthesising 2D materials by using liquid metals as reaction solvents, thereby giving access to a variety of metal oxide compounds that have not been accessible before. This new method for synthesising 2D materials can overcome challenges that exist for the current methods such as process costs, complexity, scalability and performance²⁹⁻³¹.

1.1. Objectives

Author's developed scope of work focuses on the exploration of hypotheses that can address the research gaps and questions identified and presented in the previous section. Accordingly, objectives of this research are targeted towards investigation of the followings:

1. Based on the Lippmann's equation change in the potential of zero charge (PZC) on each side of a liquid metal droplet will induce a surface tension gradient across the droplet³². The PZC on surfaces can be modulated by modification of pH of electrolytes³³. Author hypothesises that when two opposite sides of a droplet are exposed to different pH values, the difference in the PZC should induce a surface tension gradient. The surface tension gradient therefore can be observable by deformation and surface Marangoni flows. Author further hypothesises that adding natural salts to one side of droplet should also change the chemical potentials. According to the Lippmann's equation potential gradient will induce surface tension gradient and as a result will alter droplet dynamics.

2. In ambient conditions, surface composition of gallium based liquid metal alloys, such as gallium-indium-tin and gallium-indium, found to be only made of gallium oxides³⁴⁻³⁵. This is despite the presence of indium and tin within both alloys³⁴⁻³⁵. This observation leads to the hypothesis that the composition of the surface oxides includes the metal oxides of favourable (more negative) Gibbs energy for oxidation reactions. To investigate this hypothesis, metals with more negative Gibbs free energy for the formation of metal oxides with reference to gallium oxide, such as hafnium, aluminium and gadolinium oxides, are selected. These metals are individually mixed with the gallium liquid metal using a grinding process. For control experiments, metals with less negative Gibbs free energy for the formation of metal oxides, such as silver and copper oxides, than that of gallium oxide are selected. The surface oxides need to be isolated from the liquid metal for analysis and incorporating in practical applications. It is assumed that the isolation of the surface oxide from liquid metal is possible due to weak attractive forces between the oxides and the parent liquid metal. Two methods are proposed for the surface oxide isolation. In the first proposed process, the surface of liquid metal is touched with a substrate. Direct transfer of oxide onto a substrate surface is believed to be possible *via* van der Waals attraction forces. Second process is proposed to increase yield of production. In this

method, compressed air is injected into the liquid metal alloy. During this process, a layer of oxide should form at the interface of the air bubble and the liquid metal alloy. The bubble should then rise to the surface and burst into a solvent which is placed above the liquid metal alloy. When bubble is burst, it is believed the surface oxides should disperse into the solvent.

3. In the third stage of this PhD research, hypothesis in the previous step is expanded to the interface of gallium liquid metal alloys with water molecules. Aluminium is an abundant element in nature and easy to mix with gallium liquid metals in high quantities. Aluminium compounds are selected as target materials due to their high industrial significance. The Gibbs free energy of reaction for producing aluminium hydroxides is more favourable with reference to gallium hydroxides. It is hypothesised that aluminium hydroxides should form at the interface of the liquid metal alloy with water molecules. Additionally, it is theorised that different morphological growth of the hydroxides can be accessible through either covering the entire surface of galinstan with water or exposing the surface to water vapour. Where former is assumed to produce 2D morphological structures and latter to form 1D fibrous morphologies growing from the water vapour nucleation sites.

1.2. Organisation of thesis

The aim of this research is to gain fundamental, theoretical and applied research analysis of the surface properties of liquid metal alloys of gallium.

Chapter 2 presents the literature review of this thesis. In the research work presented in this PhD thesis the surface of gallium based liquid metals are explored when interfaced with aqueous electrolytes, oxygen containing environment and water molecules. Current methods of liquid metal actuations and their limitations are assessed. Then the available knowledge in surface compositions of gallium based liquid metal alloys, when exposed to ambient air and water, are discussed.

In chapter 3 the effect of pH gradient on the deformation and induced surface Marangoni flow of gallium based liquid metal droplets is analysed. To discover fundamental mechanism of droplet dynamics and enable accurate modelling of the system, several different concentrations and types of

electrolytes and salts are investigated. The droplet deformation is mathematically modelled and an equation to describe surface Marangoni flow is derived. Several applications of such systems that operate only by changing electrolytes surrounding a droplet are demonstrated.

Chapter 4 demonstrates the fundamental method to modify the surface oxide compositions of gallium based liquid metal alloys when co-alloyed with many other metals. Two methods for the isolation of the surface oxides are demonstrated. Atomic force microscopy demonstrate metal oxides that are produced from both methods feature ultra-thin with large lateral dimensions. An electronics insulator is made from the 2D hafnium oxides and its dielectric constant is measured with peak force tunnelling current atomic force microscope which are all presented in this chapter.

In chapter 5, the synthesis and growth of low dimensional hydroxides and oxide hydroxides from the surface of the gallium-aluminium liquid metal alloys at interface with water molecules are explored. It is shown that 2D aluminium hydroxide sheets grow on the surface of the alloy when interfaced with liquid phase water. In contrary, 1D fibrous morphologies of aluminium oxide hydroxide grow at the interface of the alloy with water vapour. These low dimensional structures are fully characterised and annealed to be converted to aluminium oxides. Free standing membranes are made from the 2D morphologies of the aluminium oxide hydroxides, which demonstrated to be suitable materials for separating oil from water and adsorption of lead contaminated water. A full description of the green synthesis adopted to reuse gallium liquid metals after each synthesis cycle is shown in this chapter.

Chapter 6 of this thesis contains overall conclusion for chapters 3, 4 and 5. The potential for future work is discussed based on the research outcomes presented in this thesis.

References

1. Dickey, M. D., Emerging applications of liquid metals featuring surface oxides. *ACS Appl. Mater. Interfaces* **2014**, *6* (21), 18369-18379.
2. Tingyi, L.; Sen, P.; Kim, C. J., Characterization of nontoxic liquid-metal alloy galinstan for applications in microdevices. *J. Microelectromech. Syst.* **2012**, *21* (2), 443-450.

3. Koo, H.-J.; So, J.-H.; Dickey, M. D.; Velev, O. D., Towards all-soft matter circuits: prototypes of quasi-liquid devices with memristor characteristics. *Adv. Mater.* **2011**, *23* (31), 3559-3564.
4. Cheng, S.; Wu, Z., A microfluidic, reversibly stretchable, large-area wireless strain sensor. *Adv. Funct. Mater.* **2011**, *21* (12), 2282-2290.
5. Jeong, S. H.; Hagman, A.; Hjort, K.; Jobs, M.; Sundqvist, J.; Wu, Z., Liquid alloy printing of microfluidic stretchable electronics. *Lab Chip* **2012**, *12* (22), 4657-4664.
6. Zhang, W.; Ou, J. Z.; Tang, S. Y.; Sivan, V.; Yao, D. D.; Latham, K.; Khoshmanesh, K.; Mitchell, A.; O'Mullane, A. P.; Kalantar-Zadeh, K., Liquid metal/metal oxide frameworks. *Adv. Funct. Mater.* **2014**, *24* (24), 3799-3807.
7. Tang, S. Y.; Sivan, V.; Khoshmanesh, K.; O'Mullane, A. P.; Tang, X.; Gol, B.; Eshtiaghi, N.; Lieder, F.; Petersen, P.; Mitchell, A.; Kalantar-zadeh, K., Electrochemically induced actuation of liquid metal marbles. *Nanoscale* **2013**, *5* (13), 5949-5957.
8. Majidi, C.; Kramer, R.; Wood, R. J., A non-differential elastomer curvature sensor for softer-than-skin electronics. *Smart Mater. Struct.* **2011**, *20* (10), 105017.
9. Ota, H.; Chen, K.; Lin, Y.; Kiriya, D.; Shiraki, H.; Yu, Z.; Ha, T.-J.; Javey, A., Highly deformable liquid-state heterojunction sensors. *Nat. Commun.* **2014**, *5*, 5032.
10. Ladd, C.; So, J.-H.; Muth, J.; Dickey, M. D., 3D printing of free standing liquid metal microstructures. *Adv. Mater.* **2013**, *25* (36), 5081-5085.
11. Zheng, Y.; He, Z.; Gao, Y.; Liu, J., Direct desktop printed-circuits-on-paper flexible electronics. *Sci. Rep.* **2013**, *3*, 1786.
12. Hammock, M. L.; Chortos, A.; Tee, B. C. K.; Tok, J. B. H.; Bao, Z., 25th anniversary article: the evolution of electronic skin (E-Skin): a brief history, design considerations, and recent progress. *Adv. Mater.* **2013**, *25* (42), 5997-6037.
13. Palleau, E.; Reece, S.; Desai, S. C.; Smith, M. E.; Dickey, M. D., Self-healing stretchable wires for reconfigurable circuit wiring and 3D microfluidics. *Adv. Mater.* **2013**, *25* (11), 1589-1592.
14. Chrimes, A. F.; Berean, K. J.; Mitchell, A.; Rosengarten, G.; Kalantar-zadeh, K., Controlled electrochemical deformation of liquid-phase gallium. *ACS Appl. Mater. Interfaces* **2016**, *8* (6), 3833-3839.
15. Sen, P.; Kim, C. J., A fast liquid-metal droplet microswitch using EWOD-driven contact-line sliding. *J. Microelectromech. Syst.* **2009**, *18* (1), 174-185.
16. Khan, M. R.; Eaker, C. B.; Bowden, E. F.; Dickey, M. D., Giant and switchable surface activity of liquid metal via surface oxidation. *Proc. Natl. Acad. Sci. USA* **2014**, *111* (39), 14047-14051.
17. Zhang, J.; Sheng, L.; Liu, J., Synthetically chemical-electrical mechanism for controlling large scale reversible deformation of liquid metal objects. *Sci. Rep.* **2014**, *4*, 8.
18. Beni, G.; Hackwood, S., Electro-wetting displays. *Appl. Phys. Lett.* **1981**, *38* (4), 207-209.

19. Sheng, L.; Zhang, J.; Liu, J., Diverse transformations of liquid metals between different morphologies. *Adv. Mater.* **2014**, *26* (34), 6036-6042.
20. Nelson, W. C.; Kim, C. J., Droplet actuation by electrowetting-on-dielectric (EWOD): A review. *J. Adhes. Sci. Technol.* **2012**, *26* (12-17), 1747-1771.
21. Junghoon, L.; Kim, C. J., Surface-tension-driven microactuation based on continuous electrowetting. *J. Microelectromech. Syst.* **2000**, *9* (2), 171-180.
22. Latorre, L.; Kim, J.; Lee, J.; De Guzman, P. P.; Lee, H. J.; Nouet, P.; Kim, C. J., Electrostatic actuation of microscale liquid-metal droplets. *J. Microelectromech. Syst.* **2002**, *11* (4), 302-308.
23. Tang, X.; Tang, S. Y.; Sivan, V.; Zhang, W.; Mitchell, A.; Kalantar-Zadeh, K.; Khoshmanesh, K., Photochemically induced motion of liquid metal marbles. *Appl. Phys. Lett.* **2013**, *103* (17).
24. Gough, R. C.; Morishita, A. M.; Dang, J. H.; Moorefield, M. R.; Shiroma, W. A.; Ohta, A. T., Rapid electrocapillary deformation of liquid metal with reversible shape retention. *Micro Nano Syst. Lett.* **2015**, *3* (1), 1-9.
25. Tang, S.-Y.; Khoshmanesh, K.; Sivan, V.; Petersen, P.; O'Mullane, A. P.; Abbott, D.; Mitchell, A.; Kalantar-zadeh, K., Liquid metal enabled pump. *Proc. Natl. Acad. Sci. USA* **2014**, *111* (9), 3304-3309.
26. Bo, G.; Ren, L.; Xu, X.; Du, Y.; Dou, S., Recent progress on liquid metals and their applications. *Adv. Phys: X* **2018**, *3* (1), 1446359.
27. Carey, B. J.; Ou, J. Z.; Clark, R. M.; Berean, K. J.; Zavabeti, A.; Chesman, A. S. R.; Russo, S. P.; Lau, D. W. M.; Xu, Z.-Q.; Bao, Q.; Kevehei, O.; Gibson, B. C.; Dickey, M. D.; Kaner, R. B.; Daeneke, T.; Kalantar-Zadeh, K., Wafer-scale two-dimensional semiconductors from printed oxide skin of liquid metals. *Nat. Commun.* **2017**, *8*.
28. Nitu, S.; Ali, Z.; Md, M.; Baoyue, Z.; Yichao, W.; S., D. R.; Paul, A.; J., C. B.; Cheng, T.; Joel, v. E.; R., C. A. S.; Zhen, O. J.; Torben, D.; Kouros, K. z., Sonication-Assisted Synthesis of Gallium Oxide Suspensions Featuring Trap State Absorption: Test of Photochemistry. *Adv. Funct. Mater.* **2017**, *27* (43), 1702295.
29. Kim, D.; Cho, S.; Butch, N. P.; Syers, P.; Kirshenbaum, K.; Adam, S.; Paglione, J.; Fuhrer, M. S., Surface conduction of topological Dirac electrons in bulk insulating Bi_2Se_3 . *Nat. Phys.* **2012**, *8*, 459-463.
30. Tiwari, A.; Syväjärvi, M., *Advanced 2D Materials*. Wiley: 2016.
31. Zeng, M.; Xiao, Y.; Liu, J.; Yang, K.; Fu, L., Exploring Two-Dimensional Materials toward the Next-Generation Circuits: From Monomer Design to Assembly Control. *Chem. Rev.* **2018**, *118* (13), 6236-6296.
32. Darhuber, A. A.; Troian, S. M., Principles of microfluidic actuation by modulation of surface stresses. *Annu. Rev. Fluid Mech.* **2005**, *37*, 425-455.

33. Kosmulski, M., pH-dependent surface charging and points of zero charge. IV. Update and new approach. *J. Colloid Interface Sci.* **2009**, 337 (2), 439-448.
34. Dickey, M. D.; Chiechi, R. C.; Larsen, R. J.; Weiss, E. A.; Weitz, D. A.; Whitesides, G. M., Eutectic gallium-indium (EGaIn): A liquid metal alloy for the formation of stable structures in microchannels at room temperature. *Advanced Functional Materials* **2008**, 18 (7), 1097-1104.
35. Kim, D.; Thissen, P.; Viner, G.; Lee, D.-W.; Choi, W.; Chabal, Y. J.; Lee, J.-B., Recovery of Nonwetting Characteristics by Surface Modification of Gallium-Based Liquid Metal Droplets Using Hydrochloric Acid Vapor. *ACS Appl. Mater. Interfaces* **2013**, 5 (1), 179-185.

Chapter 2

Literature Review

2.1. Introduction

In this thesis the focus is on surface properties of gallium based liquid metal alloys at interfaces with aqueous electrolytes (section 2.2.1), oxygen containing environments (section 2.2.2) and water molecules (section 2.2.3). Surface of liquid metals at interface to each of these environments offer unique features that are discussed in this chapter.

When the liquid metal is submerged in aqueous electrolytes an electrical double layer (EDL) is formed on its surface¹. Manipulation of the surface EDL leads to inducing surface Marangoni flow and deformation of liquid metal droplets which enable news observations and also the development of novel fluidic devices²⁻³. The electrolytes used can be natural, basic or acidic in nature, while basic and acidic electrolytes can facilitate the delamination or dissolution of surface oxides⁴. These surface oxides can be isolated to fabricate high performing semiconductors for applications in electronics⁵⁻⁶. When acidic or basic electrolytes are not used other phenomena may be observed. For instance, the system can be designed in a way that low dimensional oxides or oxide hydroxides can grow on the surface of the liquid metal at the interface⁷⁻⁸. However, these surface oxide and oxide hydroxides hinder the performance of the liquid metals in microfluidic channels^{7,9}.

In this chapter, an overview background on the interfacial properties of liquid metals will be discussed with the focus of the work which will be presented in this thesis.

2.1.1. Surface of gallium based liquid metals in aqueous electrolytes

Soft components based on microfluidic and elastomer technologies present an increasing promise for industrial uptake¹⁰⁻²¹ and relatively non-hazardous liquid metal alloys of gallium are set to play considerable role in this process⁷. Room temperature liquid metals have shown to be remarkable platforms for makeshift mechanical components²²⁻²⁴, reversible electrochemical systems²⁵⁻²⁶, soft sensors^{16, 25-27}, electrical components in microfluidic channels², 3D printing²⁸⁻²⁹ and stretchable and reconfigurable electronics³⁰⁻³². Controlling the motion and deformation of liquid metals is the key to the successful realization of these applications. To date, motions and deformations of liquid droplets have been demonstrated using methods such as surface oxidation modifications³³⁻³⁴, surfaces that are selective to vapours³⁵, hydrodynamic modifications³⁶, topologically modified structures³⁷⁻³⁸, fuel consumption³⁹⁻⁴⁰, the provision of energy through light sources⁴¹, electrical energy sources^{26, 33, 42-48}, and magnetic fields⁴⁹. These methods of deformation and motion induction of gallium based liquid metals can be enhanced via the formation or dissolution of surface oxides. Therefore, it has been mostly preferred to use aqueous electrolytes that are either acidic or basic surface are used⁴.

In principle, the applied driving force should break the charge symmetry that exists on the surface of a liquid metal to generate a differential pressure that either changes the configuration of the liquid and/or induces a displacement. However, there are no studies that show that this symmetry can be broken solely to differences in the environment surrounding a liquid metal. Specifically, studies to date, have not focused on the significance of the ionic composition near the surface of the metal, where an EDL forms on the droplet surface giving rise to surface capacitive properties⁵⁰, which can be used for modifying its behaviour.

The ionic imbalance at the interface between the liquid metal and the solution approaches equilibrium through the formation of an EDL as shown in Fig. 3.1a⁵¹. For a liquid metal immersed in an ionic

solution, the EDL can be modelled as a parallel-plate capacitor²⁶. Based on the integrated Lippmann's equation, the surface tension of the liquid metal droplet γ changes with the square of the potential as⁵²:

$$\gamma = -\frac{C}{2} (\varphi - \varphi_0)^2 + \gamma_0 \quad (2.1)$$

in which C is the EDL capacitance per unit area, φ is the electrode potential, φ_0 is the potential of zero charge (PZC), γ_0 is the maximum surface tension at PZC. Knowing γ , the Young–Laplace equation can be used for defining the pressure difference (ΔP) across a liquid metal hemisphere as⁵⁰:

$$\Delta P = \gamma \left(\frac{1}{R_1} + \frac{1}{R_2} \right) \quad (2.2)$$

where R_1 and R_2 are the principal radii of curvature at the interface, respectively. Equations (2.1) and (2.2) describe the change that the surface tension provides as a means to alter the pressure difference that in turn can produce a displacement and/or cause deformation of the soft liquid metal.

Changes in surface tension may be induced by directly adjusting the EDL via modifying the electrolyte surrounding the droplet that generates a surface tension difference. One possible change to the electrolyte that would affect the EDL is adjusting the ionic content by altering the pH of the solution. Another possibility is to change the composition of the electrolyte itself. A change of electrolyte has been previously shown to affect the surface tension for mercury⁵³ and liquid gallium⁵⁴. It was demonstrated that the PZC, which corresponds to the maximum on the surface tension curve, is a strong function of electrolyte type. The primary reasons for this electrolyte dependency include the variation in the electronegativity of the ions, their mobility and their intrinsic charge. Additionally, this dependence of the surface tension on the electrolyte composition is augmented, reaching a maximum value, if a positive voltage is applied to the liquid metal against a reference electrode⁵³.

In chapter 3 of this thesis, the effect of the liquid metal surface manipulation on droplet dynamics by modifying electrolytes surrounding the droplet is demonstrated. The author of this thesis will explore the effect of different acidic and basic electrolyte types and concentrations which are focused on defining the regimes in which Marangoni flow or deformation effect govern the liquid metal. The concept will be fully investigated to reveal the theories behind the phenomenon. Additionally, a few microfluidic based systems will be developed that can autonomously move droplets between acidic and basic reservoirs and pumps and switches that can operate based on environmental ionic stimuli.

2.1.2. Exploring the surface composition of complex alloys of gallium

As explained in section 2.1.1, surface of liquid metals can be manipulated by using different electrolytes to induce motion and deformation. However, in the absence of these electrolytes when exposed to air, liquid metal components react with oxygen in the surrounding environment to form a self-limiting oxide on the surface of the alloy of gallium. This self-limiting oxide constitute interesting properties that depends on the alloyed element and can vary significantly from one alloy to another depending on the incorporated elements. The focus of this section of the thesis is regarding the investigations that provide the fundamental understating of the surface oxide compositions and properties.

Most metals, including gallium-based alloys⁵⁵⁻⁵⁶, feature a self-limiting thin oxide layer under ambient conditions at the metal-air interface⁵⁷. This atomically thin interfacial oxide is considered a naturally occurring two-dimensional (2D) material. The concept of using a liquid metal as a reaction environment is based on the observation that the self-limiting oxide layers of gallium alloys, such as EGaIn and galinstan, are exclusively composed of gallium oxide, despite indium content of 22 to 25 weight percent (wt%) and tin content of as much as 10 wt % in these alloys⁵⁵⁻⁵⁶. Co-alloying suitable reactive metals allows formation of the co-alloyed metal oxides at the metal-air interface. The author of the thesis identified suitable co-alloyed metals on the basis of thermodynamic considerations,

which require that the composition of the surface oxide is determined by the reactivity of the individual metals within the melt. Thus, the oxide resulting in the greatest reduction of Gibbs free energy (ΔG_f) will dominate the surface (Fig. 4.2A). If room-temperature liquid gallium alloys are the solvent, all lanthanide oxides and a sizable portion of the transition metal and post-transition metal oxides should be accessible as 2D nanostructures (Table 2.1)⁵⁸⁻⁵⁹. In chapter 4 of this thesis, the author used eutectic gallium melts as a reaction environment to create a variety of two-dimensional metal oxides.

In chapter 4, the author of the thesis will explore the effect on composition of the surface oxides when liquid metal is co-alloyed with transition metals, post transition metals and lanthanides. This initiative is fully investigated to reveal fundamental understanding of surface oxide compositions in complex alloys of gallium. The results confirm hypothesis that the oxide composition resulting in the greatest ΔG_f , will dominate the surface of liquid metal. Then the surface oxides are isolated by two novel approaches. Firstly, surface oxides are transferred to a substrate by direct printing through van der Waals (vdW) exfoliation. In the second approach, 2D oxides are produced in a liquid suspension through gas injection synthesis. The resultant 2D oxides feature large and defect free morphologies which are demonstrated to be suitable for producing 2D insulating metal oxides.

Table 2.1. Tabulated thermodynamic properties of single element oxides⁵⁸⁻⁵⁹.

Formula	Compound name	Enthalpy ΔH kJ mol ⁻¹	Gibbs free energy ΔG_f kJ mol ⁻¹	Entropy S J mol ⁻¹ K ⁻¹
Eu₃O₄	Europium(II-III) oxide	-2272	-2142	205
Ta₂O₅	Tantalum(V) oxide	-2046	-1911.2	143.1
Sc₂O₃	Scandium oxide	-1908.8	-1819.4	77
Y₂O₃	Yttrium oxide	-1905.3	-1816.6	99.1
Er₂O₃	Erbium oxide	-1897.9	-1808.7	155.6
V₃O₅	Vanadium(III-IV) oxide	-1933	-1803	163
Tm₂O₃	Thulium oxide	-1888.7	-1794.5	139.7
Ho₂O₃	Holmium oxide	-1880.7	-1791.1	158.2
Lu₂O₃	Lutetium oxide	-1878.2	-1789	110
Tb₂O₃	Terbium oxide	-1865.2	-1776.5*	156.9*
Dy₂O₃	Dysprosium(III) oxide	-1863.1	-1771.5	149.8
Nb₂O₅	Niobium(V) oxide	-1899.5	-1766	137.2
Sm₂O₃	Samarium(III) oxide	-1823	-1734.6	151

Gd₂O₃	Gadolinium(III) oxide	-1819.6	-1732.3*	151.9*
Yp₂O₃	Ytterbium(III) oxide	-1814.6	-1726.7	133.1
Pr₂O₃	Praseodymium oxide	-1809.6	-1721.0*	158.6*
Nd₂O₃	Neodymium oxide	-1807.9	-1720.8	158.6
Ce₂O₃	Cerium(III) oxide	-1796.2	-1706.2	150.6
La₂O₃	Lanthanum oxide	-1793.7	-1705.8	127.3
Al₂O₃	Aluminium oxide	-1675.7	-1582.3	50.9
Eu₂O₃	Europium(III) oxide	-1651.4	-1556.8	146
Ti₂O₃	Titanium(III) oxide	-1520.9	-1434.2	78.8
V₂O₅	Vanadium(V) oxide	-1550.6	-1419.5	131
Mn₃O₄	Manganese(II-III)oxide	-1387.8	-1283.2	155.6
B₂O₃	Boron oxide	-1273.5	-1194.3	54
ThO₂	Thorium(IV) oxide	-1226.4	-1169.2	65.2
UO₃	Uranium(VI) oxide	-1223.8	-1145.7	96.1
V₂O₃	Vanadium(III) oxide	-1218.8	-1139.3	98.3
HfO₂	Hafnium oxide	-1144.7	-1088.2	59.3
Re₂O₇	Rhenium(VII) oxide	-1240.1	-1066	207.1
Cr₂O₃	Chromium(III) oxide	-1139.7	-1058.1	81.2
ZrO₂	Zirconium(IV) oxide	-1100.6	-1042.8	50.4
UO₂	Uranium(IV) oxide	-1085	-1031.8	77
CeO₂	Cerium(IV) oxide	-1088.7	-1024.6	62.3
Fe₃O₄	Iron(II-III)oxide oxide	-1118.4	-1015.4	146.4
Ga₂O₃	Gallium(III) oxide	-1089.1	-998.3	85
TiO₂	Titanium(IV) oxide	-944	-888.8	50.6
Mn₂O₃	Manganese(III) oxide	-959	-881.1	110.5
SiO₂	Silicon oxide	-910.7	-856.3	41.5
In₂O₃	Indium(III) oxide	-925.8	-830.7	104.2
Sb₂O₅	Antimony(V) oxide	-971.9	-829.2	125.1
As₂O₅	Arsenic(V) oxide	-924.9	-782.3	105.4
Co₃O₄	Cobalt(II-III) oxide	-891	-774	102.5
WO₃	Tungsten(VI) oxide	-842.9	-764	75.9
Fe₂O₃	Iron(III) oxide	-824.2	-742.2	87.4
NbO₂	Niobium(IV) oxide	-796.2	-740.5	54.5
MoO₃	Molybdenum(VI) oxide	-745.1	-668	77.7
CaO	Calcium oxide	-634.9	-603.3	38.1
Pb₃O₄	Lead(II-II-IV) oxide	-718.4	-601.2	211.3
BeO	Beryllium oxide	-609.4	-580.1	13.8
MgO	Magnesium oxide	-601.6	-569.3	27
SrO	Strontium oxide	-592	-561.9	54.4
Li₂O	Lithium oxide	-597.9	-561.2	37.6
WO₂	Tungsten(IV) oxide	-589.7	-533.9	50.5
MoO₂	Molybdenum(IV) oxide	-588.9	-533	46.3
GeO₂	Germanium(IV) oxide	-580	-521.4	39.7
BaO	Barium oxide	-548	-520.3	72.1
SnO₂	Tin(IV) oxide	-577.6	-515.8	49
TiO	Titanium(II) oxide	-519.7	-495	50

Bi₂O₃	Bismuth oxide	-573.9	-493.7	151.5
MnO₂	Manganese(IV) oxide	-520	-465.1	53.1
B₂O₂	Diboron dioxide	-454.8	-462.3	242.5
Na₂O₂	Sodium peroxide	-510.9	-447.7	95
VO	Vanadium(II) oxide	-431.8	-404.2	38.9
NbO	Niobium(II) oxide	-405.8	-378.6	48.1
Na₂O	Sodium oxide	-414.2	-375.5	75.1
MnO	Manganese(II) oxide	-385.2	-362.9	59.7
ZnO	Zinc oxide	-350.5	-320.5	43.7
Cs₂O	Caesium oxide	-345.8	-308.1	146.9
OsO₄	Osmium(VIII) oxide	-394.1	-304.9	143.9
TeO₂	Tellurium dioxide	-322.6	-270.3	79.5
SnO	Tin(II) oxide	-280.7	-251.9	57.2
KO₂	Potassium superoxide	-284.9	-239.4	116.7
GeO	Germanium(II) oxide	-261.9	-237.2	50
CdO	Cadmium oxide	-258.4	-228.7	54.8
NaO₂	Sodium superoxide	-260.2	-218.4	115.9
PbO₂	Lead(IV)oxide	-277.4	-217.3	68.6
CoO	Cobalt(II) oxide	-237.9	-214.2	53
NiO	Nickel oxide	-239.7*	-211.6*	37.99*
PbO	Lead(II) oxide (litharge)	-219	-188.9	66.5
PbO	Lead(II) oxide (massicot)	-217.3	-187.9	68.7
Al₂O	Aluminium (I) oxide	-130	-159	259.4
RuO₄	Ruthenium(VIII) oxide	-239.3	-152.2	146.4
Tl₂O	Thallium(I) oxide	-178.7	-147.3	126
Cu₂O	Copper(I) oxide	-168.6	-146	93.1
CuO	Copper(II) oxide	-157.3	-129.7	42.6
SiO	Silicon monoxide	-99.6	-126.4	211.6
HgO	Mercury(II) oxide	-90.8	-58.5	70.3
Ag₂O	Silver(I) oxide	-31.1	-11.2	121.3
AgO	Silver(II) oxide	-24.3	27.6	117
PdO	Palladium(II) oxide	-85.4	31.4	348.9
AlO	Aluminium monoxide	91.2	65.3	218.4
GaO	Gallium monoxide	279.5	253.5	231.1
InO	Indium monoxide	387	364.4	236.5

*These values were taken from Robie *et al.*⁵⁹

2.1.3. Surface composition of complex liquid gallium alloys in H₂O

In addition to several remarkable platforms mentioned in 2.1.1, gallium based liquid metal alloys have emerging applications in optics and synthesis of nano-dimensional compounds of metals.^{5, 60-69}

Section 2.1.2 explored surface composition of liquid metal alloys at interface with oxygen containing

environment. In this section, this concept will be furthered to investigate the interface with aqueous environments to produce low dimensional hydroxide and oxide hydroxides of aluminium.

Gallium can be mixed with many transition and post transition metals to produce alloys or liquid/solid metal colloids with a wide range of interesting characteristics.⁶⁹⁻⁷² Galinstan, is one such example, a non-toxic eutectic alloy containing 68.5 wt% Ga, 21.5 wt% In and 10.0 wt% Sn with a freezing point well below 0 °C.⁷³ Selected metallic elements can be incorporated onto or alloyed into galinstan itself at relatively high concentrations, leading to a vast family of liquid alloys that may be exploited.^{39, 74-75}

Wide bandgap low dimensional materials feature remarkable properties for applications in electronics, photonics, electrochemistry and many other fields.⁷⁶⁻⁷⁹ These materials can also be applied in other important areas such as membrane technologies and the strengthening of transparent polymeric composites.⁸⁰⁻⁸⁴ One such set of wide bandgap metal oxide compounds is the aluminium oxide family that are in high demand for industrial applications and, despite the abundance of aluminium in nature,⁸⁵ their environmentally friendly production into one and two dimensional (1D and 2D) morphologies have rarely been reported.

Oxide hydroxide of aluminium (boehmite γ -AlOOH) is the main component of many bauxite minerals⁸⁶ and one of the main precursors used for the production of aluminium oxides.⁸⁷⁻⁸⁸ It has been described theoretically⁸⁹ and shown experimentally^{87, 90-92} that cubic alumina (γ -Al₂O₃) adopts an orthorhombic γ -AlOOH morphology when de-hydrated. Cubic alumina is of special importance as this crystal phase of aluminium oxide can readily be transformed into other phases of Al₂O₃.⁹³⁻⁹⁴ Therefore the ability to control the morphology of γ -AlOOH *via* a green synthesis route has high industrial significance. In itself, γ -AlOOH is a very stable room temperature wide bandgap material.⁹⁵ This compound is layered and has been shown to play an important technological role in applications in medicine, composites, catalysis, ceramics, electronics and other technologies.^{92, 96-98} In addition γ -AlOOH is potentially a strong candidate for filtering applications.⁹⁸⁻¹⁰⁴ Layered oxide-hydroxides of aluminium feature various properties such as room temperature stability and high mechanical stiffness.⁹⁵ Nanostructures of γ -AlOOH, that offer high surface area, have been developed using a

variety of liquid phase techniques^{94, 105-110} However, methods of producing γ -AlOOH with large surface area involve complex synthesis processes with narrow windows to control the growth morphology. They are generally power intensive, require high temperatures, extensive processing times, or usage and/or release of toxic chemicals.

Chapter 5 of this thesis demonstrates using galinstan as a reaction solvent to dissolve aluminium and produce low dimensional aluminium hydroxide and oxide hydroxide at interface with water. The synthesis of atomically thin sheets and nanofibres of boehmite (γ -AlOOH) and their transformation into cubic alumina (γ -Al₂O₃) via annealing is explored in this thesis. The sheets are as thin as one orthorhombic boehmite unit cell. The addition of aluminium into a room temperature alloy of gallium, followed by exposing the melt to either liquid water or water vapour, allows growing either two-dimensional sheets or one-dimensional fibres, respectively. The isolated oxide hydroxides feature large surface areas, with the sheet-morphologies also showing a high Young's modulus. The method is green, since the liquid metal solvent can be fully reused. The ultrathin boehmite sheets are found suitable for the development of free-standing membrane filters that enable excellent separation of heavy metal ions and oil from aqueous solutions at extraordinary filtrate flux. The developed liquid metal-based synthesis process offers a sustainable, green and rapid method for synthesizing nano-morphologies of metal oxides which are challenging to obtain by conventional methods. The process is both sustainable and scalable and may be explored for the creation of other types of metal oxide compounds.

References

1. Gough, R. C.; Morishita, A. M.; Dang, J. H.; Moorefield, M. R.; Shiroma, W. A.; Ohta, A. T., Rapid electrocapillary deformation of liquid metal with reversible shape retention. *Micro Nano Syst. Lett.* **2015**, 3 (1), 1-9.
2. Tang, S.-Y.; Khoshmanesh, K.; Sivan, V.; Petersen, P.; O'Mullane, A. P.; Abbott, D.; Mitchell, A.; Kalantar-zadeh, K., Liquid metal enabled pump. *Proc. Natl. Acad. Sci. USA* **2014**, 111 (9), 3304-3309.
3. Bo, G.; Ren, L.; Xu, X.; Du, Y.; Dou, S., Recent progress on liquid metals and their applications. *Adv. Phys: X* **2018**, 3 (1), 1446359.

4. Adam, B. R.; Y., Z. D.; K., K. R., Liquid Metal Switches for Environmentally Responsive Electronics. *Advanced Materials Interfaces* **2017**, *4* (5), 1600913.
5. Carey, B. J.; Ou, J. Z.; Clark, R. M.; Berean, K. J.; Zavabeti, A.; Chesman, A. S. R.; Russo, S. P.; Lau, D. W. M.; Xu, Z.-Q.; Bao, Q.; Kavehei, O.; Gibson, B. C.; Dickey, M. D.; Kaner, R. B.; Daeneke, T.; Kalantar-Zadeh, K., Wafer-scale two-dimensional semiconductors from printed oxide skin of liquid metals. *Nat. Commun.* **2017**, *8*, 14482.
6. Daeneke, T.; Khoshmanesh, K.; Mahmood, N.; de Castro, I. A.; Esrafilzadeh, D.; Barrow, S. J.; Dickey, M. D.; Kalantar-zadeh, K., Liquid metals: fundamentals and applications in chemistry. *Chem. Soc. Rev.* **2018**, *47* (11), 4073-4111.
7. Dickey, M. D., Emerging applications of liquid metals featuring surface oxides. *ACS Appl. Mater. Interfaces* **2014**, *6* (21), 18369-18379.
8. Nitu, S.; Ali, Z.; Md, M.; Baoyue, Z.; Yichao, W.; S., D. R.; Paul, A.; J., C. B.; Cheng, T.; Joel, v. E.; R., C. A. S.; Zhen, O. J.; Torben, D.; Kourosh, K. z., Sonication-Assisted Synthesis of Gallium Oxide Suspensions Featuring Trap State Absorption: Test of Photochemistry. *Adv. Funct. Mater.* **2017**, *27* (43), 1702295.
9. Khoshmanesh, K.; Tang, S.-Y.; Zhu, J. Y.; Schaefer, S.; Mitchell, A.; Kalantar-zadeh, K.; Dickey, M. D., Liquid metal enabled microfluidics. *Lab Chip* **2017**, *17* (6), 974-993.
10. Sackmann, E. K.; Fulton, A. L.; Beebe, D. J., The present and future role of microfluidics in biomedical research. *Nature* **2014**, *507* (7491), 181-189.
11. Whitesides, G. M., The origins and the future of microfluidics. *Nature* **2006**, *442* (7101), 368-373.
12. Fan, X.; White, I. M., Optofluidic microsystems for chemical and biological analysis. *Nature Photon.* **2011**, *5* (10), 591-597.
13. Mitchell, P., Microfluidics - downsizing large-scale biology. To what extent has microfluidics technology fulfilled life science researchers' expectations of creating a viable "lab-on-a-chip"? *Nature Biotechnol.* **2001**, *19* (8), 717-721.
14. Elvira, K. S.; I Solvas, X. C.; Wootton, R. C. R.; Demello, A. J., The past, present and potential for microfluidic reactor technology in chemical synthesis. *Nat. Chem.* **2013**, *5* (11), 905-915.
15. Muth, J. T.; Vogt, D. M.; Truby, R. L.; Mengüç, Y.; Kolesky, D. B.; Wood, R. J.; Lewis, J. A., Embedded 3D printing of strain sensors within highly stretchable elastomers. *Adv. Mater.* **2014**, *26* (36), 6307-6312.
16. Majidi, C.; Kramer, R.; Wood, R. J., A non-differential elastomer curvature sensor for softer-than-skin electronics. *Smart Mater. Struct.* **2011**, *20* (10), 105017.
17. White, T. J.; Broer, D. J., Programmable and adaptive mechanics with liquid crystal polymer networks and elastomers. *Nat. Mater.* **2015**, *14* (11), 1087-1098.
18. Cheng, S.; Wu, Z., Microfluidic stretchable RF electronics. *Lab Chip* **2010**, *10* (23), 3227-3234.

19. Cheng, S.; Wu, Z., Microfluidic electronics. *Lab Chip* **2012**, *12* (16), 2782-2791.
20. Lu, Y.; Hu, Q.; Lin, Y.; Pacardo, D. B.; Wang, C.; Sun, W.; Ligler, F. S.; Dickey, M. D.; Gu, Z., Transformable liquid-metal nanomedicine. *Nat. Commun.* **2015**, *6*.
21. Sen, P. b.; Kim, C. J., Microscale liquid-metal switches - A review. *IEEE Trans. Ind. Electron.* **2009**, *56* (4), 1314-1330.
22. Koo, H.-J.; So, J.-H.; Dickey, M. D.; Velev, O. D., Towards all-soft matter circuits: prototypes of quasi-liquid devices with memristor characteristics. *Adv. Mater.* **2011**, *23* (31), 3559-3564.
23. Cheng, S.; Wu, Z., A microfluidic, reversibly stretchable, large-area wireless strain sensor. *Adv. Funct. Mater.* **2011**, *21* (12), 2282-2290.
24. Jeong, S. H.; Hagman, A.; Hjort, K.; Jobs, M.; Sundqvist, J.; Wu, Z., Liquid alloy printing of microfluidic stretchable electronics. *Lab Chip* **2012**, *12* (22), 4657-4664.
25. Zhang, W.; Ou, J. Z.; Tang, S. Y.; Sivan, V.; Yao, D. D.; Latham, K.; Khoshmanesh, K.; Mitchell, A.; O'Mullane, A. P.; Kalantar-Zadeh, K., Liquid metal/metal oxide frameworks. *Adv. Funct. Mater.* **2014**, *24* (24), 3799-3807.
26. Tang, S. Y.; Sivan, V.; Khoshmanesh, K.; O'Mullane, A. P.; Tang, X.; Gol, B.; Eshtiaghi, N.; Lieder, F.; Petersen, P.; Mitchell, A.; Kalantar-zadeh, K., Electrochemically induced actuation of liquid metal marbles. *Nanoscale* **2013**, *5* (13), 5949-5957.
27. Ota, H.; Chen, K.; Lin, Y.; Kiriya, D.; Shiraki, H.; Yu, Z.; Ha, T.-J.; Javey, A., Highly deformable liquid-state heterojunction sensors. *Nat. Commun.* **2014**, *5*, 5032.
28. Ladd, C.; So, J.-H.; Muth, J.; Dickey, M. D., 3D printing of free standing liquid metal microstructures. *Adv. Mater.* **2013**, *25* (36), 5081-5085.
29. Zheng, Y.; He, Z.; Gao, Y.; Liu, J., Direct desktop printed-circuits-on-paper flexible electronics. *Sci. Rep.* **2013**, *3*, 1786.
30. Hammock, M. L.; Chortos, A.; Tee, B. C. K.; Tok, J. B. H.; Bao, Z., 25th anniversary article: the evolution of electronic skin (E-Skin): a brief history, design considerations, and recent progress. *Adv. Mater.* **2013**, *25* (42), 5997-6037.
31. Palleau, E.; Reece, S.; Desai, S. C.; Smith, M. E.; Dickey, M. D., Self-healing stretchable wires for reconfigurable circuit wiring and 3D microfluidics. *Adv. Mater.* **2013**, *25* (11), 1589-1592.
32. Chrimes, A. F.; Berean, K. J.; Mitchell, A.; Rosengarten, G.; Kalantar-zadeh, K., Controlled electrochemical deformation of liquid-phase gallium. *ACS Appl. Mater. Interfaces* **2016**, *8* (6), 3833-3839.
33. Khan, M. R.; Eaker, C. B.; Bowden, E. F.; Dickey, M. D., Giant and switchable surface activity of liquid metal via surface oxidation. *Proc. Natl. Acad. Sci. USA* **2014**, *111* (39), 14047-14051.

34. Gough, R. C.; Dang, J. H.; Moorefield, M. R.; Zhang, G. B.; Hihara, L. H.; Shiroma, W. A.; Ohta, A. T., Self-actuation of liquid metal via redox reaction. *ACS Appl. Mater. Interfaces* **2016**, *8* (1), 6-10.
35. Ilyas, N.; Butcher, D. P.; Durstock, M. F.; Tabor, C. E., Ion exchange membranes as an interfacial medium to facilitate gallium liquid metal alloy mobility. *Adv. Mater. Interfaces* **2016**.
36. Fang, W.-Q.; He, Z.-Z.; Liu, J., Electro-hydrodynamic shooting phenomenon of liquid metal stream. *Appl. Phys. Lett.* **2014**, *105* (13), 134104.
37. Liu, C.; Ju, J.; Ma, J.; Zheng, Y.; Jiang, L., Directional drop transport achieved on high-temperature anisotropic wetting surfaces. *Adv. Mater.* **2014**, *26* (35), 6086-6091.
38. Kramer, R. K.; Boley, J. W.; Stone, H. A.; Weaver, J. C.; Wood, R. J., Effect of microtextured surface topography on the wetting behavior of eutectic gallium-indium alloys. *Langmuir* **2014**, *30* (2), 533-539.
39. Zhang, J.; Yao, Y.; Sheng, L.; Liu, J., Self-fueled biomimetic liquid metal mollusk. *Adv. Mater.* **2015**, *27* (16), 2648-2655.
40. Mohammed, M.; Sundaresan, R.; Dickey, M. D., Self-running liquid metal drops that delaminate metal films at record velocities. *ACS Appl. Mater. Interfaces* **2015**, *7* (41), 23163-23171.
41. Tang, X.; Tang, S. Y.; Sivan, V.; Zhang, W.; Mitchell, A.; Kalantar-Zadeh, K.; Khoshmanesh, K., Photochemically induced motion of liquid metal marbles. *Appl. Phys. Lett.* **2013**, *103* (17).
42. Sen, P.; Kim, C. J., A fast liquid-metal droplet microswitch using EWOD-driven contact-line sliding. *J. Microelectromech. Syst.* **2009**, *18* (1), 174-185.
43. Zhang, J.; Sheng, L.; Liu, J., Synthetically chemical-electrical mechanism for controlling large scale reversible deformation of liquid metal objects. *Sci. Rep.* **2014**, *4*, 8.
44. Beni, G.; Hackwood, S., Electro-wetting displays. *Appl. Phys. Lett.* **1981**, *38* (4), 207-209.
45. Sheng, L.; Zhang, J.; Liu, J., Diverse transformations of liquid metals between different morphologies. *Adv. Mater.* **2014**, *26* (34), 6036-6042.
46. Nelson, W. C.; Kim, C. J., Droplet actuation by electrowetting-on-dielectric (EWOD): A review. *J. Adhes. Sci. Technol.* **2012**, *26* (12-17), 1747-1771.
47. Junghoon, L.; Kim, C. J., Surface-tension-driven microactuation based on continuous electrowetting. *J. Microelectromech. Syst.* **2000**, *9* (2), 171-180.
48. Latorre, L.; Kim, J.; Lee, J.; De Guzman, P. P.; Lee, H. J.; Nouet, P.; Kim, C. J., Electrostatic actuation of microscale liquid-metal droplets. *J. Microelectromech. Syst.* **2002**, *11* (4), 302-308.
49. Kim, D.; Lee, J. B., Magnetic-field-induced liquid metal droplet manipulation. *J. Korean Phys. Soc.* **2015**, *66* (2), 282-286.
50. Tingyi, L.; Sen, P.; Kim, C. J., Characterization of nontoxic liquid-metal alloy galinstan for applications in microdevices. *J. Microelectromech. Syst.* **2012**, *21* (2), 443-450.

51. Lyklema, J., *Fundamentals of interface and colloid science. Volume 2: Solid-liquid interfaces*. U.S. ed. ed.; Academic Press: San Diego, 1995; Vol. 2, p 1-232.
52. Darhuber, A. A.; Troian, S. M., Principles of microfluidic actuation by modulation of surface stresses. *Annu. Rev. Fluid Mech.* **2005**, *37*, 425-455.
53. Grahame, D. C., The electrical double layer and the theory of electrocapillarity. *Chem. Rev.* **1947**, *41* (3), 441-501.
54. Frumkin, A.; Polianovskaya, N.; Grigoryev, N.; Bagotskaya, I., Electrocapillary phenomena on gallium. *Electrochim. Acta* **1965**, *10* (8), 793-802.
55. Dickey, M. D.; Chiechi, R. C.; Larsen, R. J.; Weiss, E. A.; Weitz, D. A.; Whitesides, G. M., Eutectic gallium-indium (EGaIn): A liquid metal alloy for the formation of stable structures in microchannels at room temperature. *Advanced Functional Materials* **2008**, *18* (7), 1097-1104.
56. Kim, D.; Thissen, P.; Viner, G.; Lee, D.-W.; Choi, W.; Chabal, Y. J.; Lee, J.-B., Recovery of Nonwetting Characteristics by Surface Modification of Gallium-Based Liquid Metal Droplets Using Hydrochloric Acid Vapor. *ACS Appl. Mater. Interfaces* **2013**, *5* (1), 179-185.
57. Cabrera, N.; Mott, N. F., THEORY OF THE OXIDATION OF METALS. *Reports on Progress in Physics* **1948**, *12*, 163-184.
58. Lide, D. R., CRC handbook of chemistry and physics. *12J204* **2012**.
59. Robie, R. A.; Hemingway, B. S. *Thermodynamic properties of minerals and related substances at 298.15 K and 1 bar (10⁵ pascals) pressure and at higher temperatures*; 2131; 1995.
60. Markvicka, E. J.; Bartlett, M. D.; Huang, X.; Majidi, C., An autonomously electrically self-healing liquid metal–elastomer composite for robust soft-matter robotics and electronics. *Nat. Mater.* **2018**, doi:10.1038/s41563-018-0084-7.
61. Wang, H.; Yuan, B.; Liang, S.; Guo, R.; Rao, W.; Wang, X.; Chang, H.; Ding, Y.; Liu, J.; Wang, L., PLUS-M: a porous liquid-metal enabled ubiquitous soft material. *Mater. Horizons* **2018**, *5* (2), 222-229.
62. Palleau, E.; Reece, S.; Desai, S. C.; Smith, M. E.; Dickey, M. D., Self-healing stretchable wires for reconfigurable circuit wiring and 3D microfluidics. *Adv Mater.* **2013**, *25* (11), 1589-1592.
63. Tang, J.; Zhao, X.; Li, J.; Guo, R.; Zhou, Y.; Liu, J., Gallium-based liquid metal amalgams: transitional-state metallic mixtures (TransM2ixes) with enhanced and tunable electrical, thermal, and mechanical properties. *ACS Appl. Mater. Interfaces* **2017**, *9* (41), 35977-35987.
64. Kazem, N.; Bartlett, M. D.; Majidi, C., Extreme toughening of soft materials with liquid metal. *Adv. Mater.* **2018**, *30* (22), 1706594.
65. Bilodeau, R. A.; Zemlyanov, D. Y.; Kramer, R. K., Liquid metal switches for environmentally responsive electronics. *Adv. Mater. Interfaces* **2017**, *4* (5), 1600913.
66. Kramer, R. K.; Majidi, C.; Wood, R. J., Masked deposition of gallium-indium alloys for liquid-embedded elastomer conductors. *Adv. Funct. Mater.* **2013**, *23* (42), 5292-5296.

67. Sen, P.; Kim, C. J., Microscale liquid-metal switches—A review. *IEEE Trans. Ind. Electron.* **2009**, *56* (4), 1314-1330.
68. Zavabeti, A.; Daeneke, T.; Chrimes, A. F.; O'Mullane, A. P.; Zhen Ou, J.; Mitchell, A.; Khoshmanesh, K.; Kalantar-zadeh, K., Ionic imbalance induced self-propulsion of liquid metals. *Nat. Commun.* **2016**, *7*, 12402.
69. de Castro, I. A.; Chrimes, A. F.; Zavabeti, A.; Berean, K. J.; Carey, B. J.; Zhuang, J.; Du, Y.; Dou, S. X.; Suzuki, K.; Shanks, R. A.; Nixon-Luke, R.; Bryant, G.; Khoshmanesh, K.; Kalantar-Zadeh, K.; Daeneke, T., A gallium-based magnetocaloric liquid metal ferrofluid. *Nano Lett.* **2017**, *17* (12), 7831-7838.
70. Cui, Y.; Liang, F.; Yang, Z.; Xu, S.; Zhao, X.; Ding, Y.; Lin, Z.; Liu, J., Metallic bond-enabled wetting behavior at the liquid Ga/CuGa₂ interfaces. *ACS Appl. Mater. Interfaces* **2018**, *10* (11), 9203-9210.
71. Daeneke, T.; Khoshmanesh, K.; Mahmood, N.; de Castro, I. A.; Esrafilzadeh, D.; Barrow, S. J.; Dickey, M. D.; Kalantar-zadeh, K., Liquid metals: fundamentals and applications in chemistry. *Chem. Soc. Rev.* **2018**, doi:10.1039/C7CS00043J.
72. Farrell, Z. J.; Tabor, C., Control of gallium oxide growth on liquid metal eutectic gallium/indium nanoparticles via thiolation. *Langmuir* **2018**, *34* (1), 234-240.
73. Liu, T. Y.; Sen, P.; Kim, C. J., Characterization of nontoxic liquid-metal alloy galinstan for applications in microdevices. *J. Microelectromech. S.* **2012**, *21* (2), 443-450.
74. Choi, G.; Ziebarth, J. T.; Woodall, J. M.; Kramer, R.; Sherman, D.; Allen, C. R. In *Mechanism of hydrogen generation via water reaction with aluminum alloys*, 2010 18th Biennial University/Government/Industry Micro/Nano Symposium, June 28 2010-July 1 2010; 2010; p 11431839.
75. Zavabeti, A.; Ou, J. Z.; Carey, B. J.; Syed, N.; Orrell-Trigg, R.; Mayes, E. L. H.; Xu, C.; Kavehei, O.; O'Mullane, A. P.; Kaner, R. B.; Kalantar-Zadeh, K.; Daeneke, T., A liquid metal reaction environment for the room-temperature synthesis of atomically thin metal oxides. *Science* **2017**, *358* (6361), 332-335.
76. Rogers, J. A.; Lagally, M. G.; Nuzzo, R. G., Synthesis, assembly and applications of semiconductor nanomembranes. *Nature* **2011**, *477*, 45-53.
77. Fiori, G.; Bonaccorso, F.; Iannaccone, G.; Palacios, T.; Neumaier, D.; Seabaugh, A.; Banerjee, S. K.; Colombo, L., Electronics based on two-dimensional materials. *Nat. Nanotechnol.* **2014**, *9*, 768-779.
78. Sun, Z.; Martinez, A.; Wang, F., Optical modulators with 2D layered materials. *Nat. Photonics* **2016**, *10*, 227-238.
79. Narasimhan, V.; Siddique, R. H.; Lee, J. O.; Kumar, S.; Ndjamen, B.; Du, J.; Hong, N.; Sretavan, D.; Choo, H., Multifunctional biophotonic nanostructures inspired by the longtail glasswing butterfly for medical devices. *Nat. Nanotechnol.* **2018**, doi:10.1038/s41565-018-0111-5.

80. Naskar, A. K.; Keum, J. K.; Boeman, R. G., Polymer matrix nanocomposites for automotive structural components. *Nat. Nanotechnol.* **2016**, *11*, 1026-1030.
81. Zheng, X.; Lee, H.; Weisgraber, T. H.; Shusteff, M.; DeOtte, J.; Duoss, E. B.; Kuntz, J. D.; Biener, M. M.; Ge, Q.; Jackson, J. A.; Kucheyev, S. O.; Fang, N. X.; Spadaccini, C. M., Ultralight, ultrastiff mechanical metamaterials. *Science* **2014**, *344* (6190), 1373-1377.
82. Colson, J. W.; Dichtel, W. R., Rationally synthesized two-dimensional polymers. *Nat. Chem.* **2013**, *5*, 453-465.
83. Kissel, P.; Erni, R.; Schweizer, W. B.; Rossell, M. D.; King, B. T.; Bauer, T.; Götzinger, S.; Schlüter, A. D.; Sakamoto, J., A two-dimensional polymer prepared by organic synthesis. *Nat. Chem.* **2012**, *4*, 287-291.
84. Betancur, R.; Romero-Gomez, P.; Martinez-Otero, A.; Elias, X.; Maymó, M.; Martorell, J., Transparent polymer solar cells employing a layered light-trapping architecture. *Nat. Photonics* **2013**, *7*, 995-1000.
85. Singh, S. S., The formation and coexistence of gibbsite, boehmite, alumina and alunite at room temperature. *Can. J. Soil Sci.* **1982**, *62* (2), 327-332.
86. Peintinger, M. F.; Kratz, M. J.; Bredow, T., Quantum-chemical study of stable, meta-stable and high-pressure alumina polymorphs and aluminum hydroxides. *J. Mater. Chem. A* **2014**, *2* (32), 13143-13158.
87. Bell, T. E.; Gonzalez-Carballo, J. M.; Tooze, R. P.; Torrente-Murciano, L., Single-step synthesis of nanostructured γ -alumina with solvent reusability to maximise yield and morphological purity. *J. Mater. Chem. A* **2015**, *3* (11), 6196-6201.
88. Deng, Y.; Yang, Q.; Lu, G.; Hu, W., Synthesis of γ - Al_2O_3 nanowires through a boehmite precursor route. *Ceram. Int.* **2010**, *36* (6), 1773-1777.
89. Krokidis, X.; Raybaud, P.; Gobichon, A.-E.; Rebours, B.; Euzen, P.; Toulhoat, H., Theoretical study of the dehydration process of boehmite to γ -alumina. *J. Phys. Chem. B* **2001**, *105* (22), 5121-5130.
90. Liu, S.; Chen, C.; Liu, Q.; Zhuo, Y.; Yuan, D.; Dai, Z.; Bao, J., Two-dimensional porous γ - AlOOH and γ - Al_2O_3 nanosheets: hydrothermal synthesis, formation mechanism and catalytic performance. *RSC Adv.* **2015**, *5* (88), 71728-71734.
91. Zhang, Z.; Pinnavaia, T. J., Mesosstructured γ - Al_2O_3 with a lathlike framework morphology. *J. Am. Chem. Soc.* **2002**, *124* (41), 12294-12301.
92. Shen, S.; Ng, W. K.; Chia, L. S. O.; Dong, Y.; Tan, R. B. H., Morphology controllable synthesis of nanostructured boehmite and γ -alumina by facile dry gel conversion. *Cryst. Growth Des.* **2012**, *12* (10), 4987-4994.
93. Lamouri, S.; Hamidouche, M.; Bouaouadja, N.; Belhouchet, H.; Garnier, V.; Fantozzi, G.; Trellat, J. F., Control of the γ -alumina to α -alumina phase transformation for an optimized alumina densification. *Boletín de la Sociedad Española de Cerámica y Vidrio* **2017**, *56* (2), 47-54.

94. Zhang, X.; Honkanen, M.; Levänen, E.; Mäntylä, T., Transition alumina nanoparticles and nanorods from boehmite nanoflakes. *J. Cryst. Growth* **2008**, *310* (15), 3674-3679.
95. Zhou, X.; Zhang, J.; Ma, Y.; Tian, H.; Wang, Y.; Li, Y.; Jiang, L.; Cui, Q., The solvothermal synthesis of γ -AlOOH nanoflakes and their compression behaviors under high pressures. *RSC Adv.* **2017**, *7* (9), 4904-4911.
96. Sun, B.; Ji, Z.; Liao, Y.-P.; Wang, M.; Wang, X.; Dong, J.; Chang, C. H.; Li, R.; Zhang, H.; Nel, A. E.; Xia, T., Engineering an effective immune adjuvant by designed control of shape and crystallinity of aluminum oxyhydroxide nanoparticles. *ACS Nano* **2013**, *7* (12), 10834-10849.
97. Martínez, A.; Prieto, G.; Rollán, J., Nanofibrous γ -Al₂O₃ as support for Co-based Fischer–Tropsch catalysts: pondering the relevance of diffusional and dispersion effects on catalytic performance. *J. Catal.* **2009**, *263* (2), 292-305.
98. Gao, C.; Yu, X.-Y.; Xu, R.-X.; Liu, J.-H.; Huang, X.-J., AlOOH-reduced graphene oxide nanocomposites: one-pot hydrothermal synthesis and their enhanced electrochemical activity for heavy metal ions. *ACS Appl. Mater. Interfaces* **2012**, *4* (9), 4672-4682.
99. Wei, Y.; Yang, R.; Zhang, Y.-X.; Wang, L.; Liu, J.-H.; Huang, X.-J., High adsorptive γ -AlOOH(boehmite)@SiO₂/Fe₃O₄ porous magnetic microspheres for detection of toxic metal ions in drinking water. *Chem. Commun.* **2011**, *47* (39), 11062-11064.
100. Salem, M.; Sharawy, H.; Ossman, M., Kinetics modeling and Adsorption isotherm studies for Cr(III) removal using Boehmite Nano-powder. *Int. J. Chem. Biol. Sci.* **2013**, *3*, 9-18.
101. Hota, G.; Kumar, B. R.; Ramakrishna, W. J. N. S., Fabrication and characterization of a boehmite nanoparticle impregnated electrospun fiber membrane for removal of metal ions. *J. Mater. Sci.* **2008**, *43* (1), 212-217.
102. He, T.; Xiang, L.; Zhu, S., Hydrothermal preparation of boehmite nanorods by selective adsorption of sulfate. *Langmuir* **2008**, *24* (15), 8284-8289.
103. Zhang, Y.-X.; Yu, X.-Y.; Jin, Z.; Jia, Y.; Xu, W.-H.; Luo, T.; Zhu, B.-J.; Liu, J.-H.; Huang, X.-J., Ultra high adsorption capacity of fried egg jellyfish-like γ -AlOOH(Boehmite)@SiO₂/Fe₃O₄ porous magnetic microspheres for aqueous Pb(II) removal. *J. Mater. Chem.* **2011**, *21* (41), 16550-16557.
104. Tang, W. P.; Shima, O.; Ookubo, A.; Ooi, K., A kinetic study of phosphate adsorption by boehmite. *J. Pharm. Sci.* **1997**, *86* (2), 230-235.
105. Márquez-Alvarez, C.; Žilková, N.; Pérez-Pariente, J.; Čejka, J., Synthesis, characterization and catalytic applications of organized mesoporous aluminas. *Cataly. Rev.* **2008**, *50* (2), 222-286.
106. Baumann, T. F.; Gash, A. E.; Chinn, S. C.; Sawvel, A. M.; Maxwell, R. S.; Satcher, J. H., Synthesis of high-surface-area alumina aerogels without the use of alkoxide precursors. *Chem. Mater.* **2005**, *17* (2), 395-401.
107. Xiang Ying, C.; Hyun Sue, H.; Soon, W. L., Hydrothermal synthesis of boehmite (γ -AlOOH) nanoplatelets and nanowires: pH-controlled morphologies. *Nanotechnology* **2007**, *18* (28), 285608.

108. Bell, T. E.; Gonzalez-Carballo, J. M.; Tooze, R. P.; Torrente-Murciano, L., γ -Al₂O₃ nanorods with tuneable dimensions - a mechanistic understanding of their hydrothermal synthesis. *RSC Adv.* **2017**, *7* (36), 22369-22377.
109. Gan, Z.; Ning, G.; Lin, Y.; Cong, Y., Morphological control of mesoporous alumina nanostructures via template-free solvothermal synthesis. *Mater. Lett.* **2007**, *61* (17), 3758-3761.
110. Osman, A. I.; Abu-Dahrieh, J. K.; McLaren, M.; Laffir, F.; Nockemann, P.; Rooney, D., A facile green synthetic route for the preparation of highly active γ -Al₂O₃ from aluminum foil waste. *Sci. Rep.* **2017**, *7* (1), 3593.

Chapter 3

Ionic imbalance induced self-propulsion of liquid metals[†]

3.1. Introduction

In this chapter, the author of the thesis presents the investigation on the surface manipulations of liquid metals by modification of the liquid electrolyte surrounding it. Galinstan, which is a eutectic alloy of gallium, is used as the model liquid metal. Gallium has low toxicity, negligible vapour pressure and is relatively safe for practical applications¹. Gallium itself melts above room temperature at 29.8°C, however when combined with other metals its melting point can be significantly lowered below 0°C such as is the case with Galinstan, which is a eutectic alloy of 68.5% gallium, 21.5% indium and 10% tin². The pH of the electrolyte is modified by adding acidic or basic solutions and the ionic properties of the electrolyte are adjusted through the addition of a salt. The author will show that maintaining a gradient in the electrolyte properties across a liquid metal droplet results in continuous mechanical motion and deformation. The device is characterised to determine the required conditions for self-propulsion, and the ionic imbalance requirements are optimised and tested. Two key applications that illustrate pumping and switching effects are also presented. This work represents the

[†] The contents of this chapter is published in Zavabeti et al., Ionic imbalance induced self-propulsion of liquid metals, *Nature Communications*, 7, 12402, 2016

first steps in building a self-propelling liquid metal droplet, which can be controlled with a fluid only, thereby marking a significant advancement towards truly autonomous soft systems. The content of this chapter was published as an article in the journal of Nature Communications³.

3.2. Experimental details

3.2.1. Ionic Imbalance Framework

For the experiments presented in Figs 3.1 to 3.9, a Fusion 720 dual syringe pump was used to dispense acid and base at a steady flow rate of 200 $\mu\text{L}/\text{min}$ and a PHD 2000 Harvard syringe pump was used to infuse at a steady flow rate of 400 $\mu\text{L}/\text{min}$. The effect of flow viscosity on droplets is assumed negligible. Inlet flow was regulated through a narrow orifice opening fabricated to avoid any inlet flow irregularities before sweeping across to the droplet. Video recording analysed with a developed image processing program in Matlab program to facilitate assessing the dynamics of the droplet. Cone shaped UV and blue light wavelength band pass filters attached to a camera lens to enclose droplet and mitigate light energy absorption. Photos and video recordings have a green reflection of the droplet surface facing the camera.

3.2.2. Voltage Characterization

In Fig. 3.10, the recess and its walls are coated with Teflon to form a hydrophobic surface. Hydrophobicity avoids wetting of the intermediate surface by ionic solutions, which are an electrical conductor, which can bypass the EDL capacitor. Copper electrode tips are amalgamated with Galinstan to avoid generation of battery cells in between the droplet and electrodes. The two channels are completely segregated to ensure the voltage drop occurs only on the liquid metal droplet. Electrolyte levels inside each channel were identical and lower than the droplet surface.

3.2.3. Self-propelling Droplet

In Fig. 3.11 to 3.13, a perfluoroalkoxy (PFA) tube is cut in half using a milling machine to make a semi-cylindrical channel. Then the PFA semi-cut tube is coated with dry film Teflon spray to bring down the friction force and enhance the mobility of the droplet. Each reservoir is filled with 9 ml of solution. 113 mg of Galinstan liquid metal is separated into two smaller droplets and placed inside the

channel. Then each droplet is connected to either of the reservoirs. The droplets are then merged. Separation of the droplets minimizes mixing of the ionic solutions at the start of the experiments.

3.3. Results and Discussions

3.3.2. *pH imbalance*

The first experiments were conducted to observe the dynamics of a liquid metal when two different electrolytes of varying pH were placed on each side of the droplet. An open-top fluidic channel was fabricated by milling polymethyl methacrylate (PMMA) as shown in Fig. 3.1c. A liquid metal droplet was placed in a spherical recess located in between two different flowing electrolytes of acidic and basic nature (dyed in different colours for easy identification – very low concentration food dyes). This liquid metal droplet (3 mm in diameter) nearly filled the recess, effectively reducing the mixing between the two electrolytes. Some of the effects of droplet size variations are presented in Fig. 3.2. The set-up was designed in a way that the effect of electrolytes on the droplet, causing symmetry breaking, could be readily observed using a camera. The camera recorded the presence of deformation or surface flow during the experiments, which was the main information that was required for this study. Constraining the droplet in the recess allows one to study its deformation and surface flow dynamics without any displacement. A continuous flow of electrolyte was important as it provided a fresh supply of ions to the liquid metal surface, and cleansed the surroundings of the droplet from any undesired chemical by-products and bubbles. Flow rates were set to a low value of 200 $\mu\text{L}/\text{min}$ in each channel to ensure a laminar flow with a Reynolds number of 2.2. This value was sufficiently high to avoid mixing of the electrolytes within the two channels. More detail on materials and methods are available in section 3.2.1.

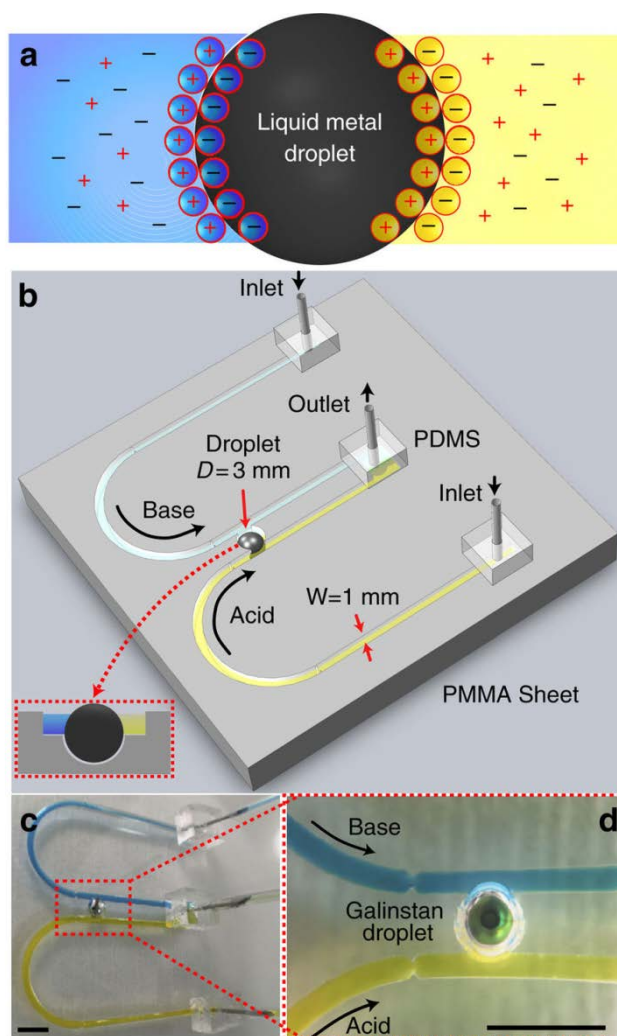


Figure 3.1. EDL schematic and experimental framework for analysing liquid metal droplet dynamics under ionic imbalance. (a) Top view schematic of the droplet and arrangement of ions, forming the EDL. (b) Schematic of the experimental setup showing two U-shaped open-top (see inset) PMMA inlet channels which extend in parallel and join at an outlet. Two channels carry different types of electrolytes represented in distinct colours, acidic in yellow and basic in blue. Two parallel flows come in contact with the Galinstan droplet of 3 mm diameter residing in a recess. (c) Actual experimental set up. (d) Close up view of c. Scale bars are 5 mm.

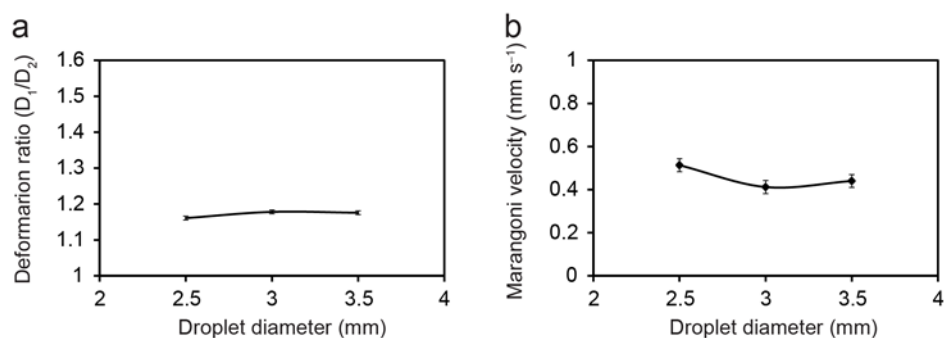


Figure 3.2. Effect of the droplet size on droplet dynamics. (a and b) In three sets of experiments with varying droplet diameter, dynamics of the droplet in deformation dominant regions did not change significantly. Molarities are constant at 2.4 mol L^{-1} acid and 0.3 mol L^{-1} of base. Error bars indicated s.e.m. ($n=6$).

3.3.3. Droplet dynamics under pH imbalance

The diagram in Fig. 3.3 represents the droplet dynamics when a liquid metal droplet is placed in between acidic (HCl) and basic (NaOH) electrolytes. Experiments were conducted at varying concentrations of NaOH and HCl as illustrated in Fig. 3.3c. Droplets were observed to have two dynamics: (a) deformation and (b) Marangoni flow.

To trigger a change in the dynamics of a droplet, a minimum pH difference across the liquid metal of ~ 13 was required. Therefore, during these experiments each hemisphere of the droplet was exposed to a minimum of 0.3 mol/L NaOH (pH of ~ 13.5) and 0.3 mol/L HCl (pH of ~ 0.5), respectively. Above 3 mol/L , significant changes in the chemistry of the system was observed and the functionality was disrupted.

3.3.4. Deformation of liquid metal droplets

The first dynamic component was due to the deformation (extension and compression) of the liquid metal droplet at the interface with the electrolyte as described by equation (2.2). Deformation was observed as a change in shape of the droplet indicating a pressure imbalance between the two

opposing hemispheres of the droplet (Fig. 3.3a). Each hemisphere formed a different curvature corresponding to its interfacial pressure deviation exposed to each of the electrolytes. As the flow was equal on both sides, there was no pressure deviation induced by electrolyte flow. Thus, the pH imbalance induced the pressure deviation on the two sides of the droplet, which resulted in a displacement of liquid metal from the HCl side (high surface tension) towards the NaOH (low surface tension) electrolyte. Since the droplet movement was restricted by the recess, the liquid metal deformed towards the NaOH channel leading to an extended diameter (D_1) in one direction and a compressed diameter (D_2) in the other axis perpendicular to the direction of extension. It is referred to the aspect ratio between the two axes as 'deformation ratio', $\frac{D_1}{D_2}$. Measured deformation ratios in Fig. 3b, varied from 1 to 1.46.

3.3.5. Marangoni flow of liquid metal droplets

The second observed dynamic component was due to the Marangoni flow effect. Marangoni flow was observed as the mass transfer of liquid on the surface of the droplet, which was driven by the induced surface tension gradient ⁴ (Fig. 3.3b). Marangoni flow was measured with tracking the starch micro particles that were added to the electrolytes on the surface of the droplet. The flow induced by the ionic imbalance was initiated from the interfacial region with lower surface tension (NaOH) towards the region with higher surface tension (HCl). The surface Marangoni flow path was observed along the outer curvature of the surface of the droplet outside the electrolyte (Fig. 3.3b). Marangoni flow rate ranges during the pH experiments in Fig. 3.3 were found to span from 0 to a maximum of 1.74 mm/s. Some small micro particles were added in the electrolytes to facilitate the observations of the Marangoni flow for velocity measurements as per previous work ⁵. The conditions that define the Marangoni flow dynamics of a droplet are presented in Fig. 3.3 and Fig. 3.4.

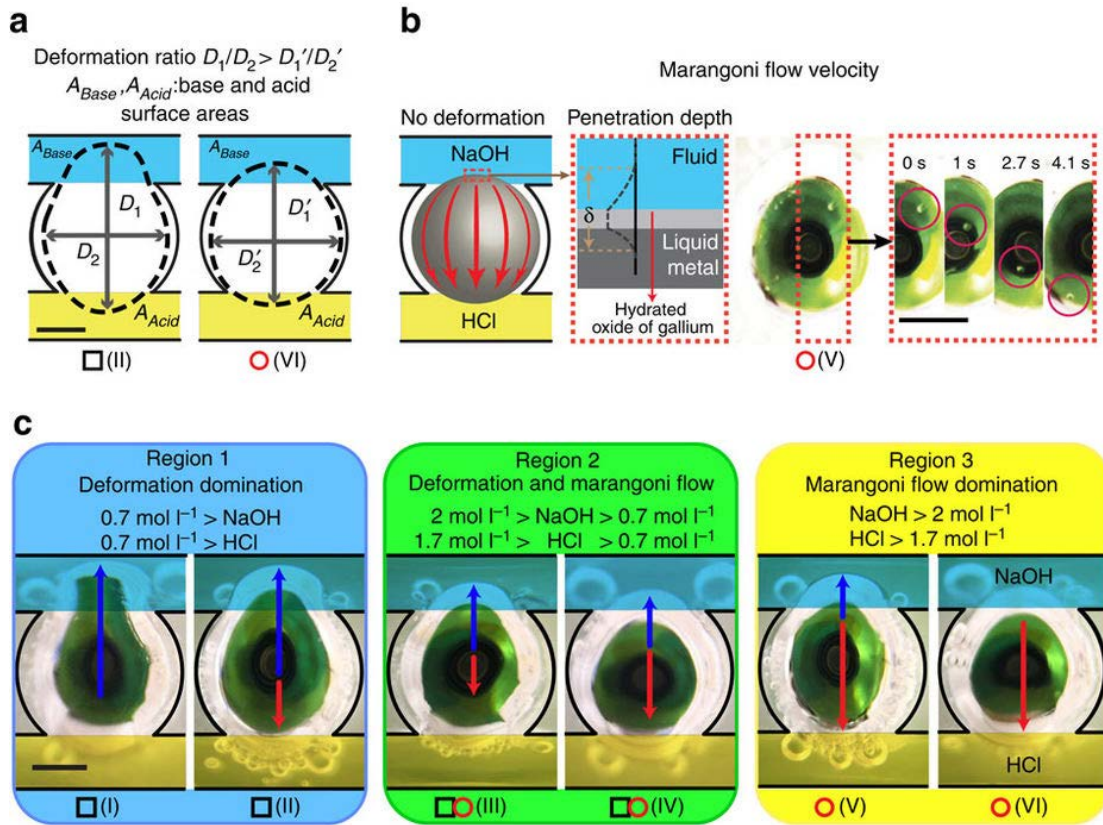


Figure 3.3. Reference diagram of the dynamics of the liquid-metal droplets under different HCl and NaOH concentrations. (a) Schematic of the deformation ratio measurements for D_1/D_2 assessment. ‘Black square’ indicates experiments with deformation dominating the dynamics and Marangoni flow dominant experiments are represented by ‘red circles’. (b) Demonstration of Marangoni flow and sequential snapshots shows a micro particle transferring from NaOH to HCl. The tangential skin flow displaced component, as a result of the Marangoni effect, contains a Galinstan layer near the surface of the droplet, an oxide layer and a layer of electrolyte also near the surface. A thickness of δ is used to define the effective thickness of this layer. (c) Selected enlarged images showing droplet deformation (in black arrows) towards NaOH while Marangoni flow (in red arrows) direction is towards HCl. Scale bars are 1 mm.

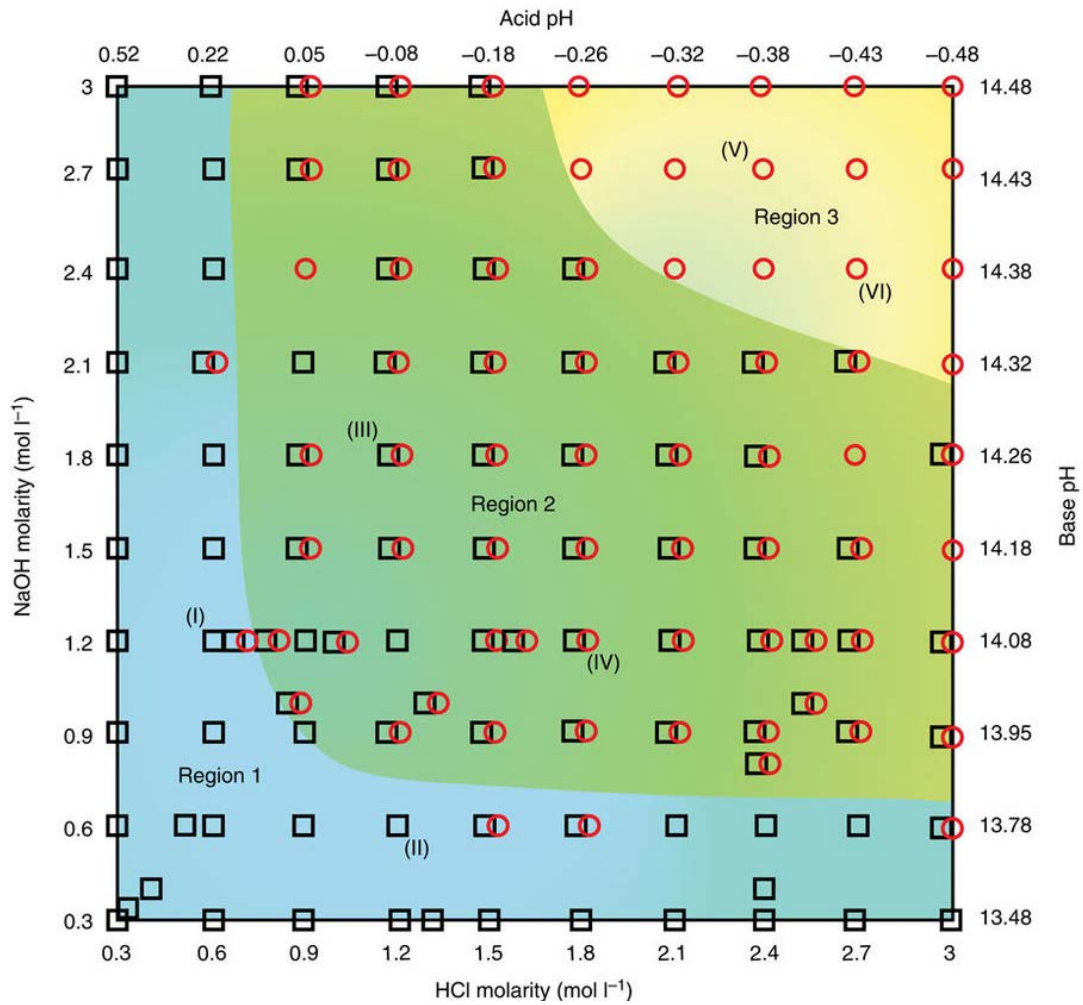


Figure 3.4. Reference diagram of liquid metal droplet dynamics under a pH imbalance. Each ‘black square’ or ‘red circle’ presents an experiment with measurable deformation ratio or Marangoni flow, respectively (overlapped ‘black square’ and ‘red circle’ indicates experiments with both measurable Marangoni flow and deformation ratios without a distinct dominating effect), in various ionic concentrations of HCl and NaOH between 0.3 to 3 mol/L (pH of ~ 0.5 to ~ -0.5 for HCl and ~ 13.5 to ~ 14.5 for NaOH respectively). The background of the reference diagram is coloured blue, green and yellow accordingly, to represent each of the regions (deformation, deformation-Marangoni, and Marangoni regions) discussed in the text.

An important observation is regarding the formation of thin flakes and their apparent effect on the Marangoni flow. At relatively high acidic and basic concentrations, it is seen that oxide flakes of triangular configurations are formed on the surface of the liquid metal droplet (Fig. 3.5a). These flakes increasingly become thicker when the concentration of the electrolyte increases (almost 4-5 times thicker when NaOH or HCl molar concentration increase by an order of magnitude according to Raman spectroscopy assessments as presented in the Fig. 3.5b). It seems that when these flakes (which are made of hydrated oxides of gallium) become thicker, they eventually delaminate into the electrolyte or move along together with the Marangoni flow (Fig. 3.5c). The presence of the thick hydrated oxides seems to be an important reason for the dominance of Marangoni flow and reduction of the deformation effect. The flakes form a solid skin (either attached or delaminated) that contains the droplet and reduces the deformation effect.

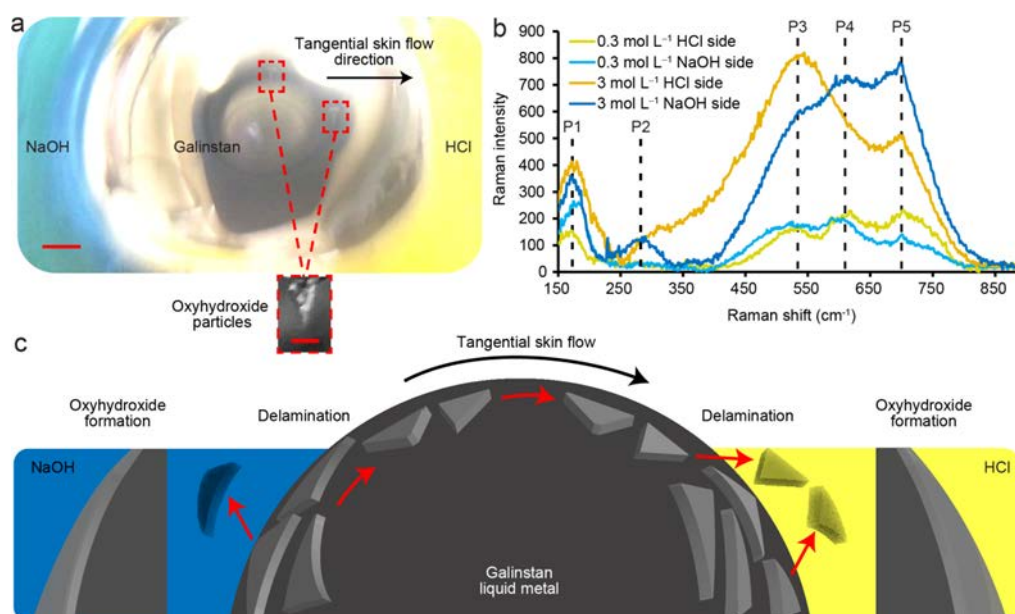


Figure 3.5. Galinstan surface oxidation in high molarities of acid and base. (a) At high HCl and NaOH concentrations, relatively large and thick oxides flakes are formed on the surface of droplets and delaminated. These flakes move along the surface of Galinstan droplet toward the acidic side. The oxide flakes can be mechanically exfoliated simply by tweezers (inset). Scale bars are 0.5 and 0.1 mm in a and inset respectively. (b) To understand the composition and nature of the oxide flakes, the

surface of the two sides of the droplet were analysed using Raman microspectroscopy. Results indicate five distinct peaks (P1-5) matching Raman spectra of α -gallium oxyhydroxide⁶. The peaks' intensities increased significantly when droplet was exposed to higher imbalanced concentrations, which indicates the formation of much thicker α -gallium oxyhydroxide flakes (at least 4-5 times thicker comparing 0.3 and 3 mol L⁻¹ concentrations if the relation is considered linear). Peak intensities are different for skins in NaOH and HCl areas due to the difference of hydration and surface charges. Due to the damping effect of liquid metal under the surface of flakes, peaks located in wavenumbers lower than 500 cm⁻¹ are weakened. (c) In higher molarities of electrolytes, thicker layers of α -gallium oxyhydroxide flakes form on the NaOH side of the droplet. These thick layers delaminate from the surface, with the help of bubbles that are produced by the chemical reactions on the surface of droplet and move toward the HCl side under the effect of surface tension difference. This causes a tangential skin flow. These flakes are eventually released into the aqueous solution as the effect of the flow in the channels.

3.3.6. Dynamics regions

The reference diagram shown in Fig. 3.4 summarizes the dynamics of the droplets, according to which the diagram can be divided into three regions. Region 1 features experimental conditions that resulted in droplet dynamics dominated by deformation. The droplet was found to strongly stretch towards the NaOH electrolyte with deformation ratios of up to 1.46, while Marangoni flow was less noticeable (less than 0.2 mm/s). The experimental conditions resulting in region 1 type dynamics were found to require comparatively low concentrations of one of the electrolytes in which either hemisphere was exposed to ionic concentrations of 0.3 mol/L to 0.7 mol/L (pH of \sim 0.5 to \sim 0.2 and \sim 13.5 to \sim 13.9 for HCl and NaOH, respectively) (Fig. 3.3c). Region 2 summarizes the experimental conditions for which a droplet exhibited simultaneous measurable deformation and Marangoni flow (Fig. 3.3c). As per Fig. 3.4, the region is featured as curved and confined areas defined by the concentrations of NaOH between 0.7 mol/L and 1.7 mol/L (pH of \sim 13.9 to \sim 14.2) and HCl between 0.7 mol/L and 2 mol/L (pH of \sim 0.2 to \sim -0.3). Region 3 is the area dominated by Marangoni flow

(Fig. 3.3c). Increasing both NaOH and HCl concentrations to above 1.7 and 2 mol/L (pH of ~14.2 and ~ -0.3 for HCl and NaOH, respectively) (Fig. 3.4), respectively, enhances the induced Marangoni flow (up to a maximum 1.74 mm/s) while reducing the deformation ratios (to a maximum of 1.1).

Altogether, the results show that a low differential pH results in deformation toward the basic solution while a large differential pH induces high Marangoni flows toward the acid solution, which counters the deformation process.

It seems that the deformation process can be repeated for a substantial time period (I repeated it for more than a week with no apparent change in performance). Days of operation did not dampen the deformation effect. However, the longevity in the Marangoni region seems to be significantly shorter (less than several hours of perfect repeatability).

The difference can be associated to the fact that the skin formed on the surface is very thin during the deformation process (several nm) and consequently a very small amount of Galinstan is chemically used in the process. However, in the Marangoni flow region the surface is much thicker, delaminates and leaves the droplet, which, in time, reduces the mass of the droplet.

To further examine the effect that the presence of a surface skin has on the establishment of the Marangoni flow, a set of experiments were conducted using mercury droplets (Fig. 3.6). For mercury, hardly any surface oxide skin was observed after exposure to acidic and basic electrolytes. Interestingly, no Marangoni flow was observed for mercury droplets at the same concentrations where strong Marangoni flow was seen for Galinstan droplets.

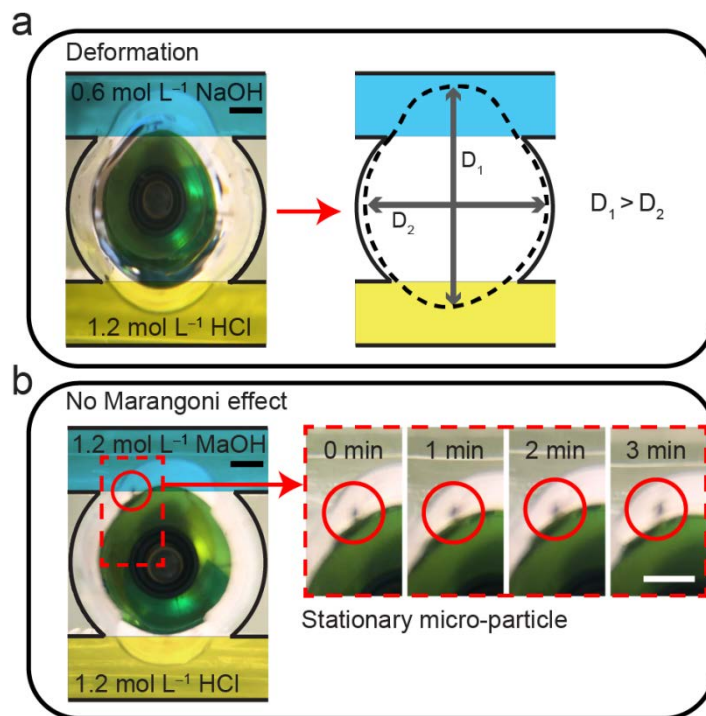


Figure 3.6. Mercury droplet dynamics under ionic imbalance. (a) At low concentrations of electrolyte, droplet deformation is observed, similar to that of Galinstan. (b) At high concentrations of electrolytes, the mercury droplet does not exhibit any tangential skin flow due to Marangoni effect, as opposed to the Galinstan liquid metal. This is evidenced as the micro particles deposited over the surface of mercury droplet remain stationary. Scale bars are 0.5 mm.

Experiments were conducted to observe the effects of the changes in the differential pH across the droplet. Figure 3.6a and b illustrate the deformation and Marangoni flow of the droplet when the pH was kept constant in one of the channels (a concentration of 2.4 mol/L produces a solution with a pH of ~ -0.4 and ~ 14.4 for HCl and NaOH respectively) and the molarity of the electrolyte was changed in the other channel. 2.4 mol/L was chosen as it covers a typical band for the three regions shown in Fig. 3.3c.

The experiments indicate that the pH gradient has a significant effect on both deformation and Marangoni flow. Within region 2, the deformation ratio decreases almost linearly when the molarity is increased (black line in Fig. 3.7a and b) and at the same time the Marangoni flow rate increases (red line). Additional measurements on other acid and base types (e.g. H_2SO_4 and KOH) are presented in Fig. 3.8.

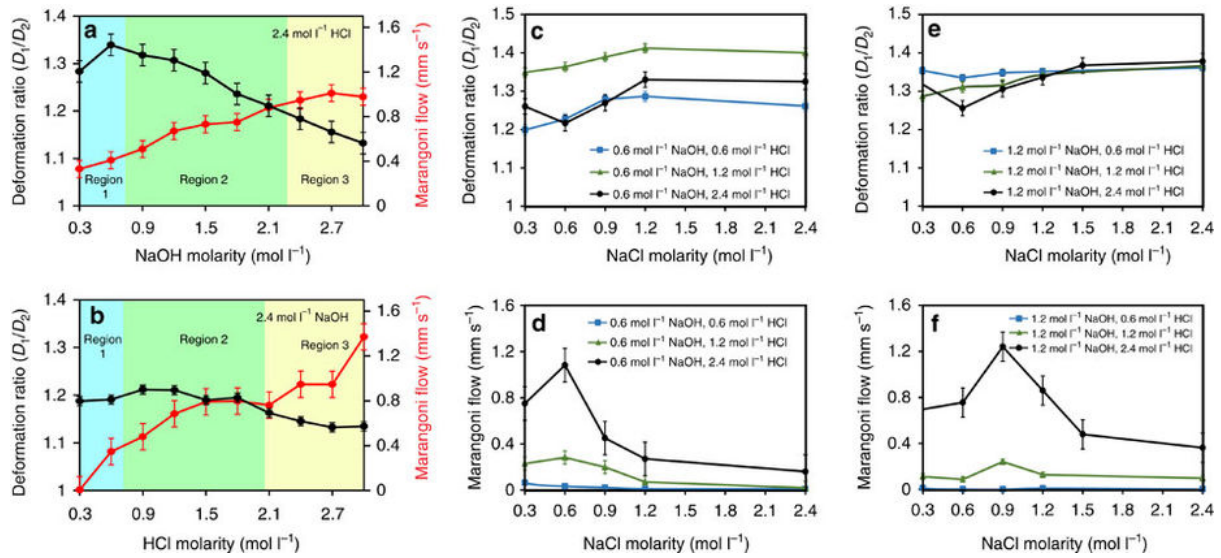


Figure 3.7. Changes of deformation and Marangoni flow under different conditions. **(a)** Graph of the experimental measurements with varying NaOH and constant HCl molarities. **(b)** Graph of the experimental measurements with varying HCl and constant NaOH molarities. Black and red lines indicate droplet deformation ratio and Marangoni flow rates respectively. Background colours correspond to regions of the reference diagram in Fig. 3.4. Error bars are s.e.m. ($N=6$). **(c-f)** Graphs present the deformation ratio and Marangoni flow in varying concentrations of NaCl while concentrations of NaOH and HCl are kept constant. NaCl is mixed with NaOH in all experiments. Error bars are s.e.m. ($N=6$).

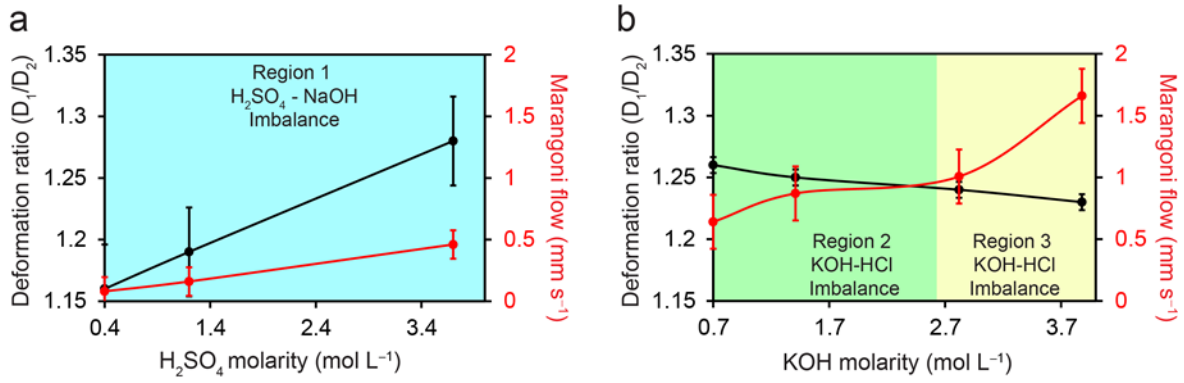


Figure 3.8. Effect of pH imbalance of different acid and base solutions on droplet dynamics. (a) Varying concentration of H_2SO_4 is used with constant 0.3 mol L^{-1} of NaOH. As expected, droplet deformation was more dominant. Background is coloured in blue to indicate the droplet is operating in region 1 of the reference diagram of Fig. 3.4. (b) Region 2 and 3 are tested with varying concentration of KOH and constant concentration of 3.4 mol L^{-1} HCl. The Marangoni dominant region is shifted to higher concentrations of KOH solution than that of NaOH.

3.3.7. Effect of mixed salt concentration on liquid metal droplet dynamics

In these experiments, the change of maximum surface tension at the PZC is not separable from the effect of the pH change. To further understand the effect of the maximum surface tension at the PZC change and the accumulated charges in the EDL, several experiments were conducted by keeping both the acid and base concentration at set points, while changing the ionic concentration via the addition of a neutral salt. The salt chosen here was NaCl, which completely ionizes in water. The outcomes of these measurements are presented in Fig. 3.7c-f and Fig. 3.9, in which the effect of NaCl concentration is shown at constant sets of acidic and basic molarities in the respective channels.

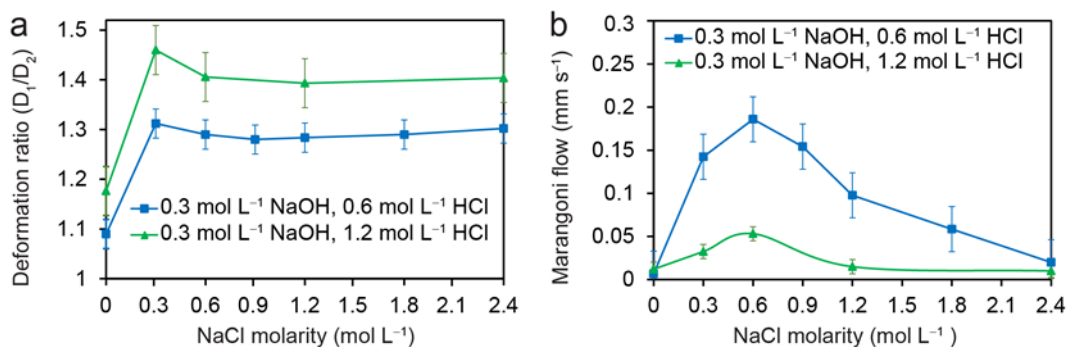


Figure 3.9. Droplet dynamics under imbalanced mix ionic solution of low NaOH molarity. NaCl mixed solutions are prepared in low molarities of 0.3 mol L⁻¹ NaOH. HCl is kept constant at 0.6 mol L⁻¹. Error bars indicated s.e.m. (n=6). (a and b) Graphs present deformation ratio and Marangoni flow in varying concentrations of NaCl while concentrations of NaOH and HCl are kept constant. NaCl is mixed with NaOH in all experiments. In a Maximum deformation is seen in 0.3 mol L⁻¹ of NaCl while Marangoni flow maximum in b is located at 0.6 mol L⁻¹ of NaCl.

At 0.6 mol/L NaOH and three different concentrations of HCl (0.6, 1.2 and 2.4 mol/L), deformation increases almost linearly by increasing [NaCl] from 0.3 to 1.2 mol/L (Fig. 3.7c and d). The deformation of the droplet reached a saturation value after this point. Interestingly, the highest extent of deformation was seen at 1.2 mol/L HCl. When the NaOH concentration was increased to 1.2 mol/L significant deformation of the droplet was already occurring in even the lowest concentration of NaCl and the changes were comparatively less prominent.

As mentioned in the previous section, for HCl concentrations of less than 0.6 mol/L the Marangoni flow is negligible. At higher concentrations of HCl, the Marangoni flow consistently shows a distinct peak when the NaCl concentration changes. Interestingly the location of this peak is a function of the NaOH concentration, however is not affected by a change of NaCl concentration. After this peak, the Marangoni flow decreases. It seems that at high NaCl concentrations, the mixing may be more extensive and, as a result, more NaCl is transferred to the HCl channel reducing the flow. There can

also be a competition between the adsorption of Cl^- and OH^- ions. The OH^- ions changes the pH of the solution which alters the voltage gradient that can adversely affect the adsorption of Cl^- ions.

For HCl kept at three constant values of 0.6, 1.2 and 2.4 mol/L and when NaOH is at 2.4 mol/L (Fig. 3.7e and f), deformation starts at a higher magnitude in the non-saturated regions. The behaviour of Marangoni flow is similar to 0.6 mol/L NaOH but the peak is shifted towards higher NaCl concentrations.

If NaCl is added to HCl no deformation and Marangoni flow is observed. It seems that the competition between Na^+ and H^+ is counterproductive for both effects. Unfavourable effects of salt mixtures with some electrolytes on the EDL has been explained previously by Lyklema⁷ and Davies⁸.

3.3.8. Voltage characterizations

To verify and characterize the effect of the maximum surface tension at the PZC, the dynamics of droplets are investigated by applying an external electrical potential. Changing the potential changes the potential difference gradient across the EDL along the interface between the droplet and the electrolyte. This changes the surface tension gradient and as a result, both the deformation and Marangoni flows are altered. The set-up is shown in Fig. 3.10a. Both electrodes are Galinstan amalgamated metals that cannot be deformed. The EDL is manipulated by the applied voltage and its effect on the maximum surface tension can be assessed by the observation of deformation and surface flow (Fig. 3.10b).

The channels were filled with acidic, basic, and salt solutions of the same concentrations to analyse the effect of applied voltage in different electrolytes. The measurement outcomes are presented in Fig. 3.10c and d. Five different conditions were shown for comparison. Molar concentrations of 0.6 mol/L NaOH and 1.2 mol/L HCl are shown to exhibit maximum deformation and relatively small Marangoni flow (Fig. 3a-d), which was confirmed by experiments in Fig. 3.10c and d.

When the applied voltage is increased the deformation ratios reaches peaks of >1.25 in all cases. The peak reaches the maximum at a voltage of 1.5 V for HCl only, while the peak is significantly shifted to 2.1 V for NaOH only. Adding NaCl to HCl and NaOH shifts the peaks to the middle area between these two voltages to 1.7 and 1.9 V, respectively. This means the location of the maximum surface tension at the PZC is influenced by mixing salt ions which, interestingly, shifts both the HCl and NaOH peaks almost symmetrically. The order of the appearance of the peaks shown in Fig. 3.10c is in agreement with observations by Grahame on mercury ⁹. The peak voltage shifts are also comparable with what is seen for mercury ⁹⁻¹⁰ and liquid gallium ¹¹.

Marangoni flow velocity increases with an increase in the applied voltage and has a different set point for each electrolyte. The set point is lower for HCl (0.8 V) and significantly increases for NaOH (1.7 V). Similar to the deformation curves, solutions containing NaCl shift the Marangoni flow velocity to the middle, to 1 and 1.6 V for HCl and NaOH solutions, respectively that contain NaCl. Marangoni flow velocity is much higher for HCl, almost an order of magnitude larger than that of NaOH.

Assuming a constant differential EDL capacitance, the surface tension of Galinstan (Fig. 3.10e) can be readily obtained by applying the integrated Lippmann equation (equation (2.1)) at each PZC of the ionic solutions. The peak locations are obtained from experimental measurements. As can be seen, the calculated surface tension changes are proportionally related to the deformation ratio changes as a function of voltage, which is the expected observation. The parameters used are presented in Table 3.1.

Table 3.1. Ionic coefficients: List of experimental measurements of the Marangoni flow coefficient α , threshold potential φ_{Th} and potential of zero charge φ_0 . R^2 is the coefficient of determination of the linear regression trend line gradient of the Marangoni flow velocity against potential.

	1.2 mol L ⁻¹ HCl	0.6 mol L ⁻¹ HCl	0.3 mol L ⁻¹ HCl + 0.3 mol L ⁻¹ NaCl	0.3 mol L ⁻¹ NaOH + 0.3 mol L ⁻¹ NaCl	0.6 mol L ⁻¹ NaOH
α (mm/v s ⁻¹)	1.8218 ($R^2 = 0.93$)	6.3857 ($R^2 = 0.89$)	3.9984 ($R^2 = 0.98$)	0.3048 ($R^2 = 0.89$)	0.2621 ($R^2 = 0.94$)
φ_{Th} (v)	1	0.8	1	1.6	1.7
φ_0 (v)	1.4	1.5	1.7	1.9	2.1

For deformation region, the capacitance energy of the droplet due to ionic imbalance over the two sides of the droplet converts into mechanical energy, which induces droplet propulsion and tangential skin flow. The capacitance energy can be obtained using the integrated Lippmann equation (equation (2.1)) at each side of the droplet, as:

$$E_{\text{Unit area}} \cong \frac{1}{2} \left[\underbrace{C(\varphi - \varphi_0)^2 A}_{\text{Acid}} + \underbrace{C(\varphi - \varphi_0)^2 A}_{\text{Base}} \right] / A_{\text{Total}} \quad (3.1)$$

where φ is the applied surface potential, φ_0 is the PZC, and A is the surface area of each semi-sphere exposed to acidic and basic electrolytes. Here, A_{Total} is the total surface area of the droplet.

The equation describes that the two sides of the droplets can be independently affected by changing the acid and base concentrations. The asymmetry breaking is then a function of the total EDL energy of the two sides.

For the Marangoni region, Fig. 3.10f is the simulated representation for the kinetic energy of Marangoni flow per unit area. This is obtained using the following equations:

$$E_{Unit\ area} \cong \frac{1}{2} \int d\left(\frac{m_s U_s^2}{A_s}\right) \quad (3.2)$$

$$E_{Unit\ area} \cong \frac{1}{2} \delta \rho_s \alpha^2 (\varphi - \varphi_{Th})^2 \quad \text{for } \varphi > \varphi_{Th} \quad (3.3)$$

Here m_s is the displaced mass (this mass is made of surface liquid of the Galinstan, liquid in its vicinity and delaminated skin oxide layer in Figs 3.3b and 3.4c), U_s is the skin tangential flow velocity generated by the Marangoni effect, A_s is the surface area of the moving layer, ρ_s is the density of the displaced mass, δ is the effective thickness of the displaced layer (Fig. 3.3b) at the interface of liquid metal (which also includes the surface oxide skin), α is the ionic liquid constant which is a function of gradient of Marangoni flow against potential (Table 3.1), φ is the applied external potential, φ_{Th} is the threshold for the applied external potential for the ionic liquid in which Marangoni flow starts. The discussion regarding the derivation of this equation is presented in next section. It is important to consider that this equation can also be extracted from the general Lippmann equation.

The main observation is that after fitting the voltage thresholds, Marangoni flow velocity graphs and the calculated kinetic energies trends are proportionally related.

3.3.9. Energy calculations of the surface Marangoni flow

Induced Marangoni flow of the liquid metal was measured on the surface of the droplet at different applied potentials and concentrations of ionic solution. In order to calculate the surface tension gradient, which causes the Marangoni flow, the kinetic energy of the flow is calculated first. It is

assumed negligible viscous losses at the air/droplet interface. In Marangoni dominant regions, the droplet is approximately spherical $\frac{D_1}{D_2} \cong \frac{R}{R} = 1$ (in which R is droplet radius) then:

$$E_{Unit\ Area} = \frac{\partial E_{Kinetics}}{\partial A_s} = \frac{1}{2} \left(\frac{\partial m_s u_s^2}{\partial A_s} \right) = \frac{1}{2} \left(\frac{\partial A_s \delta \rho_s u_s^2}{\partial A_s} \right) = \frac{1}{2} \delta \rho_s u_s^2 \quad (3.4)$$

where $\partial E_{Unit\ Area}$ denotes the kinetic energy of the Marangoni flow per area on the surface of the droplet, m_s is the displaced mass (this mass is made of surface liquid of the Galinstan, liquid in its vicinity and delaminated skin oxide layer in Figs 3.3b and 3.4c), U_s is the skin tangential flow velocity generated by the Marangoni effect, A_s is the surface area of the moving layer, ρ_s is the density of the displaced mass, δ is the effective thickness of the displaced layer (Fig. 3.3b) at the interface of liquid metal (which also includes the surface oxide skin)

From the experimental results and measurements, Marangoni flow is constant over the surface and proportional to the potential difference as:

$$u \propto (\varphi - \varphi_{Th}) \rightarrow u = \alpha(\varphi - \varphi_{Th}) \quad (3.5)$$

in which φ is the applied potential, φ_{Th} is the threshold potential for each ionic liquid, at which Marangoni flow commences, and α is a constant number that is defined as the ionic liquid gradient of Marangoni flow graph against potential listed in Table 3.1.

The droplet resides in a circular recess. Therefore, the liquid metal at the interface with the recess has a zero velocity and surface Marangoni flow occurs predominantly on the surface of the top hemisphere of the droplet. Combining (3.4) and (3.5) result in:

$$E_{Unit\ Area} = \frac{1}{2} \delta \rho_s \alpha^2 (\varphi - \varphi_{Th})^2 \quad (3.6)$$

which is only valid for $\varphi > \varphi_{Th}$. Consequently, the surface tension changes, accordingly the Marangoni Flow effect can be approximated as:

$$\Delta \gamma_{Marangoni\ Flow} \cong -\frac{1}{2} \delta \rho_s \alpha^2 (\varphi - \varphi_{Th})^2 \quad (3.7)$$

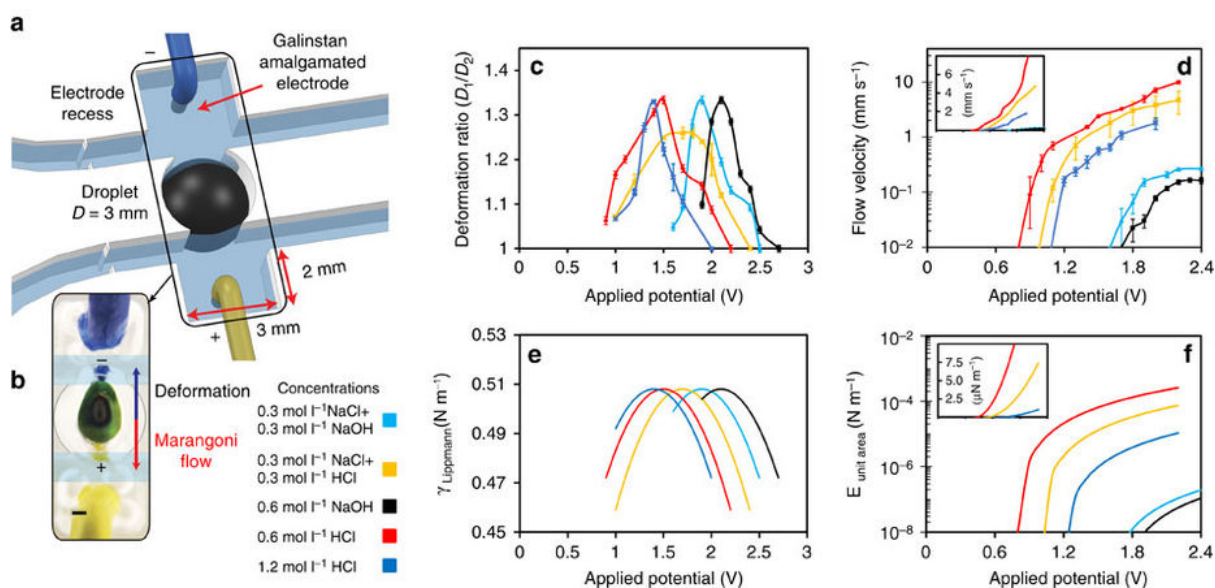


Figure 3.10. Characterization of droplet dynamics with an external applied electrical potential. (a) Electrodes are covered with Galinstan and placed in rectangular recesses (b) Marangoni flow and deformation direction of droplet created by the electrical potential. Scale bar is 0.5 cm . (c and d) Graphs of deformation ratios and Marangoni flow velocities under the applied electrical potential. Applied potentials that are greater than presented here cause the oxidation of the liquid metal. Error bars indicate s.e. ($N=6$). Calculated: (e) surface tension of the Galinstan droplet using Lippmann's equation (PZC value for EGaIn has been used in the simulation as the PZC of Galinstan¹²) and (f) the kinetic energies of Marangoni flows per unit area of a surface's cross section. Insets in d and f show graphs in linear scales.

3.3.10. Applications of liquid metal based on ionic imbalance self-propulsion

To demonstrate the self-propulsion of the liquid droplets due to pH and ionic concentration differences, selected regions based on Figs 3.3 and 3.7 were used to assess the effect of deformation and Marangoni flow on the behaviour of the droplets. A number of experiments were conducted. As a typical example, Fig. 3.11a presents images for the continuous motion of a self-propelling droplet in an open top semi cylindrical channel taken at different time intervals. The cylindrical shape of the

channel allowed the spherical droplet to completely separate the two electrolytes. The tube was coated with Teflon to reduce the friction force. The droplet was placed midway between the two reservoirs and the channels were filled as presented in Figure 3.10a shows the profile of the droplet velocity in a channel length of 8.7 cm. With the experimental conditions of 1.2 mol/L HCl and 0.6 mol/L NaOH, (which is later shown to be the optimum conditions for self-propulsion) the droplet travelled at a maximum velocity of 25 mm/s (Fig. 3.11b). Figure 3.12 show other experimental set points with velocities exceeding 20 mm/s. It is important to consider that after reaching the maximum velocity it almost drops linearly due to the height difference between the two reservoirs, which is generated after the displacement of the liquid, generating a pressure variance against the motion.

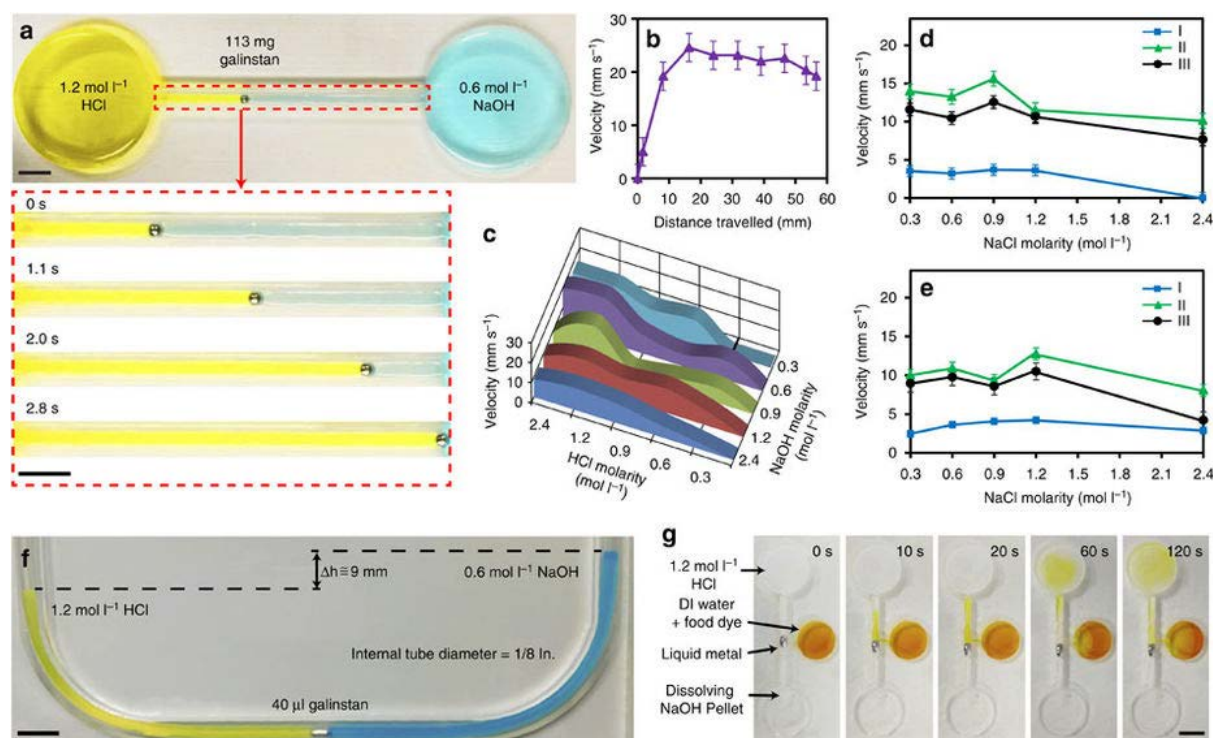


Figure 3.11. Liquid metal self-propulsion. (a) Droplet propels from 1.2 mol/L HCl to 0.6 mol/L NaOH reservoir. (b) The instantaneous droplet velocity profile of experiment a. Error bars indicate the s.e. (N=2). (c) Average velocity of droplets under different acidic and basic solutions. (d and e) Droplets velocities at different NaCl concentrations. Error bars indicate the s.e. (N=3). I, II, III in d indicate constant 0.6 mol/L NaOH (pH of ~13.8) and 0.6, 1.2 and 2.4 mol/L HCl (pH of 0.2, ~ -0.1

and ~ -0.4), respectively. I, II, III in e indicate constant 1.2 mol/L NaOH (pH of ~ 14.1) and 0.6, 1.2 and 2.4 mol/L HCl (pH of ~ 0.2 , ~ -0.1 and ~ -0.4), respectively. (f) Metal droplet pushes the liquid to produce a 6.5 mm difference in height. According to the ρgh (in which ρ is the density, g is the gravitation acceleration constant and h is the liquid height) this amount of liquid equates to a pressure exceeding ~ 1 mbar for 1/8 inch diameter tubing. By reducing the area, this headpressure can be significantly increased. (g) The concept of a switch based on the motion induced by the electrolyte difference on either side of the droplet. The pH difference across the liquid metal droplet induces a motion towards the basic liquid and opens the inlet to the liquid with DI water/yellow dye after 10 s. The liquid in the middle reservoir then mixes with the acidified liquid in the top reservoir. Snapshots taken at: 0, 10, 20, 60 and 120 s. Scale bars are 1 cm.

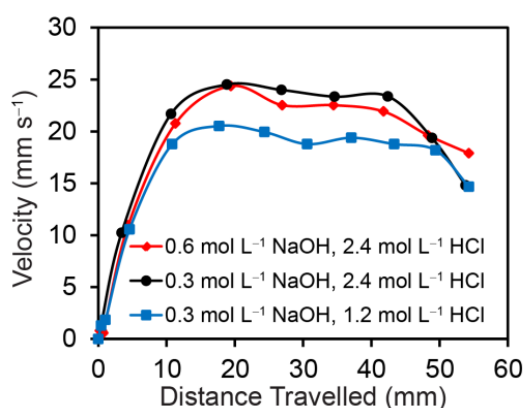


Figure 3.12. Self-propelling droplet with instantaneous velocity. Graph of three experimental velocity profiles with droplet velocities exceeding 20 mm s^{-1} .

A set of experiments with various pH differences and without any addition of NaCl were also undertaken. In general, the average velocity of the droplet increases with increasing the acid concentration (Fig. 3.11c) until reaching 1.2 mol/L HCl (pH of ~ -0.1) and then decreases. The peak velocity was generally associated with NaOH at a concentration of 0.6 mol/L (pH of ~ 13.8). The maximum velocity, as represented in Fig. 3.11b reached 25 mm/s.

Another set of experiments were conducted to assess the effect of the ionic concentration of NaCl on the droplet velocities. The NaCl concentrations were chosen based on the experiments presented in Fig. 3.7 and minima were seen in all graphs. At 1.2 mol/L NaOH, the minima occur at 0.9 mol/L NaCl concentration and for 0.6 mol/L NaOH it takes place at 0.6 mol/L NaCl. These NaCl concentrations are very consistent with the locations of the Marangoni flow peak positions as seen in Fig. 3.7. This reduction in velocity seems to be strongly associated with the effect of mixing of the electrolytes promoted by the Marangoni flow that deteriorates the EDL on each side and hence reduces the breakage of symmetry in the environment around the droplet. The maximum velocity belongs to the imbalanced condition of a mixed solution of 0.6 mol/L NaOH+0.9 mol/L NaCl on one side and 1.2 mol/L HCl on the other side. The droplet is capable of self-propelling longer distances as shown in Fig. 3.13 in a serpentine channel with a total length of 18.3 cm.

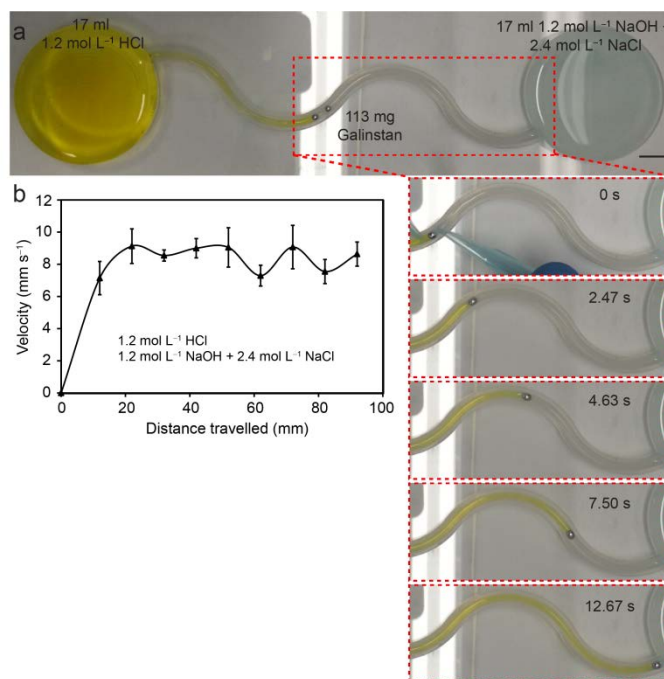


Figure 3.13. Channel Configuration to obtain high velocity profile of the self-propelling droplet. (a) Self-propelling droplet was tested in a longer serpentine channel. Configuration has total channel length of 18.3 cm and reservoir sizes of 5.5 cm. Experiment is conducted as explained in experimental methods. (b) Configuration is selected from region 2 of Fig. 3.3c to demonstrate the velocity profile in a region with measurable Marangoni flow and less deformation ratio. The droplet velocity profile shows a cyclic behaviour and descends regularly due to the mixing effect caused by the Marangoni flow.

As an example of practical applicability this pumping effect is tested (Fig. 3.11f). The liquid metal droplet is placed in a 1/8 inch diameter standard tubing and each side was filled with the acidic and basic electrolytes that gave the maximum velocity. As can be seen, the liquid droplet moved in less than 1 s generating a height difference of approximately ~9 mm which accounts for ~1 mbar pressure difference. This headspace pressure can be significantly increased by decreasing the surface area before entering the realm that atomic forces dominate the system.

Another example is the switching capability of the electrolyte only system (Fig. 3.11g), with the liquid metal droplet blocking access to the middle liquid reservoir. After electrolytes containing acid and base are introduced, the liquid droplet moves toward the basic area, opening the outlet of the middle reservoir. As a result, the middle liquid reservoir (containing DI water/yellow food dye) is gradually mixed with the content of the acid reservoir.

Electrical actuation of mercury has been shown by Kim *et al.*¹³ Similarly electrical actuations has been shown for liquid alloys of gallium by Tang *et al.*¹⁴ and Gough *et al.*¹⁵ Accordingly in comparison, the ionic imbalance can perform better, in terms of velocity, than electrical actuation for voltages less than 4 V when the deformation ratio is less than 1.5. However, significantly larger velocities can be obtained (up to five times larger than the ionic imbalance condition) using applied electrical potentials of 10 V or higher.

3.4. Surface tension measurement between galinstan and aqueous ionic electrolytes

Pendant drop shape analysis method is used for measuring interfacial tension between aqueous solutions and liquid metal droplet. The shape of the droplet is governed by the balance between gravitational and surface tension forces, from which the interfacial tension of droplet-liquid is obtained as:

$$\gamma = (\Delta \rho g D^2)/H \quad (3.8)$$

where $\Delta \rho$ is the difference in fluid densities, g is the gravitational acceleration, D is the equatorial diameter, and H is a shape dependent parameter, which is obtained using equation (3.9):¹⁶

$$\frac{1}{H} = \frac{B_4}{S^4} + B_3 S^3 - B_2 S^2 + B_1 S - B_0 \quad (3.9)$$

in which, “ $S=d/D$ ” is the shape factor with d defined as the diameter of droplet at the distance D from the bottom of the droplet. The values of A and B_i ($i=0, 1, 2, 3, 4$) are empirical constants, as given in Table 3.2¹⁶.

Table 3.2. Values of A and B_i for pendant drop shape analysis

Range of S	A	B_4	B_3	B_2	B_1	B_0
0.401-0.46	2.56651	0.32720	0	0.97553	0.84059	0.18069
0.46-0.59	2.59725	0.31968	0	0.46898	0.50059	0.13261
0.59-0.68	2.62435	0.31522	0	0.11714	0.15756	0.05285
0.68-0.90	2.64267	0.31345	0	0.09155	0.14701	0.05877
0.90-1.00	2.84636	0.30715	-0.69116	-1.08315	-0.18341	0.20970

3.5. Conclusion

According to the observations, the stored energy on the surface of a droplet, due to the ionic imbalance, can be converted into: (a) droplet propulsion kinetic energy for low concentration electrolytes in the deformation region, or (b) tangential skin flow for electrolytes of high concentrations in the Marangoni region. In reality, each component also involves an extra term representing the viscosity losses (propulsion viscosity loss for the deformation region and flow viscosity loss for the Marangoni region). By ignoring these viscosity loss components, the equation describing the system can be simplified into:

$$Kinetic\ energy \cong \begin{cases} \frac{1}{2} m_D U_D^2 & \text{Deformation region} \\ \frac{1}{2} \delta \rho_s A_s U_s^2 & \text{Marangoni region} \end{cases} \quad (3.10)$$

in which m_D is the droplet mass, U_D is the average propulsion velocity of the droplet due to the deformation effect, U_s is the skin tangential flow velocity due to the Marangoni flow, ρ_s is the density of the oxide skin layer moving tangentially along the surface of droplet, δ is the effective thickness of the skin layer (Figure 3.3b) and A_s is the average surface area of the skin layer. The kinetic energy of the liquid metal droplet, which is generated by the ionic imbalance, can be exploited according to equation (3.10).

pH and ionic concentration differences govern the components of equation (3.10) by determining the potentials and adsorbed surface charges. Exposure of the liquid metal droplet to a pH imbalance and ionic concentration differences induces a surface tension gradient across the droplet by (a) changing the PZC and (b) a generated potential. As demonstrated, in equation (3.10) the deformation component becomes dominant at relatively low pH values and low concentration differences. This is due to the fact that the self-limiting oxide surface in such conditions is atomically thin and the layer easily breaks down to allow the large deformation of the droplet (Fig. 3.3a and 3.14). Conversely, at relatively high pH and concentration differences, the Marangoni flow becomes the dominant component. This is the region in which the oxide becomes thick enough to reduce the deformation effect (Fig. 3.3b and 3.5).

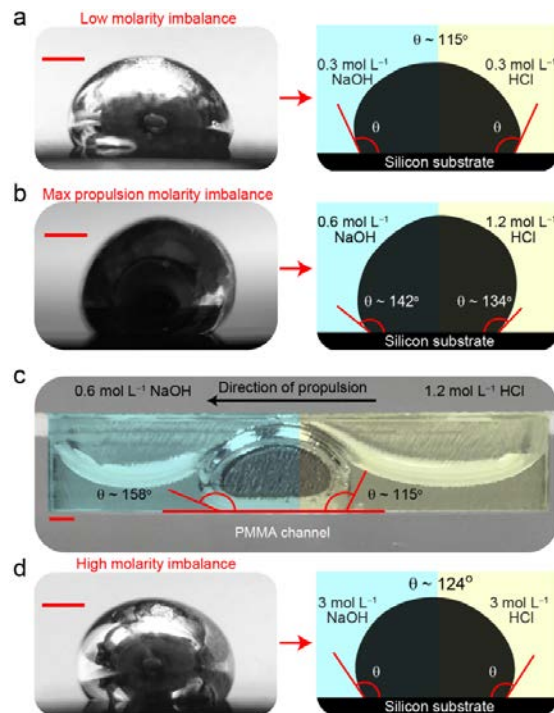


Figure 3.14. Droplet contact angle. (a) Droplet contact angle on a silicon substrate after the exposure to relatively low molarity imbalance, which results in soft and deformable skin. (b) Droplet contact angle after the exposure to molarities, which produce the maximum propulsion. (c) Droplet showing asymmetric contact angles when placed in ionic imbalance condition in b. (d) Droplet contact angle after the exposure to relatively high molarity imbalance which results in contact angles for producing less wettability and deformability than that of a. d represents an example of the Marangoni region.

The reader should consider equation (3.10) as valid under the conditions where there is no significant mixing of the electrolytes on the two sides of the droplet, due to the Marangoni flow. Obviously, in such an extreme regime, no symmetry breaking occurs and as such, no droplet motion takes place.

An interesting observation regarding the maximum velocity of the droplets is about the surface tension of Galinstan. The maximum velocity of the Galinstan droplet is obtained ($\sim 25 \text{ mm/s}$) for 0.6 mol/L NaOH (pH of ~ 13.8) and 1.2 mol/L of HCl (pH ~ -0.1) condition (Fig. 3.12). These two

numbers are associated with the local maximum of surface tensions for the area in contact with acidic and the local minimum of the surface tension for the area in contact with basic electrolytes that likely generate the maximum surface tension difference. This consequently generates the highest asymmetry across the liquid metal droplet, resulting in the maximum velocity. However, when the oxide becomes thick enough on both sides of the droplet, the deformation effect is reduced. As shown in Fig. 3.15, there still exists a significant surface tension gradient between the two sides of a droplet at high concentrations of acid and basic ionic electrolytes, despite the formation of this thick hydrated oxide layer. Surface tension measurement calculations are presented in section 3.4. Owing to the rigidity of the layers, this surface tension appears as Marangoni flow from NaOH towards HCl on the surface of the Galinstan. Parts of the skin layer are also delaminated and move with the tangential flow. This effect, however, is not seen for mercury droplets where an oxide layer is harder to form chemically (Fig. 3.6).

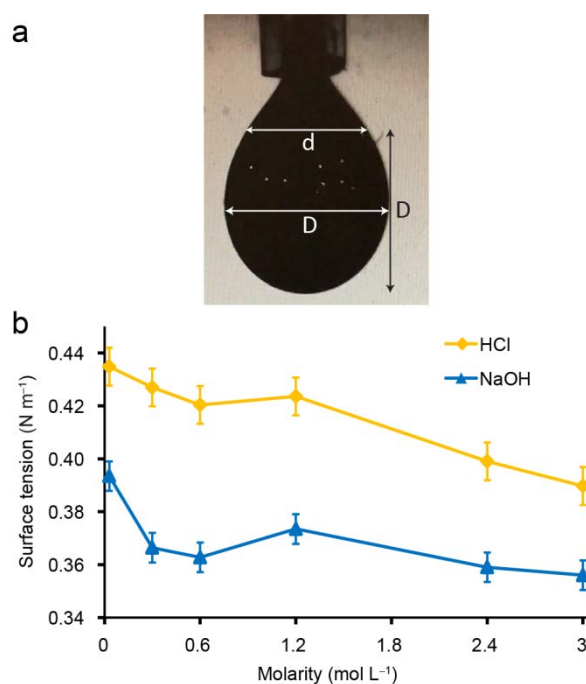


Figure 3.15. Surface tension measurement between Galinstan and aqueous ionic electrolytes. (a) Surface tension was measured using pendant drop method¹⁶. (b) Surface tension of Galinstan in contact with aqueous solutions of different HCl and NaOH concentrations. Error bars are s.e.m. (N=4).

In brief this chapter presented a comprehensive study of the autonomous motion of liquid metal droplets caused by modification of the liquid electrolyte surrounding the liquid metal. The maximum velocity is obtained at the largest magnitude of induced surface tension gradient according to Lippmann's equation. The ionic properties of the electrolytes contain sufficient energy to induce motion of the metal droplet through modification of the EDL. Consequently, the liquid metal droplet is continuously propelled without the need for an external electric potential. The measurements that showed some of the optimum conditions for gaining the maximum velocities of liquid metal droplets in an electrolyte only system is presented. To present some of the applications of this only electrolyte based liquid metal motion, the pumping capability of the system is demonstrated as well as a switching capability. The author's work fundamentally presents the governing factors in obtaining the best condition for self-propulsion that can also be extended to voltage induced motion systems. The outcomes of this work can be used for designing future autonomous low dimensional micromechanical units that are based on compositional changes of the employed electrolytes, thereby exploiting the use of systems that only contain liquid components.

References

1. Dickey, M. D., Emerging applications of liquid metals featuring surface oxides. *ACS Appl. Mater. Interfaces* **2014**, *6* (21), 18369-18379.
2. Tingyi, L.; Sen, P.; Kim, C. J., Characterization of nontoxic liquid-metal alloy galinstan for applications in microdevices. *J. Microelectromech. Syst.* **2012**, *21* (2), 443-450.
3. Zavabeti, A.; Daeneke, T.; Chrimes, A. F.; O'Mullane, A. P.; Zhen Ou, J.; Mitchell, A.; Khoshmanesh, K.; Kalantar-zadeh, K., Ionic imbalance induced self-propulsion of liquid metals. *Nat. Commun.* **2016**, *7*, 12402.
4. Scriven, L. E.; Sternling, C. V., The Marangoni effects. *Nature* **1960**, *187* (4733), 186-188.
5. Tang, S.-Y.; Khoshmanesh, K.; Sivan, V.; Petersen, P.; O'Mullane, A. P.; Abbott, D.; Mitchell, A.; Kalantar-zadeh, K., Liquid metal enabled pump. *Proc. Natl. Acad. Sci. USA* **2014**, *111* (9), 3304-3309.
6. Zhao, Y.; Yang, J.; Frost, R. L., Raman spectroscopy of the transition of α -gallium oxyhydroxide to β -gallium oxide nanorods. *J. Raman Spectrosc.* **2008**, *39* (10), 1327-1331.

7. Lyklema, J., Does electrical double layer formation lead to salt exclusion or to uptake? *Phys. Rev. E Stat. Nonlin. Soft Matter. Phys.* **2005**, *71* (3), 032501.
8. Davies, J. T., *Interfacial phenomena*. 2nd ed.; Academic Press: New York, 1963; p 108-153.
9. Grahame, D. C., The electrical double layer and the theory of electrocapillarity. *Chem. Rev.* **1947**, *41* (3), 441-501.
10. Grahame, D. C.; Coffin, E. M.; Cummings, J. I.; Poth, M. A., The potential of the electrocapillary maximum of mercury. II. *J. Am. Chem. Soc.* **1952**, *74* (5), 1207-1211.
11. Frumkin, A.; Polianovskaya, N.; Grigoryev, N.; Bagotskaya, I., Electrocapillary phenomena on gallium. *Electrochim. Acta* **1965**, *10* (8), 793-802.
12. Khan, M. R.; Eaker, C. B.; Bowden, E. F.; Dickey, M. D., Giant and switchable surface activity of liquid metal via surface oxidation. *Proc. Natl. Acad. Sci. USA* **2014**, *111* (39), 14047-14051.
13. Junghoon, L.; Kim, C. J., Surface-tension-driven microactuation based on continuous electrowetting. *J. Microelectromech. Syst.* **2000**, *9* (2), 171-180.
14. Tang, S. Y.; Sivan, V.; Khoshmanesh, K.; O'Mullane, A. P.; Tang, X.; Gol, B.; Eshtiaghi, N.; Lieder, F.; Petersen, P.; Mitchell, A.; Kalantar-zadeh, K., Electrochemically induced actuation of liquid metal marbles. *Nanoscale* **2013**, *5* (13), 5949-5957.
15. Gough, R. C.; Dang, J. H.; Moorefield, M. R.; Zhang, G. B.; Hihara, L. H.; Shiroma, W. A.; Ohta, A. T., Self-actuation of liquid metal via redox reaction. *ACS Appl. Mater. Interfaces* **2016**, *8* (1), 6-10.
16. J. Drelich, C. F., and C. L. White, *Measurement of interfacial tension in fluid/fluid systems*. Marcel Dekker Inc, New York, U.S.A.: New York, 2002.

Chapter 4

A liquid metal reaction environment for the room temperature synthesis of atomically thin metal oxides[†]

4.1. Introduction

In previous chapter, the surface manipulation of liquid metals at interface with the electrolyte surrounding it, was presented. In this chapter, the fundamental understanding of surface oxide composition of liquid metal at interface with air is investigated. Nontoxic eutectic gallium-based alloys are used as a reaction solvent and co-alloyed desired metals into the melt. On the basis of thermodynamic considerations, the composition of the self-limiting interfacial oxide is predicted. The surface oxide as a 2D layer is isolated, either on substrates or in suspension. This enabled to produce

[†] The contents of this chapter is published in Zavabeti et al., A liquid metal reaction environment for the room-temperature synthesis of atomically thin metal oxides, *Science*, 358, 332-335, 2017

extremely thin subnanometer layers of HfO_2 , Al_2O_3 , and Gd_2O_3 . The liquid metal-based reaction route can be used to create 2D materials that were previously inaccessible with pre-existing methods. The chapter introduces room-temperature liquid metals as a reaction environment for the synthesis of oxide nanomaterials with low dimensionality. The content of this chapter was published as an article in Science¹.

4.2. Experimental details

4.2.1. Eutectic gallium indium tin alloy (galinstan) preparation

I used a eutectic GaInSn alloy (galinstan) as a base liquid metal for all alloying and subsequent synthesis processes. This alloy features a melting point below 0 °C, which provides a large temperature margin when working with its co-alloyed materials at room temperature. Commercial galinstan frequently contains unknown additives (proprietary) which may interfere with its use as a reaction solvent. To ensure the exact composition, galinstan was made in-house by melting 68.5 wt% gallium, 21.5 wt% indium, and 10 wt% tin in a glass beaker, which was achieved by raising the temperature of the mixture to approximately 250 °C on a hot plate. The temperature was chosen since it is well above the melting point of tin (231.9 °C)². The melt was stirred with a glass rod after melting. The precursor materials (gallium 99.99%, indium 99.99% and tin 99.9%) were purchased from Roto Metals Inc. The materials were received in the form of large solid lumps (gallium), ingots (indium), and centimetre sized granules (tin). Macroscopic precursors were preferred over micron-sized powders due to the reduced presence of pre-existing surface oxides. After melting, the alloy was allowed to cool to room temperature. The pre-existing surface oxides could simply be removed by transferring the produced liquid metal from the reaction beaker into a storage container, using a plastic transfer pipette. Care was taken to only collect liquid metal from the centre of the melt, effectively decanting the pure liquid, leaving the grey surface layer behind. The final liquid metal exhibited the expected silver-metallic surface appearance and was stored in sealed vials inside a nitrogen glovebox until used.

General handling warning: Gallium based liquid metals are known to corrode metal surfaces. It is recommended that care is taken to avoid damage to equipment and instrumentation such as glove boxes, electron microscopes and photoemission spectrometers.

4.2.2. Co-alloying process

As explained above, galinstan was used as the base liquid metal and other elements were co-alloyed into it. This process is conducted inside a glove box with ~10 ppm oxygen to minimize oxidation of the material. The process involves adding 1 wt% micron sized metal powders to approximately 15 g of the liquid metal. A mortar and pestle were used to facilitate the alloying process, by breaking down the metal powders, increasing the surface area and breaking off pre-existing interfacial oxides. The manual grinding process was conducted rigorously for a period of 30 min. Successful alloying was found to be accomplished when the surface of the alloy became clear and shiny, indicating the absence of residual solid metal powders. Alloys and powders were stored inside the glove box. The following metal powders were purchased from Sigma-Aldrich Pty Ltd. (99.5% hafnium powder, 325 mesh; 99% gadolinium powder, 40 mesh; 99.5% copper powder, 150 mesh; $\geq 99.9\%$ silver powder, 5-8 μm and 99.5% aluminium powder, $< 5 \mu\text{m}$ particle size). After the synthesis, the mortar and pestle were washed with 1 mol/L of NaOH to remove bulk liquid metal residues. The mortar and pestle were then left in 98% H_2SO_4 for one hour to remove and dissolve any remaining oxide residue.

4.2.3. Van der Waals exfoliation synthesis

The room temperature liquid metal alloys were transferred onto a microscope glass slide using a plastic pipette. The microscopy slide was chosen as a work surface, since it is inert to the liquid metal alloys. The gallium based alloys were found to form round droplets on the glass surface due to their high surface tension. The diameter of the droplet was selected to be 2 mm or more, depending on the dimensions of the desired two-dimensional oxide sheets. The glass slide was tapped a few times to ensure that the surface of the droplet is flat. Before the start of each experiment and after several synthesis attempts, the surface of the droplet may feature thicker surface oxides due to initially present oxide layers (start of the experiment) or mechanical agitation (after several preceding exfoliations). In order to achieve reproducible results in the first and subsequent experiments, the

surface of the liquid metal was cleaned frequently by sweeping a thin glass rod (i.e. a Pasteur pipette) over the surface of the liquid metal, removing the oxide skin.

As shown in Figure 4.1, exfoliation was achieved by touching the surface of the liquid metal with the desired substrate. When contact is made with excessive force, liquid metal may delaminate from the droplet and attach to the substrate. This occurs particularly easily for substrates that are oxygen terminated (e.g. SiO_2). To avoid this issue, smaller sized droplets and less force to minimize delamination of liquid metal for these substrates are used.

Highly reactive elements such as aluminium and gadolinium oxidise very rapidly on the surface of the droplet. Therefore, the exfoliation is performed for these elements in an oxygen reduced environment containing less than 0.1% of oxygen, allowing extended experimental times and more controlled conditions. The oxygen controlled environment was achieved by working within a bench-top Perspex glove box, which was purged with nitrogen and equipped with an oxygen sensor (lower detection limit 0.1%).

I successfully exfoliated oxide sheets from liquid metal droplets being up to 1 cm in size. Larger metal droplets were found to be challenging to work with, since the contact force is difficult to control manually. Automation of the exfoliation process will likely overcome this limitation and ensure scalability.

Various substrates were used as target surfaces including Si, SiO_2 , Pt coated Si wafers, Au coated Si wafers, quartz, glass, ITO and TEM grids (several not shown). All samples were visually inspected using a standard optical microscope. Any samples that featured visible metal inclusions were discarded. Prepared samples were found to be stable under ambient conditions for at least several days.

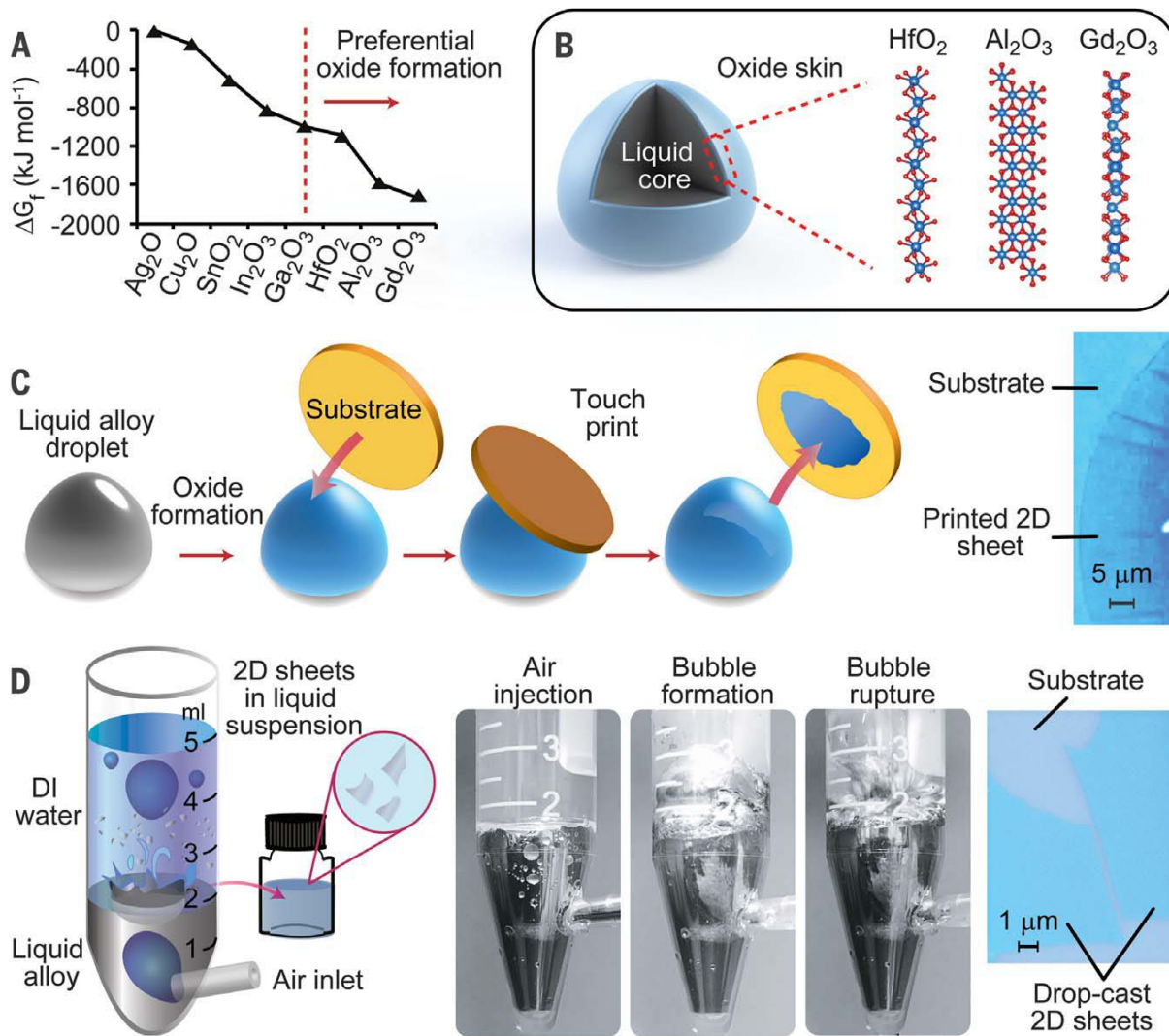


Figure 4.1. Fundamental principles and synthetic approach. (A) Gibbs free energy of formation for selected metal oxides (5, 6). Oxides to the right of the red dashed line are expected to dominate the interface. (B) A cross-sectional diagram of a liquid metal droplet, with possible crystal structures of thin layers of HfO₂, Al₂O₃, and Gd₂O₃ as indicated. (C) Schematic representation of the van der Waals exfoliation technique. The pristine liquid metal droplet is first exposed to an oxygen-containing environment. Touching the liquid metal with a suitable substrate allows transfer of the interfacial oxide layer. An optical image is shown at the right. (D) Schematic representation of the gas injection method (left), photographs of the bubble bursting through the liquid metal (centre), and an optical image of the resulting sheets drop-cast onto a SiO₂/Si wafer (right).

4.2.4. Gas injection synthesis

As shown in Figure 4.1, for this synthesis method, a plastic centrifuge tube from Sigma-Aldrich Pty Ltd was used as the reaction vessel. A 1/8 inch hole was drilled into the side of the centrifuge tube. A PFA (Perfluoroalkoxy) tube with similar outer diameter and an inside diameter of 1/16 inch was connected into the centrifuge tube. Approximately 2 ml of the liquid metal alloy were placed inside the centrifuge tube and 3 ml of solvent (here distilled water) were placed on top of the liquid metal. It is observed that the liquid metal column should be at least 1-2 cm in height above the gas inlet tube, in order to minimize the formation of semi-permanent micro-channels which can compromise the bubble formation process. A mass flow controller (MKS 1479) was utilized to control the flow of compressed, dry laboratory air through the pipe into the liquid metal with a flow rate of 30 sccm. It is observed that placing the gas inlet hole at the bottom of the centrifuge tube may result in leakage of liquid metal into the gas inlet tube. Therefore, the inlet was placed on the side of the centrifuge tube.

The possible duration of the synthesis depends on the amount of alloyed metal that is present. The synthesis of Ga_2O_3 when using galinstan could in theory be continued for several hours with negligible decay in gallium wt% due to the abundance of this element (~68.5 wt%) in the melt. However, the added 1 wt% of metallic hafnium was found to be consumed within approximately 30 min. As such, a reaction time of 30 min was selected. Once the majority of elemental hafnium is consumed, gallium oxide begins to form. In order to avoid the presence of Ga_2O_3 , a hydrochloric acid wash was added, this wash is capable of dissolving any produced gallium oxide nanosheets³. This was achieved by adding 0.2 mol/L of HCl to the aqueous solution after the synthesis. The samples prepared by the gas injection synthesis method were centrifuged for 1 hr at 50 RCF at room temperature in order to remove any residual liquid metal droplets.

Prepared samples were found to be stable in aqueous solution for several days. After prolonged storage (weeks) and in the absence of capping agents and surfactants, agglomeration of the nanosheets suspended in DI water was observed. Samples drop-cast onto a substrate were found to be stable under ambient conditions for at least several days.

4.2.5. Instrumentation and characterization

Raman spectroscopy was conducted with a Horiba Scientific LabRAM HR evolution Raman spectrometer equipped with a 100× objective lens, a 532 nm laser source (intensity 0.45 mW at the sample position) and a 1800 lines per mm grating. Two accumulations with a duration of 60 s each were utilized. The samples were deposited on either gold coated Si wafers (Ga_2O_3) or on Si wafers (HfO_2). Surface topography and Peak Force TUNA (PF-TUNA) measurements were conducted using a Bruker Dimension Icon AFM. The instrument features a noise floor of less than 30 pm enabling imaging at sub-nanometer resolution. The AFM was equipped with ScanAsyst® Imaging and NanoScope® software 1.8. Scanasyst air and SCM-PIT-V2 AFM tips were used for topography imaging and the PF-TUNA mode, respectively. Topographic images were obtained using samples deposited on Si/SiO₂ wafers using either the exfoliation method or drop-casting of the samples obtained with the gas injection method. PF-TUNA measurements are detailed below and the fitting of the data is described in the Schottky emission model section of this document. For PF-TUNA measurements, the sample was prepared applying the exfoliation method using a platinum coated Si/SiO₂ wafer as a substrate. The platinum was deposited using electron beam evaporation leading to a layer thickness of 200 nm. The platinum substrate was electrically connected to a stainless-steel disk with silver paint (as shown in Figure 4.8). The silver paint was allowed to dry for 12 hours. The stainless steel disk was then placed on the AFM stage through which an external bias voltage could be applied. Bruker SCM-PIT-V2 platinum/iridium coated AFM tips with radii of 25 nm were used. The tip work function has been measured to be 4.86 eV⁴. Topography images of the sheets were measured using a normal imaging tip (ScanAsyst air) in order to conserve both the sample and the conductive tip prior to high resolution imaging and I-V curve measurements. During current imaging and I-V characterization, a bias voltage was applied to the sample and the electrical current was measured. Positive voltage ranges were applied to the platinum and consequently the tip was negatively biased. Under these conditions the effects of the formation of a depletion region in the SiO₂ substrate could be avoided⁵. The current was limited by the selected sensitivity range. Therefore, all current measurements have been capped at 250 pA. All measurements using PF-TUNA were carried out in PF-TUNA mode. The conductive map of the 2D HfO₂ sheet shown in Figure 4.8B was collected

using a 4 mV sample bias. X-ray photoelectron spectrometer (XPS) was performed using a Thermo Scientific K-alpha spectrometer. The instrument uses an Al k- α monochromated X-ray source providing photons with an energy of 1486.7 eV, with a spot size of approximately 400 μm . A pass energy of 100 eV was selected in conjunction with a dwell time of 50 ms. Typical measurements were averaged for more than 70 scans in the specified energy ranges. Avantage software was used for data acquisition and analysis. High resolution transmission electron microscopy (HR-TEM): two HR-TEM instruments were used. For TEM image processing, both ImageJ 1.50i and Gatan microscopy suite 1.8.4 were used. For EELS analysis, Gatan microscopy suite 1.8.4 was used. The samples were prepared by directly depositing the oxide layers onto TEM grids using the exfoliation method. The samples prepared using the gas injection method were drop-cast onto the TEM grids. A JEOL 2100F TEM/STEM (2011) operating with an 80 keV acceleration voltage was used for most of the imaging. The instrument was equipped with a Gatan Tridium Imaging Filter (EELS Spectrometer) and Gatan Orius SC1000 CCD Camera. The electron source beam energy featured a resolution of ~ 1 eV. It was observed that some of the 2D materials appeared to be beam sensitive. As such, care was taken to avoid beam damage, and most of the work was conducted using this instrument due to the lower acceleration voltage. A JEOL 2010 TEM (1990) with a 200 keV acceleration voltage was used for additional imaging. This instrument was equipped with a Gatan Orius SC600 CCD Camera (2011). A FEI Quanta 200 environmental scanning electron microscope ESEM (2002) equipped with an Oxford X-MaxN 20 energy dispersive X-ray spectroscopy (EDXS) Detector (2014) was used for the EDXS analysis of the alloyed metals. EDXS analysis was conducted using a high acceleration voltage of 30 kV in order to ensure a high emission depth of the X-rays. Elemental maps of the alloys were prepared using Oxford instrument Aztec software.

4.2.6. Fitting of I-V data: The Schottky emission model

Current voltage curves (I-V) were obtained during AFM based PF TUNA characterization. The observed I-V characteristics follow the Schottky emission model.⁶ The experimental approach for obtaining the I-V curves is detailed above. In this section, describe the fitted method. The Schottky emission model for dielectric films can be described as:⁷⁻⁸

$$J = \frac{4\pi q K^2 m^*}{h^3} T^2 e^{\frac{-q(\phi_B - \sqrt{qE/4\pi\epsilon_r\epsilon_0})}{kT}} \quad (4.1)$$

In which, J is the current density, q is the elementary charge of an electron, K is Boltzmann's constant, m^* is the effective electron mass in the dielectric, h is the Planck's constant, T is the temperature in Kelvin, ϕ_B is the Schottky barrier height, E is the electric field, ϵ_0 is vacuum permittivity and ϵ_r is the relative dielectric constant. The current density can be derived as follows:

$$J = \frac{I}{A^*} \quad (4.2)$$

In which, I is the current and A^* is the effective area between AFM tip and HfO₂. Equation 4.1 is rewritten as seen below:

$$I = A^* \frac{4\pi q K^2 m^*}{h^3} T^2 e^{\frac{-q(\phi_B - \sqrt{qE/4\pi\epsilon_r\epsilon_0})}{kT}} \quad (4.3)$$

To estimate dielectric constant, equation is further simplified the equation. Without any assumption for the values of the effective AFM tip contact area and effective mass of electron:

$$I = \alpha e^{\frac{-q(\phi_B - \sqrt{qE/4\pi\epsilon_r\epsilon_0})}{kT}} \quad (4.4)$$

Where α is defined as follows:

$$\alpha = A^* \frac{4\pi q K^2 m^*}{h^3} T^2 \quad (4.5)$$

The logarithm of equation 4.4 gives:

$$\ln(I) = \ln(\alpha) + \frac{-q(\phi_B - \sqrt{qE/4\pi\epsilon_r\epsilon_0})}{kT} \quad (4.6)$$

The electric field across the dielectric film is defined as below:

$$E = \frac{V}{d} \quad (4.7)$$

Where V is the applied voltage and d is the dielectric thickness. The film thickness has been measured to be 0.65nm using AFM. This thickness corresponds well to the dimensions of the HfO₂ unit cell (0.53 nm in the c-direction) which was used in the model. Figure 4.9 shows the I-V curve of the conductive tip directly placed on the platinum substrate (without the HfO₂ layer), which indicates that the resistance of the experimental setup is negligible and that the measured I-V characteristics are entirely associated with the 2D nanosheet that has been placed on top of the Pt substrate. The I-V curve shown in figure 4.8C allows to estimate ϕ_B which is approximately ~3.28V. The barrier height is reduced to 2.65V when the work function difference between the tip and substrate are considered. Fits assuming both barrier heights (with and without work function correction) resulted in similar estimates for the dielectric constant. Fitting of the experimental data to equation⁹ was conducted using the non-linear least square equation solver in Matlab's optimisation toolbox. The resultant fit results in an estimate of the relative dielectric constant of 38.87 with an R2 of 0.94. The fit is shown in the subset of the Figure 4.8C in the main text.

4.2.7. Band Gap determination using electron energy loss spectroscopy (EELS)

Details of the instrumentation utilised for EELS analysis have been described above. In this section the data interpretation and analysis processes used in determining the size and nature of the bandgap is described. The low loss section of EELS spectra features the zero-loss peak which is attributed to the probe beam. For wide bandgap semiconductors and dielectrics, the zero loss peak is followed by a flat region (~zero intensity) which is again followed by a sharp rise in intensity at the material's band gap energy. As a result, low loss EELS analysis can be utilised to measure the bandgap of materials.¹⁰ The technique is particularly suitable for the characterization of high band gap material due to larger separation of zero loss peak and E_g. As such this technique is frequently used for the characterization

of HfO₂, particularly since other methods such as UV-vis analysis are challenging at such high energies. Analysis of the EELS spectrum shown in Figure 4.8 D results in an estimated bandgap of E_g=6eV. EELS analysis provides further insight into the nature of the band gap, and it can be determined whether the transition is direct or indirect. EELS intensity can be described using the below equations:¹⁰

$$Intensity \propto (E - E_g)^{1/2} \quad (4.8)$$

$$Intensity_{Total} - Intensity_{Background} = (E - E_g)^{1/2} \quad (4.9)$$

Here, *Intensity* is the EELS spectra intensity, E is the energy loss and E_g is band gap.

The non-linear least square equation solver in Matlab's optimisation toolbox is used to fit the measured data to equation (4.9). An excellent fit is observed with R² = 0.98%. The fit is shown in subset of Figure 4.8D. This strongly indicates band gap measured at 6eV is a direct band gap.

4.3. Results and Discussions

Three different 2D oxides are synthesised using galinstan as a reaction environment. To show the versatility of the method, oxides of a transition metal (HfO₂), a post-transition metal (Al₂O₃), and a rare earth metal (Gd₂O₃) with high melting points are selected. Of these oxides, hafnium oxide is particularly important because of its use as an insulating oxide in the electronics industry. For galinstan, gallium oxide is expected to form on the metal surface because it features the most negative ΔG_f of the possible oxides²⁻³. Amount of ~1 wt % of elemental hafnium, aluminium, or gadolinium into the liquid metal is alloyed, which served as the precursors for the formation of their respective oxides (Fig. 4.2)¹¹. These oxides fulfilled the requirement of featuring a lower ΔG_f than gallium oxide, and as a result they expected them to form surface oxides on their respective alloys (Fig. 4.1, A and B)². All three oxides that are synthesised as 2D materials have nonstratified crystal structures and cannot be obtained using standard exfoliation techniques¹¹⁻¹². Nonetheless, either the investigated

oxides or closely related structures have been predicted to be stable as 2D monolayers¹³⁻¹⁵. Alloys containing ~1 wt % copper and silver for control experiments are prepared.

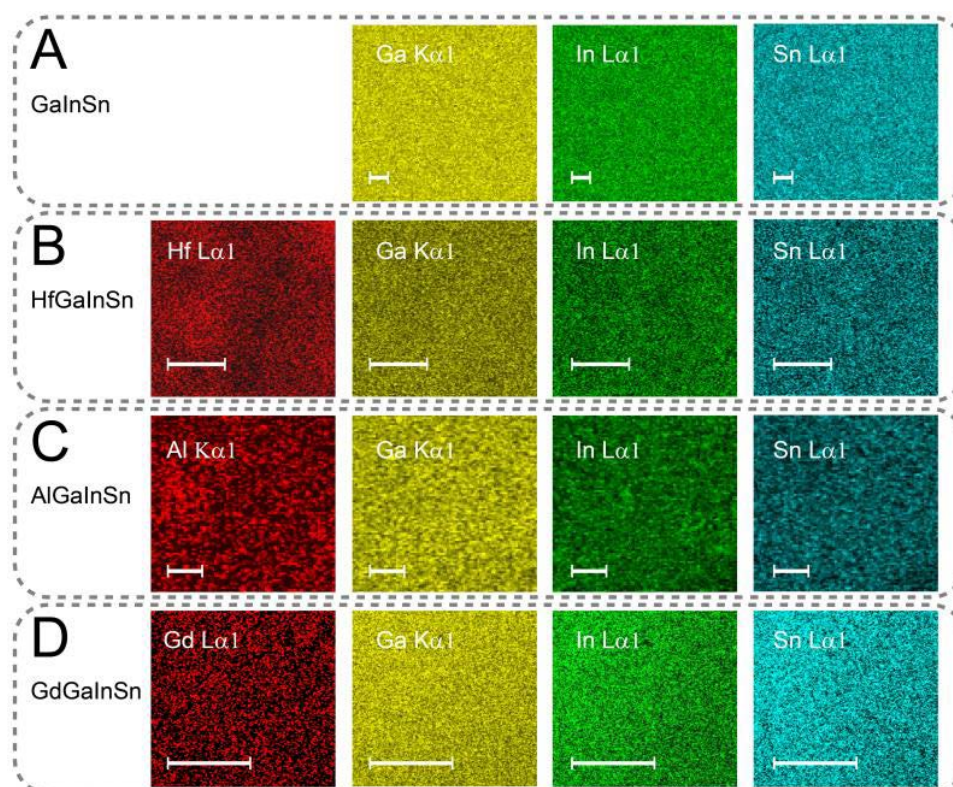


Figure 4.2. Characterization of the dispersion of co-alloyed elements in the liquid metal using EDXS. Colour maps were used to confirm the successful dispersion of the added elements within galinstan. The scale bars are 2 μ m. Since all precursor metals were purchased as micron sized powders (sizes between 5 and ~500 μ m, depending on the metal), successful amalgamation is observed. No micron sized inclusions of the added metal were observed throughout EDXS characterization. The EDXS data were utilised to determine the overall concentration of the added metal within the melt which was ~1% in all cases as expected.

I developed two synthesis approaches for the isolation of the surface oxide. The first method was a van der Waals (vdW) exfoliation technique similar to the method for obtaining monolayer graphene pioneered by Novoselov et al. (Fig. 4.1C) ¹⁶. The technique entails touching the liquid metal droplet with a solid substrate. The liquid nature of the parent metal results in the absence of macroscopic forces between the metal and its oxide skin, allowing clean delamination ¹⁷. This technique is suitable for the production of high-quality thin oxide sheets on substrates. The second technique relies on the injection of pressurised air into the liquid metal (Fig. 4.1D) (Gas injection synthesis method is explained in Experimental details section). The metal oxide is expected to form rapidly on the inside of air bubbles as they rose through the liquid metal. The released air bubbles passed through a layer of deionised water that is placed above the liquid metal, allowing the produced oxide sheets to be dispersed into an aqueous suspension. This technique is highly scalable and is therefore suitable for creating high-yield suspensions of the target oxide nanosheets.

To directly compare the different oxide nanosheets, the exfoliation method is used on all the alloys which are investigated. The optical images show the large lateral dimensions of the products (Fig. 4.1, C and D). To further characterize the nanosheets, atomic force microscopy (AFM) is performed on samples deposited on top of SiO₂/Si wafers and transmission electron microscopy (TEM) on samples directly deposited onto TEM grids (Fig. 4.3). Materials produced by the exfoliation method featured a smooth appearance under AFM imaging. Each 2D oxide sheet which are produced has a different thickness: 2.8 nm for gallium oxide, 0.6 nm for hafnium oxide, 1.1 nm for aluminum oxide, and 0.5 nm for gadolinium oxide. The ultrathin nature of the oxides is apparent from the translucent appearance and occasional wrinkles in the TEM images (Fig. 4.3).

I found that the nanosheets derived from unalloyed galinstan were amorphous when characterised by electron diffraction and high-resolution TEM (HRTEM). By contrast, the 2D oxides produced from alloys containing hafnium, aluminium, and gadolinium were polycrystalline, with characteristic lattice parameters of m-HfO₂, α -Al₂O₃, and cubic Gd₂O₃ (Fig. 4.3) ¹⁸⁻²⁰. Using x-ray photoemission spectroscopy (XPS), It is found that the exfoliated oxide of unalloyed galinstan is exclusively composed of gallium oxides (mostly Ga₂O₃ with a small Ga₂O content) ^{3, 21}. The 2D materials derived

from the alloys were composed entirely of the oxide of the added element (Figs 4.3 and 4.4). The control experiments with copper and silver alloys resulted in nanosheets predominantly composed of gallium oxide (Fig. 4.5). The results confirm the hypothesis that the oxide with the lowest ΔG_f dominates the interfacial surface oxide.

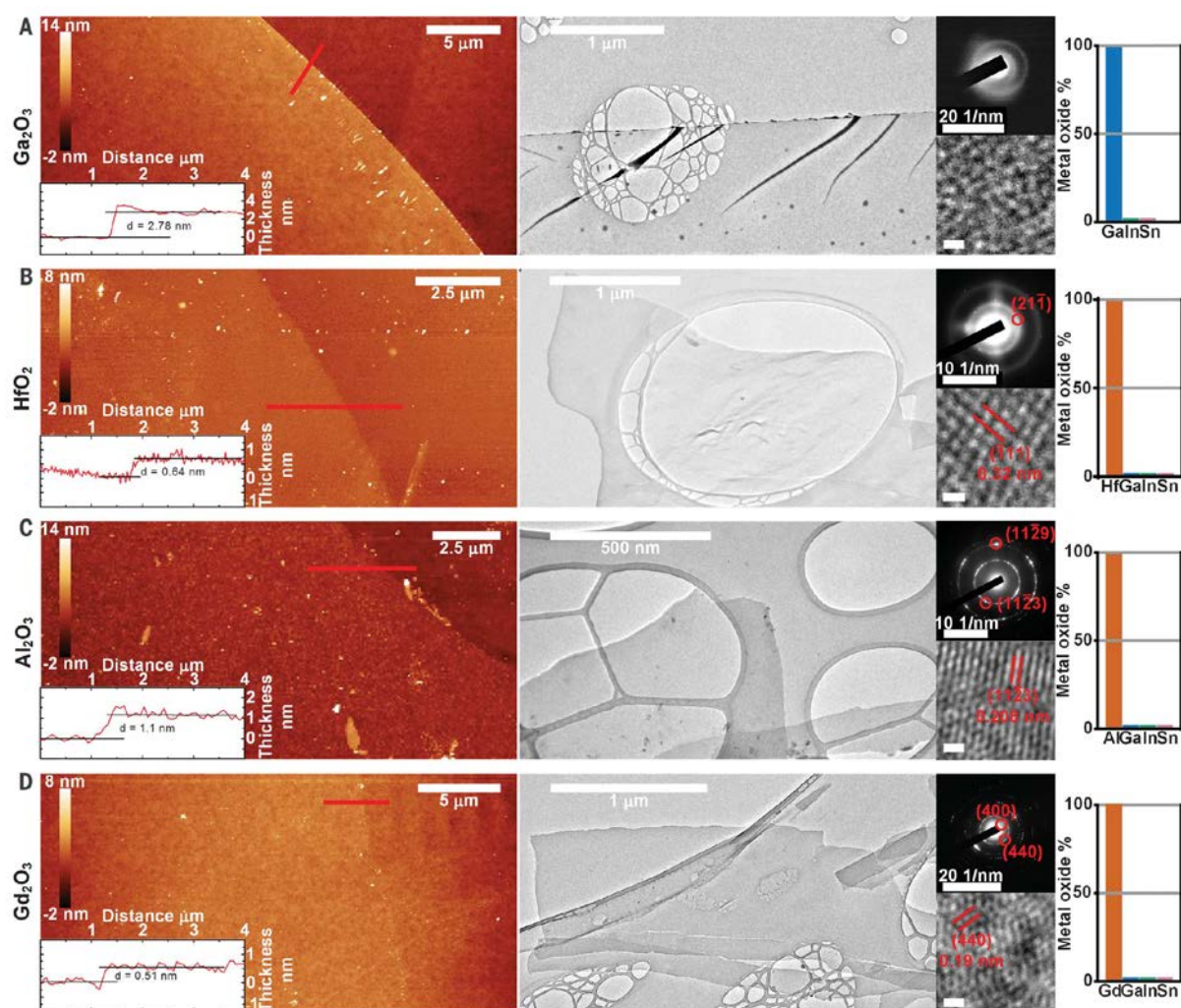


Figure 4.3. Characterization of materials derived from the exfoliation method. Left: AFM images, with thickness profile (inset) determined at the red line as indicated. Centre: TEM characterization, with selected-area electron diffraction (SAED) (top inset) and HRTEM images (bottom inset; scale bar, 0.5 nm). Right: Elemental composition determined by XPS²²⁻²⁷. (A) Results obtained from a eutectic gallium-indium-tin alloy. (B to D) Alloys containing approximately 1% of

added hafnium, aluminium, and gadolinium, respectively. See Fig. 4.2 for characterization of the alloys before use. The lattice parameters in SAED and HRTEM images were indexed using literature reports¹⁸⁻²⁰. The lack of crystallinity in the gallium oxide sample might be beam-induced. See Fig. 4.4 for XPS spectra used to determine the oxide composition. The sample derived from pure galinstan features metallic inclusions, which are visible as dark dots and elongated nodules. The other materials feature no inclusions. The lateral dimensions of the 2D sheets are extraordinarily large and exceed the AFM field of view.

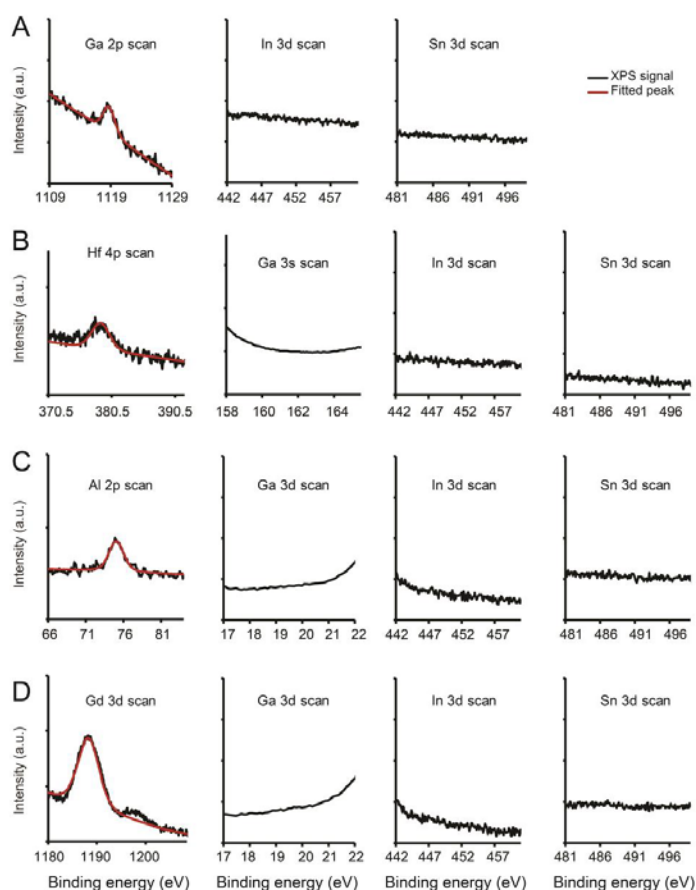


Figure 4.4. XPS spectra of the exfoliated sheets as shown in Figure 4.3. The XPS results indicate that the oxides exfoliated from the surface of the liquid metal consist of single element oxides. Other elements that were present in the precursor alloy have no measurable signals. Peak positions and binding energy ranges were auto selected by the Avantage software. Due to the thin nature of the oxide layers, signals from the substrates may mask the sample signal. Therefore, different binding energy ranges were selected featuring high sensitivity factors and no overlap between possibly present elements. According to the Avantage database, Ga⁰ peaks are located at 18.7 eV (Ga3d), 159.5 eV (Ga3s) and 1117 eV (Ga2p) eV. In⁰ and Sn⁰ have peaks at 444 eV (In3d) and 484.8 eV (Sn3d), respectively. Hf⁰, Al⁰ and Gd⁰ have peaks at 382 eV (Hf4p), 72.9 eV (Al2p) and 1186 eV (Gd3d), respectively. The corresponding peaks of the oxides are expected to appear at slightly higher binding energies²²⁻²⁷. The absence of peaks in the regions associated with possibly present side products leads to the conclusion that the produced nanosheets are pure within the resolution of the measurement. The small peak in the Gd3d region next to the Gd₂O₃ peak is a satellite feature. The results are summarised in Figure 4.3.

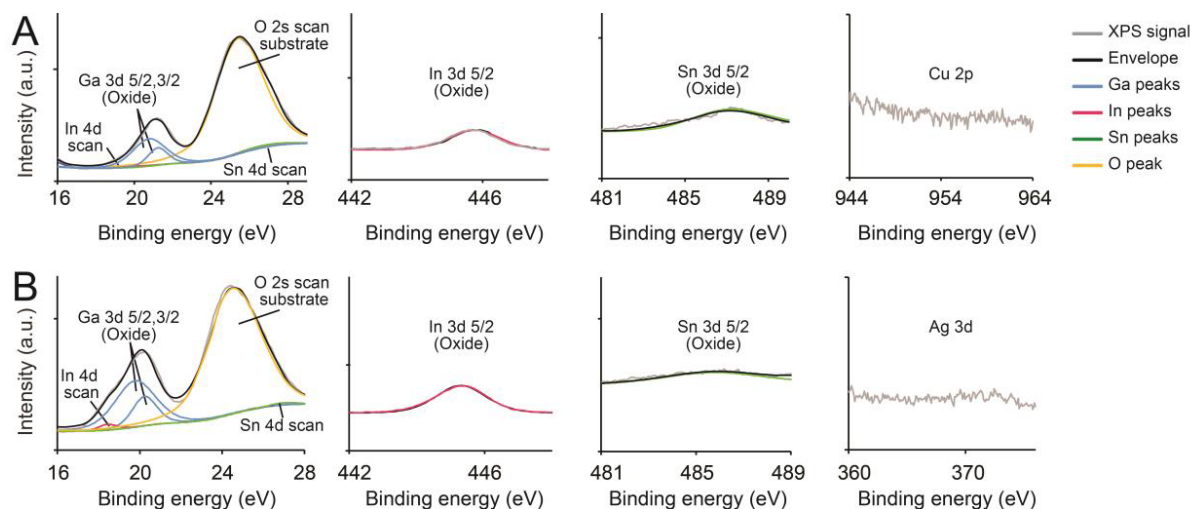


Figure 4.5. XPS results for the control experiment on liquid metal alloys containing added Ag and Cu. The exfoliation synthesis was utilised in order to exfoliate the surface oxide onto SiO_2 substrate. The XPS results confirm the absence of Cu (A) and Ag (B) oxides.

Galinstan and hafnium-containing galinstan were investigated using the gas injection synthesis method. The aluminium- and gadolinium-containing alloys visibly reacted with water and were not investigated further. Replacing water with an inert solvent was expected to enable the synthesis of aluminium and gadolinium oxide with this gas injection method. The materials that are derived from the gas injection synthesis method were similar in appearance to the oxides produced with the exfoliation method (Fig. 4.6). The material synthesised using unalloyed galinstan had a thickness of ~ 5.2 nm, about double that of the exfoliation method. It is found that the HfO_2 nanosheets had a thickness of 0.5 nm, which is similar to the thickness of exfoliated HfO_2 . The gallium oxide nanosheets contained small, spherical metallic inclusions that are discovered during TEM imaging. The presence of ~ 15 -nm spherical inclusions is confirmed with high-resolution AFM and TEM imaging (Fig. 4.7). The nanosheets have low crystallinity, which are examined using HRTEM and electron diffraction measurements. This indicates that the gas injection synthesis may have a tendency to create amorphous oxides. The short reaction time, attributable to a limited residence time for the

gas bubble within the liquid metal, may be the origin of the poor crystallinity. The reaction time frame available for the exfoliation method is considerably longer, because the metal droplet may rest for several minutes prior to the vdW transfer, allowing for the reorganisation of the crystal structure within the interfacial oxide layer.

Using Raman spectroscopy, it is found that the nanosheets derived from the gas injection method are also predominantly composed of the oxide with the lowest ΔG_f (Fig. 4.6). The successful gas injection synthesis of both gallium and hafnium oxides demonstrates the suitability of the approach for the high-throughput synthesis of 2D oxides for applications where high crystallinity is not a primary concern. The 2D materials which are synthesised hold promise for applications in energy storage, such as supercapacitors and batteries that require large quantities of materials with high ratios of surface area to volume²⁸.

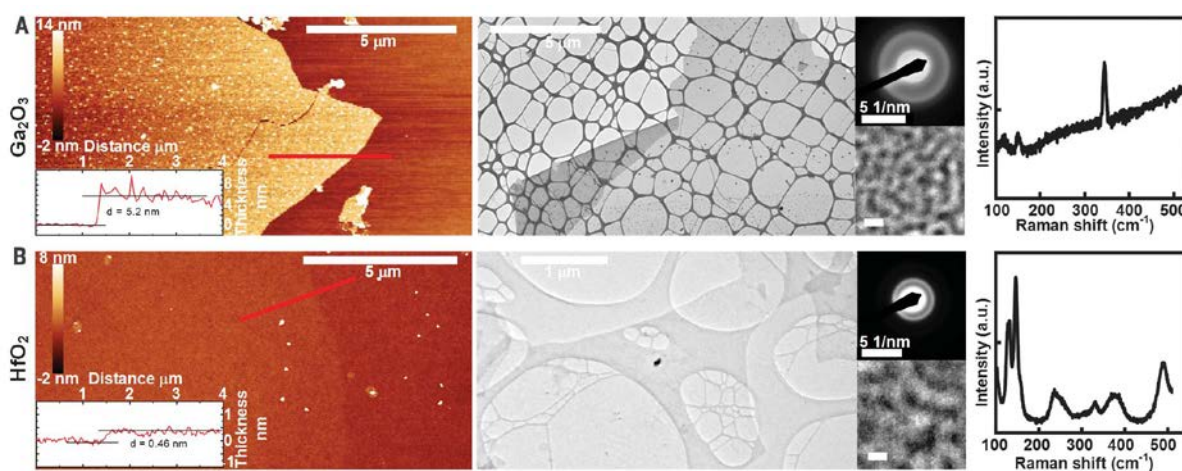


Figure 4.6. Characterization of materials derived from the gas injection method. Left: AFM images, with thickness profile (inset) determined at the red line as indicated. Centre: TEM characterization, with SAED (top inset) and HRTEM images (bottom inset; scale bar, 0.5 nm). Right: Raman spectra of the resulting oxides. (A) Results obtained from a eutectic gallium-indium-tin alloy. (B) Alloy containing approximately 1% of added hafnium. The Raman spectra match well with literature reports for Ga_2O_3 (A) and HfO_2 (B)¹⁸.

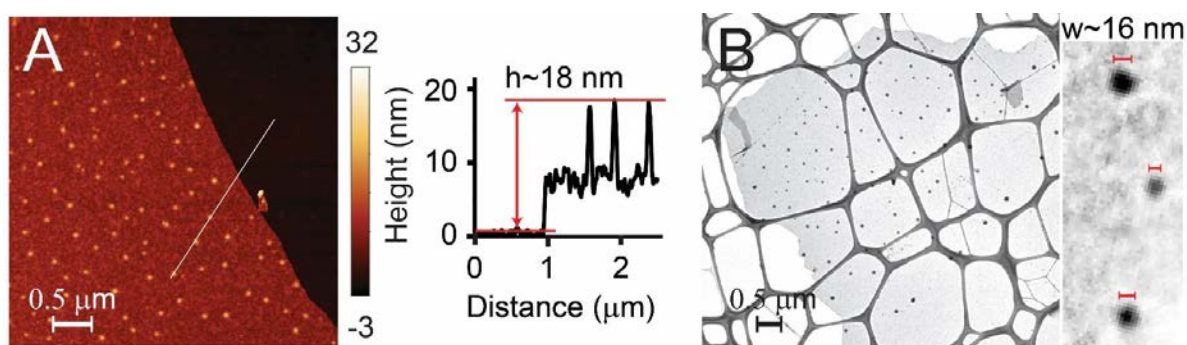


Figure 4.7. Gas injection synthesis of Ga_2O_3 results in metal inclusions. The inclusions are well separated and spread throughout the nanosheets. (A) and (B) show AFM and TEM images of these inclusions. The AFM height profile in (A) reveals that the height of these nano-sized inclusions is $\sim 10\text{--}15$ nm once the thickness of the oxide sheet is considered. TEM imaging (B) confirms that the width of these inclusions is roughly 16 nm.

One major application of the materials which are developed is their use as ultrathin insulator dielectrics for the fabrication of field-effect transistors. HfO_2 is the material of choice for the electronics industry, with a relative dielectric constant of >20 and a band gap of >5 eV²⁹. Because of the lack of a stratified crystal structure and the resulting absence of amenable exfoliation techniques, HfO_2 -based dielectrics are traditionally deposited using atomic layer deposition or other chemical and physical vapour-phase deposition techniques²⁹. These techniques rely on an island-mediated film growth mechanism that results in a minimum film thickness of 3 to 5 nm³⁰. The liquid metal-derived HfO_2 had a minimum thickness of approximately 0.5 nm. The 2D HfO_2 are directly deposited onto a wafer coated with Pt to evaluate the exfoliation methodology for the synthesis of dielectrics. Using conductive AFM characterization, it is found that the deposited 2D HfO_2 sheet is completely insulating and pinhole-free, despite being only ~ 0.5 to 0.6 nm thick (Fig. 4.8, A and B). The breakdown electric field, defined as the field at which the current rises above the noise level, is ~ 5.3 GV cm^{-1} , as determined by current-voltage (I-V) characterization of the 2D nanosheet. This value is three orders of magnitude higher than the breakthrough field for chemical vapour deposition (CVD)-

grown multilayer h-BN³¹⁻³², highlighting the excellent quality of the dielectric. Fitting the I-V curve to the Schottky emission model allowed to determine a dielectric constant of ~ 39 for the oxide sheets (see section 4.2.6). The low-loss region of the electron energy loss spectrum (EELS) of exfoliated ultrathin HfO₂ sheets is analysed and found that the band gap of the material is of a direct nature with a ~ 6 -eV gap (Fig. 4.8D)³³ (see section 4.2.7).

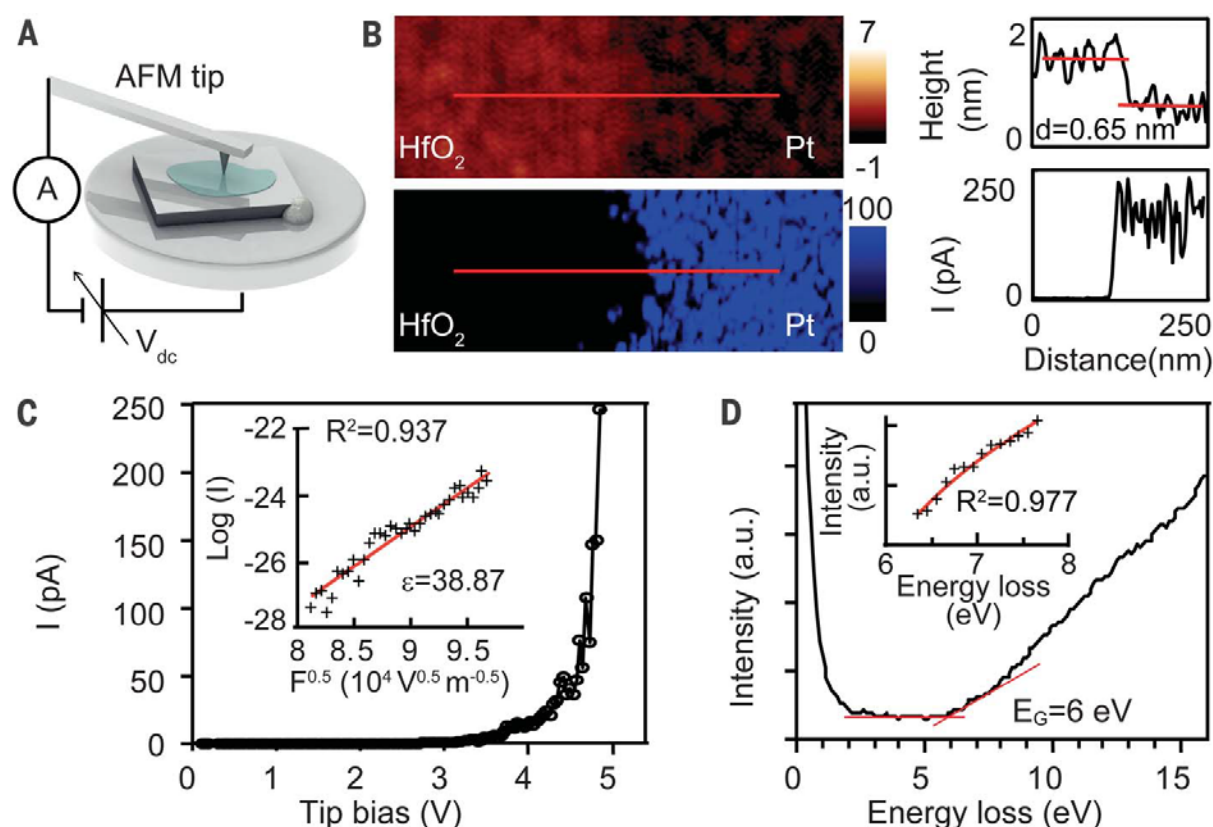


Figure 4.8. Characterization of HfO₂ as a dielectric. (A) Schematic of the peak force tunnelling AFM (PF-TUNA) setup. (B) AFM height (top) and current (bottom) maps for the edge region of an HfO₂ sample directly deposited onto a Pt-coated wafer by the exfoliation method. Both maps are 300 nm wide. The profiles at the right correspond to the regions indicated by the red lines. The HfO₂ and Pt sides are labelled. (C) Current-voltage curve measured through the HfO₂ layer. Inset: Fit to the Schottky emission model and the determined dielectric constant (see section 4.2.6). (D) Plot of the low-loss EELS spectrum, which provides an estimate of the band gap. Inset: Analysis of the nature of the band gap, indicating a direct gap ((see section 4.2.7).

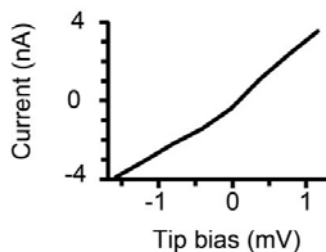


Figure 4.9. I-V curve using the PF-TUNA experimental set up shown in Fig 4.8A, measuring the I-V curve of the conductive tip when in direct contact with the platinum substrate.

4.4. Conclusion

The findings show that oxide layers on liquid metals can be manipulated by selecting appropriate alloying elements on the basis of the Gibbs free energy for oxide formation. The two methods which are used to recover the 2D nanosheets are both scalable, do not require complex equipment, and provide nanosheets either directly deposited onto substrates or as an aqueous suspension. The liquid metal serves as a solvent during the reaction. The methodology facilitated the isolation of atomically thin layers of metal oxides that do not naturally present themselves as stratified systems, providing a synthetic pathway toward an important class of 2D materials that was previously inaccessible. The underlying principles suggest that this should apply to a sizable fraction of metals, giving access to 2D crystals of many transition metal, post-transition metal, and rare earth metal oxides. Several of these metal oxides are of exceptional importance because of their various electronic, magnetic, optical, and catalytic properties.

References

1. A. Zavabeti *et al.*, liquid metal reaction environment for the room-temperature synthesis of atomically thin metal oxides. *Science* 2017, **358** (6361), 332-335.
2. D. R. Lide, *CRC handbook of chemistry and physics, internet version* (CRC Press Boca Raton, Florida, ed. 85, 2005).
3. D. Kim *et al.*, Recovery of nonwetting characteristics by surface modification of gallium-based liquid metal droplets using hydrochloric acid vapor. *ACS Appl. Mater. Interfaces* **5**, 179-185 (2013).
4. N. J. Lee *et al.*, The interlayer screening effect of graphene sheets investigated by Kelvin probe force microscopy. *Appl. Phys. Lett.* **95**, 222107 (2009).
5. A. O. Rachel, Advances in AFM for the electrical characterization of semiconductors. *Rep. Prog. Phys.* **71**, 076501 (2008).
6. J. Jahanmir, P. E. West, T. N. Rhodin, Evidence of Schottky emission in scanning tunneling microscopes operated in ambient air. *Appl. Phys. Lett.* **52**, 2086-2088 (1988).
7. S. M. Sze, K. K. Ng, *Physics of semiconductor devices*. (John Wiley & sons, ed. 2, 2006).
8. F.-C. Chiu, A review on conduction mechanisms in dielectric films. *Adv. Mater. Sci. Eng.* **2014**, 18 (2014).
9. R. A. Robie, B. S. Hemingway, J. R. Fisher, "Thermodynamic properties of minerals and related substances at 298.15 K and 1 bar (105 pascals) pressure and at higher temperatures," *U. S. Geological Survey Bulletin 1452* (United States Government Printing Office, Washington, 1978).
10. R. F. Egerton, *Electron energy-loss spectroscopy in the electron microscope*. (Springer Science & Business Media, ed. 3, 2011).
11. V. Nicolosi, M. Chhowalla, M. G. Kanatzidis, M. S. Strano, J. N. Coleman, Liquid exfoliation of layered materials. *Science* **340**, 1226419 (2013).
12. J. N. Coleman *et al.*, Two-dimensional nanosheets produced by liquid exfoliation of layered materials. *Science* **331**, 568-571 (2011).
13. T. T. Song *et al.*, The stability of aluminium oxide monolayer and its interface with two-dimensional materials. *Sci. Rep.* **6**, 29221 (2016).
14. F. A. Rasmussen, K. S. Thygesen, Computational 2D materials database: electronic structure of transition-metal dichalcogenides and oxides. *J. Phys. Chem. C* **119**, 13169-13183 (2015).
15. T. T. Song *et al.*, Graphene stabilized high- κ dielectric Y2O3 (111) monolayers and their interfacial properties. *RSC Adv.* **5**, 83588-83593 (2015).
16. K. S. Novoselov *et al.*, Electric field effect in atomically thin carbon films. *Science* **306**, 666-669 (2004).
17. D. Chandler, J. D. Weeks, H. C. Andersen, Van der Waals picture of liquids, solids, and phase transformations. *Science* **220**, 787-794 (1983).

18. X. Zhao, D. Vanderbilt, First-principles study of structural, vibrational, and lattice dielectric properties of hafnium oxide. *Phys. Rev. B*: **65**, 233106 (2002).
19. W. E. Lee, K. P. D. Lagerlof, Structural and electron diffraction data for sapphire (α -Al₂O₃). *J. Electron. Microsc. Tech.* **2**, 247-258 (1985).
20. M. A. Ballem, F. Söderlind, P. Nordblad, P.-O. Käll, M. Odén, Growth of Gd₂O₃ nanoparticles inside mesoporous silica frameworks. *Microporous Mesoporous Mater.* **168**, 221-224 (2013).
21. M. D. Dickey *et al.*, Eutectic gallium-indium (EGaIn): A liquid metal alloy for the formation of stable structures in microchannels at room temperature. *Adv. Funct. Mater.* **18**, 1097-1104 (2008).
22. G. Cossu, G. M. Ingo, G. Mattogno, G. Padeletti, G. M. Proietti, XPS investigation on vacuum thermal desorption of UV/ozone treated GaAs(100) surfaces. *Appl. Surf. Sci.* **56**, 81-88 (1992).
23. B. J. Carey *et al.*, Wafer-scale two-dimensional semiconductors from printed oxide skin of liquid metals. *Nat. Commun.* **8**, 14482 (2017).
24. D. D. Sarma, C. N. R. Rao, XPS studies of oxides of second- and third-row transition metals including rare earths. *J. Electron. Spectrosc. Relat. Phenom.* **20**, 25-45 (1980).
25. J. van den Brand, P. C. Snijders, W. G. Sloof, H. Terryn, J. H. W. de Wit, Acid–base characterization of aluminum oxide surfaces with XPS. *J. Phys. Chem. B* **108**, 6017-6024 (2004).
26. M. Kwoka *et al.*, XPS study of the surface chemistry of L-CVD SnO₂ thin films after oxidation. *Thin Solid Films* **490**, 36-42 (2005).
27. G. Hollinger, R. Skheyta-Kabbani, M. Gendry, Oxides on GaAs and InAs surfaces: An x-ray-photoelectron-spectroscopy study of reference compounds and thin oxide layers. *Phys. Rev. B*: **49**, 11159-11167 (1994).
28. Simon, P.; Gogotsi, Y., Materials for electrochemical capacitors. *Nature Materials* 2008, 7 (11), 845-854.
29. Choi, J. H.; Mao, Y.; Chang, J. P., Development of hafnium based high-k materials-A review. *Materials Science & Engineering R-Reports* 2011, 72 (6), 97-136.
30. M. L. Green *et al.*, Nucleation and growth of atomic layer deposited HfO₂ gate dielectric layers on chemical oxide (Si–O–H) and thermal oxide (SiO₂ or Si–O–N) underlayers. *J. Appl. Phys.* **92**, 7168-7174 (2002).
31. K. K. Kim *et al.*, Synthesis and characterization of hexagonal boron nitride film as a dielectric layer for graphene devices. *ACS Nano* **6**, 8583-8590 (2012).
32. S. M. Kim *et al.*, Synthesis of large-area multilayer hexagonal boron nitride for high material performance. *Nat. Commun.* **6**, 8662 (2015).
33. Cheynet, M. C.; Pokrant, S.; Tichelaar, F. D.; Rouviere, J.-L., Crystal structure and band gap determination of HfO₂ thin films. *Journal of Applied Physics* 2007, 101 (5).

Chapter 5

Green synthesis of low dimensional aluminium oxide hydroxide and oxide using liquid metal reaction media: Ultra-high flux membranes[†]

5.1. Introduction

In previous chapter, author of this thesis demonstrated liquid metals as excellent reaction solvent to produce two-dimensional oxides of the desired metals at the metal/air interface. In this chapter, the concept is furthered to synthesis low dimensional metal hydroxide and oxide hydroxide at the metal/H₂O interface. A green liquid metal based technique is presented for synthesizing 1D and 2D γ -AlOOH structures grown from the surface of galinstan at the interface with H₂O. The 1D fibres and 2D sheets grow perpendicular and parallel to the surface of the liquid galinstan, respectively, with

[†] The contents of this chapter is published in Zavabeti et al., Green Synthesis of Low-Dimensional Aluminum Oxide Hydroxide and Oxide Using Liquid Metal Reaction Media: Ultrahigh Flux Membranes, *Advanced Functional Materials*, DOI: 10.1002/adfm.201804057, 2018

large surface areas. The 1D and 2D morphology of γ -AlOOH is found to persevere when converted into γ -Al₂O₃ *via* annealing. Quantitative nanomechanical mapping (QNM) indicated that the 2D γ -AlOOH sheets feature the highest Young's modulus among oxides.¹⁻² Free-standing membranes are successfully constructed consisting of layered 2D sheets of AlOOH for separating oil-in-water emulsions and filtering Pb²⁺ ion contaminated water. Importantly, the synthesis of these membranes does not require a template, structural support, compression or sintering due to the high degree of stiffness of the structure. These membranes, which operate at extraordinary flux rates, can reduce Pb²⁺ ion contamination at a concentration that is >13 times above standard drinking water to safe levels. After completion of the nanomaterial synthesis, the galinstan can be reused for the next synthesis cycle providing a sustainable, green and low cost process. It is clearly demonstrated that after three cycles of synthesis using the same liquid metal that the quality of the products does not degrade with negligible consumption of the liquid metal. The synthesis provides a simple method for obtaining close to 100% production yield with only the need for aluminium and water as precursors and without the participation of any toxic solvents. The content of this chapter is published in *Journal of Advanced Functional Materials*⁵¹.

5.2. Experimental details

5.2.1. Alloy preparation

Galinstan is used as a base liquid metal for dissolving and alloying aluminium. Galinstan is prepared in house by melting 68.5 wt% gallium 21.5 wt% indium and 10 wt% tin in a glass beaker following previously published procedures.³ The precursor materials for galinstan (gallium 99.99%, indium 99.99% and tin 99.9%) are purchased from Roto Metals Inc.

Aluminium wire with diameter 0.58 mm, $\geq 99.99\%$ trace metals basis is procured from Sigma Aldrich. Aluminium is alloyed into the Galinstan *via* grinding using mortar and pestle. The manual grinding process is conducted rigorously for a period of 20 min. Successful alloying is observed when the surface of the alloy became clear and shiny, and the mixture is found to be free from residual metal lumps. The alloying process is conducted inside a N₂ glove box containing <2 ppm oxygen to

minimize the oxidation of the alloy. For concentrations exceeding 3.3 wt% aluminium, occasional localised solid lumps are observed.

5.2.2. *Liquid based synthesis*

During the synthesis process (Fig. 5.1a) 0.5 g of the aluminium containing liquid alloy are poured into glass vials inside a N₂ glove box. The alloy is handled inside the nitrogen atmosphere in order to minimize any oxidation that may occur prior to the beginning of the controlled experiment. DI water (2 ml) is rapidly added to the glass vials upon removal from the glovebox. The vial size is chosen to ensure that the added DI water fully covered the surface of the metal droplet, in order to maximize the interfacial reaction region. The reaction is found to immediately begin after the addition of DI water and is completed within approximately 30 min. For further characterization the sample is centrifuged at a low speed of 50 RCF for a period of 15 min to remove any metal inclusions from the sample. EDXS (Fig. 5.10) confirmed the effective removal of metal inclusions after centrifugation. The sample is then dried via heating at 80 °C. During this step the formed hydrogel transformed from a light grey colour to white with a dried appearance. The sample is then heated to 170°C for an additional 4 hours to ensure the full removal of moisture. Under these conditions bayerite is known to transform to boehmite (Equation 5.1).⁴⁹ Further drying at 200 °C for 24 hours is conducted during BET analysis. Boehmite has been found to be stable at this temperature.⁴

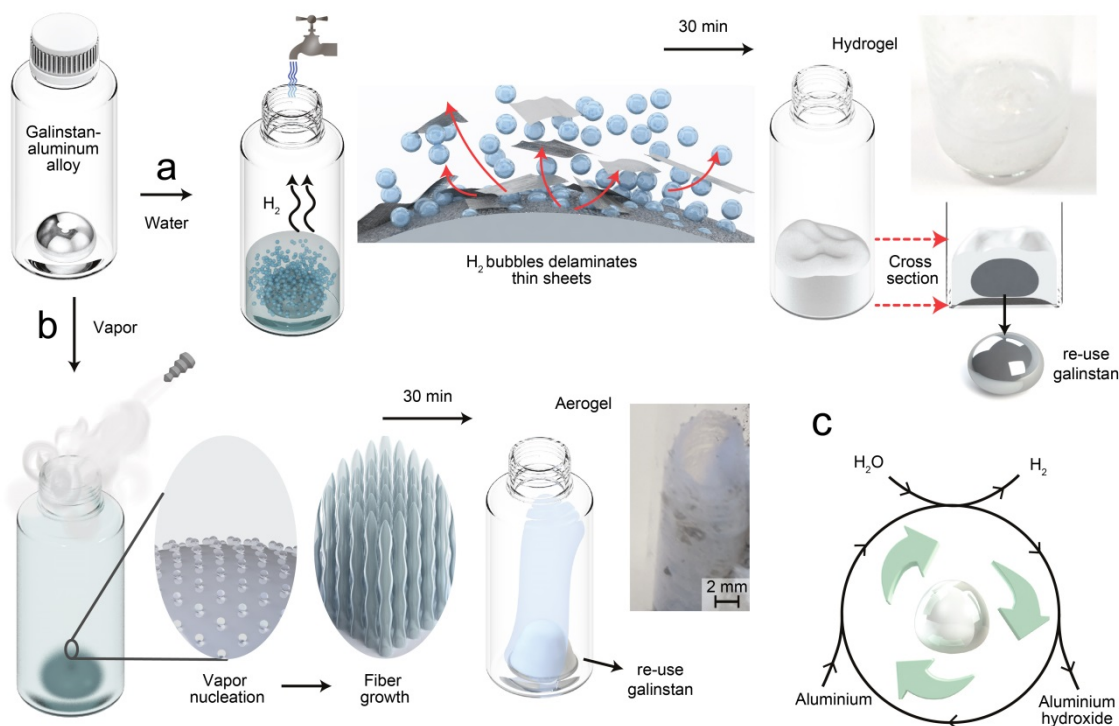


Figure 5.1. (a) DI water is added to a drop of a liquid metal alloy of galinstan-Al. After 30 min of exposure to water a hydrogel is formed. The proposed growth mechanism of the product shows that the skin is delaminated by hydrogen bubbles in the form of sheets into the DI water. The photo shows the final product from adding 2 ml DI water to 0.5 g of a 3.3 wt% galinstan-Al alloy. (b) Vapour is fed into the glass vial containing 0.5 g of 3.3 wt% galinstan-Al. After 30 min an aerogel has grown from the liquid metal. The growth mechanism shows the emergence of fibrous structures from the vapour nucleation sites. The photo shows the aerogel that has grown from the surface of the liquid metal. (c) The reaction stops after the consumption of all the aluminium but the galinstan remains unchanged after producing the aluminium hydroxides. Therefore, a green process is adopted to reuse the galinstan for the next synthesis cycle.

5.2.3. Vapour based synthesis

During this synthesis method (Fig. 5.1b) a glass vial containing 0.5 g of the prepared galinstan-aluminium alloy is prepared inside a flow through N₂ glovebox. The glass vial is then placed inside an autoclave. 0.5 ml of DI water is added to the autoclave in the space between the glass vial and the

autoclave lining (outside the glass vial containing the alloy). The autoclave packing is conducted inside the flow through glovebox to ensure minimal pre-existing oxidation products. During this process it is imperative to use a continuous flow glove box without oxygen and moisture scrubbers, since the handling of water inside an active glove box may damage the equipment. The DI water is de-gassed prior to use by bubbling nitrogen through the liquid to ensure the removal of any dissolved oxygen. The autoclave is then placed inside an oven and heated to 170°C for 30 min. The autoclave is then allowed to naturally cooled down to room temperature. HRTEM samples are prepared by sonicating a fragment of the isolated material in water for 5 min, followed by drop casting the suspension onto TEM grids.

5.2.4. Repetition, evidencing green synthesis

A 2.5g sample of galinstan is used for this experiment, aluminium is alloyed into the liquid metal via grinding, and the above described synthesis protocol is applied. Following the reaction, the formed oxide species are carefully removed and the liquid metal droplet is isolated from the bottom of the reaction vial. When each reaction is complete, the products are withdrawn from the liquid metal using a spatula. For the full recovery of the liquid metal, DI water is poured into the glass vial and any left-over hydrogel/aerogel are dispersed into the DI water *via* shaking. The aqueous suspension could then be pipetted out and re-used. The method provided a clean and complete recovery of the liquid metal and products. Visual inspection of the recovered liquid metal indicated the complete removal of the oxides. During the entire experiment care is taken to avoid the loss of any liquid metal. Following the initial synthesis cycle the liquid metal is fully dried, weighed and fresh aluminium is alloyed into the melt for the next reaction cycle. After three cycles, the weight of the used droplet is reduced by only 80 mg. A small sample of the liquid metal is smeared onto a Si wafer for SEM based EDXS analysis after the gravimetric analysis. The EDXS analysis revealed the complete removal of aluminium after the third cycle of reusing the liquid metal solvent (Fig. 5.6e and 5.11).

5.2.5. Membrane preparation

Reaction between liquid metal alloy and DI water is aggressive in the beginning and rapidly generates hydrogen bubbles. The bubbles delaminate the 2D sheets that are formed on the surface of the liquid metal. To produce thin membranes with high integrity structures, liquid metal alloy first is reacted with water for ~20 min to slow down the reaction dynamics. The liquid metal is then separated from hydrogel and is used for membrane preparation. Then surface of the liquid metal is covered with fresh DI water (~0.1 ml). A thin film of hydrogel forms on the surface of the droplet during 5-10 min (Fig. 5.12b photo on top). Then, the drying procedure which is explained in section 5.3.2 is applied. Drying process transforms hydrogel to a thin film of γ -AlOOH on surface of the liquid metal droplet. This thin film is then carefully separated from the liquid metal to avoid any metal inclusions and cracks (Fig. 5.12b photo at the bottom). An opening with diameter of ~2 mm is made on caps of a standard laboratory glass vial and a 15 ml centrifuge tube. As seen in Fig. 5.12c, a membrane is made by fixing the thin film of γ -AlOOH together with caps using silicon glue. Cap openings are aligned and the thin film of γ -AlOOH blocks the gap between the caps. All areas around the membrane are sealed using silicon glue. Glue is left to dry for 24 hours. An airway which is shown in Fig. 5.12c is punched on the upper side of the glass vial cap to allow air to exit during the filtration process. Bottom of the centrifuge tube was cut for adding the emulsions and aqueous solutions above the membrane (Fig. 5.12 c and d).

5.2.6. Emulsion preparation

Oil-in-water (50:50 %v:v) emulsion is prepared by stirring Milli-Q water and semi-synthetic engine oil with the addition of 1 v% surfactant (Tween 80).⁵ The emulsion is stirred at 1000 RPM for one hour (IKA stirrer model C-MAG HS4). The emulsion is stirred at lower rates of 250 RPM during experiments. Tween 80 surfactant which has a typical high HLB of 15 is selected to create stable oil-in-water emulsion. Tween 80 boiling point is near 100°C and evaporates with Milli-Q water during TGA analysis.

5.2.7. Annealing for conversion of γ -AlOOH to γ -Al₂O₃

Both 1D and 2D γ -AlOOH are placed on quartz slides and placed inside a thermo scientific thermolyne muffle furnace. They are then heated at 1°C/min to 550°C and kept at that temperature for 15 hours. For XRD characterization, 2D γ -Al₂O₃ is ground in a mortar and pestle and hand pressed onto a glass slide, however 1D γ -Al₂O₃ is simply pressed onto the glass slide and the softer nature of the product did not require grinding.

5.2.8. Instrumentation and characterization

A Horiba scientific LabRAM HR evolution Raman spectrometer equipped with a 50× objective lens, a 532 nm laser source (intensity 4.5 mW at the sample position) and a 1800 lines per mm grating is utilised for Raman spectroscopy. Single accumulations spectra with a duration of 200 seconds are collected. The samples are deposited on either gold or glass. Surface topography and high resolution Quantitative Mechanical Property Mapping (PeakForce QNM) measurements are conducted using a Bruker Dimension Icon AFM. The instrument features a noise floor at less than 30 pm enabling imaging at sub-nanometer resolution. The AFM is equipped with ScanAsyst® Imaging and NanoScope® software 1.8. Tips with less than 5 nm diameters are used for measurements. Peakforce QNM is fully calibrated and software is updated accordingly. Software provides high resolution Young's modulus map of the scanned area using Derjaguin–Mueller–Toporov (DMT) model. SiO₂ is used as substrate. Trenches are cut on the substrate to enable holding flakes in suspended position and avoid contribution of the substrate in measurement. Trenches are made with FEI Scios instrument explained in this section. JEOL 2100F TEM/STEM (2011) operating with 200 keV acceleration voltage is used for most of HRTEM imaging. The instrument is equipped with Gatan Orius SC1000 CCD Camera. For TEM image processing, Gatan microscopy suite 1.8.4 is used. Samples are sonicated for 5 min inside DI water to enable drop cast onto a TEM grid. 2D sheets of AlOOH are found to be beam sensitive and the electron beam reduces the crystallinity of the material. High and low resolution SEM is undertaken using a FEI Verios 460L (operating under high vacuum at 1 KV, using stage bias voltages of 1000 to 50 V and through-the-lens low energy electron detector). Patterning of SiO₂ substrates for nanomechanical mapping is performed using an FEI Scios Dual

Beam FIB/SEM (focused ion beam/scanning electron microscope) with a Gallium (Ga) beam of 7 nA. Bruker D8 Advance wide angle powder X-Ray Diffractometer is used to conduct the XRD measurements. All measurements are conducted on glass substrates. Brunauer–Emmett–Teller (BET) is carried out using a Micromeritic ASAP 2000 surface area analyser to determine surface area with nitrogen gas adsorption. Micro active v2 software which uses Hasley equations is used for data analysis. Samples are degassed under vacuum at 200°C for 24 hours using the instrument. Samples weights are measured before degassing and after degassing. In addition, all samples composition are analysed by ESDX to correct the weight for any liquid metal inclusions. Agilent ICP-MS with laser ablation capability is used to determine the concentrations of lead ions prior and after filtration. Solutions concentrations are reduced to 1:10 and are prepared to contain 2% HNO₃ before analysis with the instrument. Bruker Contour GT-I 3D optical profiler is used to measure membrane thickness.

5.3. Results and discussions

Galinstan is prepared using a thermal alloying protocol³ presented in section 5.2.1. Aluminium containing alloys are prepared using a mechanical alloying procedure adopted from the literature (see section 5.2.1).³ The prepared aluminium alloys are then exposed to aqueous environments. Figures 5.1 a and b show schematically the synthesis protocol in the liquid (water) and gas (vapour) phases, respectively. During the synthesis using liquid water, the galinstan-aluminium alloy, with an optimum ~3.3 wt% Al (the highest surface area of the product is obtained at this concentration which will be discussed later), which is still in droplet form is placed inside a glass vial with deionised (DI) water (Fig. 5.1a). The reaction is immediate and the product from this synthesis is a hydrogel as shown in the photo in Fig. 5.1a (see experimental section 5.2.2). The growth mechanism is illustrated in Fig. 5.1a in which bubbles start to form on the liquid metal surface, exfoliating the 2D sheets at the surface into the DI water. Figure 5.1b shows the synthesis schematic using water vapour. In this approach a glass vial containing the galinstan-aluminium droplet is exposed to water vapour (see experimental section 5.2.3). The product from this synthesis method features an aerogel as shown in the associated photo in Fig 5.1b. The growth mechanism is also illustrated in Fig. 5.1b in which 1D structures grow perpendicular to the surface of the liquid metal. Under these conditions water vapour nucleation

occurs on the surface of the liquid metal, creating small sites in which fibrous structures grow (Fig. 5.1b and Fig. 5.2). In a similar manner chemical vapour deposition (CVD) is also known to produce well aligned 1D structures grown from catalytic nanoisland.⁶ These structures do not delaminate from the surface of the liquid metal but grow continuously upward as shown in the images. After the completion of both methods of synthesis, when the hydrogel and aerogel are removed from the galinstan droplet, the latter remains unchanged. This indicates that in principle the galinstan can be reused for the next synthesis cycle (Fig. 5.1c). This reusability is explored (which will be discussed later) and presented in section 5.2.4.

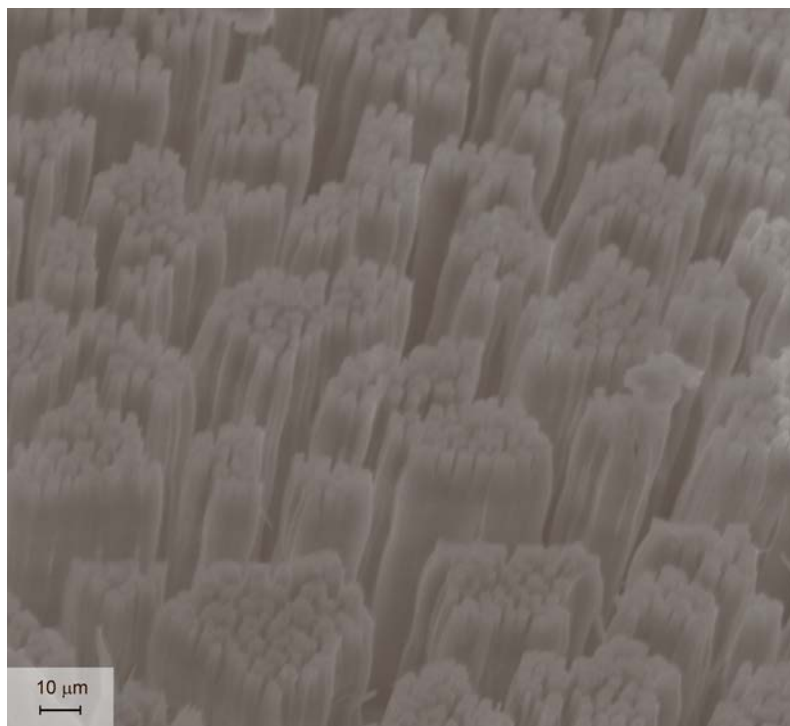
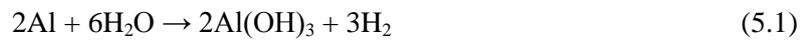


Figure 5.2. SEM image of the perpendicular growth of the fibres from the surface of the liquid metal in vapour based synthesis.

Transmission electron microscopy (TEM), scanning electron microscopy (SEM) and atomic force microscopy (AFM) images show that exposure to liquid and vapour phases produce 2D sheets (Fig. 5.3a-c) and 1D fibres (Fig. 5.3g-i), respectively. AFM images in Fig. 5.3c and 5.3j present the nominal thicknesses of 2D sheets and 1D fibres to be ~ 1.2 and ~ 2.3 nm, respectively (Fig. 5.3c and i). The 2D sheets and 1D fibres feature large lateral dimensions with their lengths extending tens of micrometers. High resolution (TEM) images together with selected area electron diffraction (SAED) and X-ray diffraction (XRD) patterns (Fig. 5.3d, e, j and k) indicate a match for the orthorhombic phase (γ -phase) of AlOOH with lattice spacings of $a = 3.700$ Å, $b = 12.227$ Å and $c = 2.868$ Å (space group *cmcm*, no. 63). Both 2D and 1D γ -AlOOH feature polycrystalline and poorly crystalline structures, respectively. Poorly crystalline boehmite is sometimes referred to as pseudo-boehmite.⁷ However, for consistency the term boehmite or γ -AlOOH is used in this chapter. The Raman spectrum

of the 2D sheets (Fig. 5.3f) shows more defined peaks than that of the 1D fibres of γ -AlOOH (Fig. 5.3l), due to the stronger crystallinity of the sheets.⁸

Equation (5.1)⁹ describes the hydrogel formation process. The obtained hydrogel is composed of a two-phase colloidal system¹⁰ containing water and α -Al(OH)₃ (bayerite). The presence of bayerite confirmed through Raman spectroscopy (Fig. 5.4) which itself is a layered material. The sample is then converted to γ -AlOOH following Equation (5.2)¹¹⁻¹² at 170°C (see section 5.2.2). Equation (5.3) represents a single step growth of 1D γ -AlOOH aerogels using the vapour synthesis route.¹³



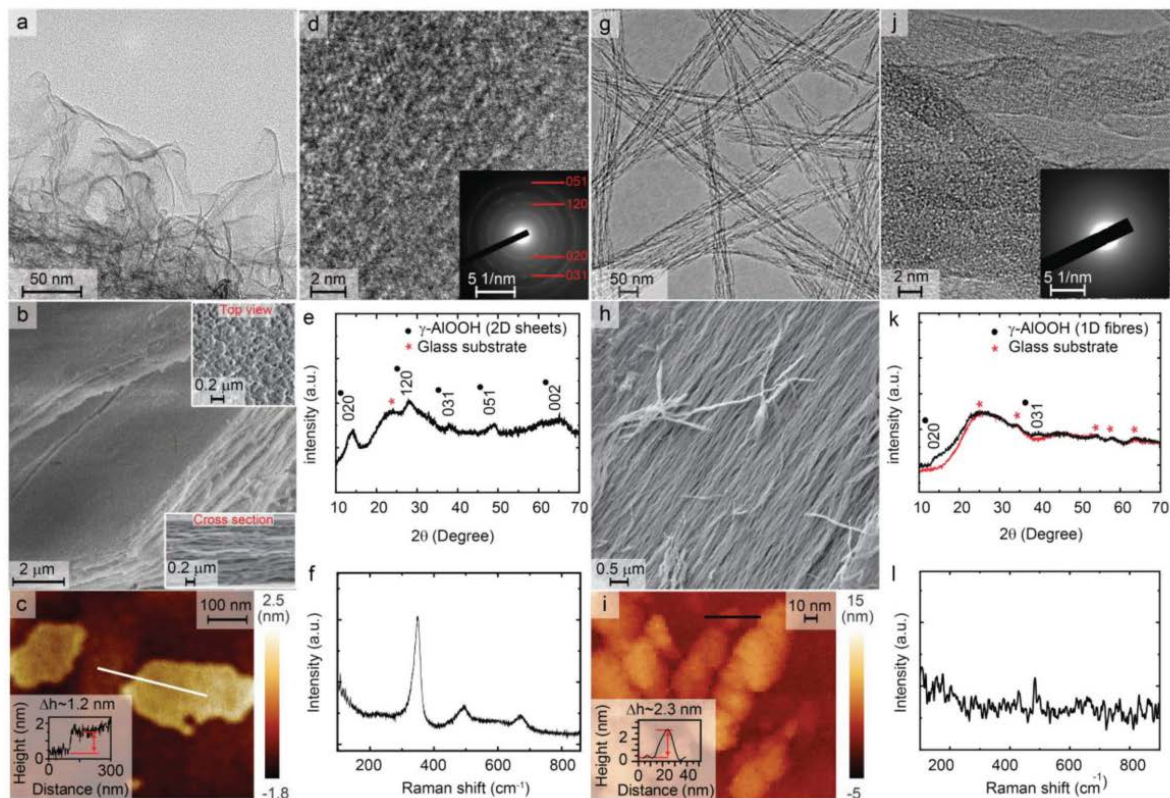


Figure 5.3. Characterization (a-f) of 2D and (g-l) 1D γ -AlOOH. (a-c) TEM, SEM, and AFM images of 2D sheets that are as-obtained products of water-based synthesis dried at 170 °C. (d-f) HRTEM with SAED (inset), XRD and Raman spectroscopy, respectively, show that the dried 2D sheets are γ -AlOOH.⁸ (h-i) TEM, SEM, and AFM images of the obtained products from vapor-based synthesis that include 1D fibers. (j-l) HRTEM with SAED (inset), XRD and Raman spectroscopy, respectively, clearly show that the 1D fibers are poorly crystalline γ -AlOOH.

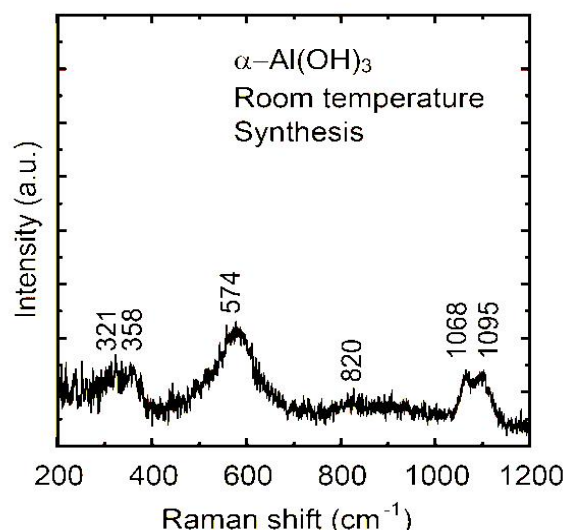


Figure 5.4. Raman spectrum of bayerite $\alpha\text{-Al(OH)}_3$ ⁸ which is produced during water based synthesis.

Boehmite is the main precursor for the synthesis of $\gamma\text{-Al}_2\text{O}_3$ as described in Equation (5.4),^{11, 14} where after being annealed at $\sim 550^\circ\text{C}$ boehmite converts to $\gamma\text{-Al}_2\text{O}_3$.¹¹ HRTEM, XRD (Fig. 5.5) confirm the conversion to the γ phase and the crystal structure matches the cubic phase. Interestingly, low resolution TEM images (Fig. 5.5 a and d) reveal that the 2D and 1D nature of the initial $\gamma\text{-AlOOH}$ is retained even after the high temperature conversion to $\gamma\text{-Al}_2\text{O}_3$. HRTEM images indicate that both 2D and 1D $\gamma\text{-Al}_2\text{O}_3$ feature polycrystalline domains (Fig. 5.5 b and e are selected to show the crystalline sections). Also, XRD of the 1D $\gamma\text{-Al}_2\text{O}_3$ sample shows sharper peaks than that of its 2D counterpart, whereby 1D $\gamma\text{-Al}_2\text{O}_3$ also presents additional [111] and [333] peaks. The 1D material is randomly oriented leading to a more complete powder pattern in comparison to the 2D material that is highly oriented leading to the missing peaks.



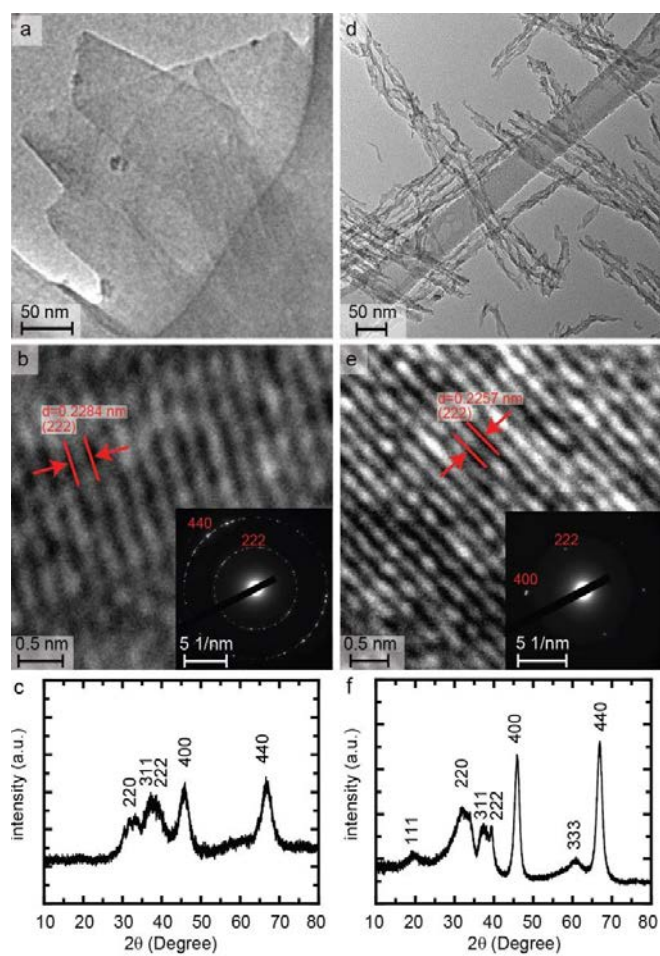


Figure 5.5. Characterization of annealed γ - Al_2O_3 . Left and right columns present 2D and 1D γ - Al_2O_3 respectively. (a and d) low resolution TEM images and (b and e) high resolution TEM images of a selected crystalline section. (c and f) show the associated XRD patterns.

Peak force quantitative nanomechanical mapping (PF-QNM) is a high-resolution AFM based technique that allows determining the Young's modulus using the Derjaguin–Mueller–Toporov (DMT) model.¹⁵⁻¹⁷ Additional information regarding this technique can be found in section 5.2.8. The 2D sheet's Young's modulus of γ -AlOOH and γ -Al₂O₃ are found to be 495.7 and 96.2 GPa, respectively (Fig. 5.6 a and b). The Young's modulus map of the 2D γ -AlOOH indicates that the synthesised boehmite sheets are a stiffer material than the subsequently synthesised γ -Al₂O₃.

High surface area γ -AlOOH and Al₂O₃ species are of tremendous technological significance due to the wide spread use of these compounds as catalyst support, polymer fillers and ion exchange filters, are increased surface areas correlate with superior performance.^{9, 18-30} Therefore the developed synthesis route for 2D γ -AlOOH is optimised towards increased surface areas. The surface area of the final product is found to depend on the alloyed concentration of aluminium as presented in Fig. 5.6 c. A substantial enhanced surface area is observed for alloys containing above 2.5 wt% of Al and the optimised alloy concentration is identified to contain ~3.3 wt% of aluminium. The overall synthesis yield for the 2D γ -AlOOH product can be increased by increasing the concentration of aluminium as demonstrated in Fig. 5.7. However, at high concentrations some bayerite somatoids are also formed (Fig. 5.8).

The optimised alloy for producing 2D γ -AlOOH is selected for the synthesis of 1D γ -AlOOH and correspondingly annealed to 1D and 2D γ -Al₂O₃. The 1D and 2D structures of γ -AlOOH have maximum measured surface areas of 906 and 654 m²g⁻¹, respectively (Fig. 5.6 c, see Fig. 5.9 for the corresponding N₂ adsorption and desorption isotherms). After annealing, the surface areas of the 1D and 2D γ -Al₂O₃ are reduced to 418 and 396 m²g⁻¹ respectively.

The recyclability of the used galinstan is of significant importance, due to the comparatively high retail price of indium and gallium. It is observed that upon the completion of the γ -AlOOH synthesis, the liquid metal solvent is found to be well separated from the product, which suggests that the liquid metal may potentially be simply reused for further reactions, provided that fresh aluminium is alloyed into the melt. Figure 5.6 d shows the surface area data for three cycles of synthesis in which galinstan

is reused (schematic is shown in Fig. 5.1c). Both the second and third synthesis cycles show an increased surface area compared to the first synthesis cycle. Gravimetric analysis revealed that ~3.2 % of the initial galinstan alloy is lost during the three synthesis cycles, with the lost liquid metal being associated with manual handling during transfer steps rather than incorporation into the product or dissolution. Energy dispersive X-ray spectroscopy (EDXS) results shown in Fig. 5.6 e indicate that the obtained product has no metal inclusions. This is achieved after a slow centrifugation step at 50 RCF for a period of 15 min which effectively removes any metal droplets. On the other hand, Fig. 5.6 f shows no aluminium on the surface of the liquid metal after three synthesis cycles, indicating complete conversion of the metallic Al into aluminium oxides and oxide hydroxides and a synthetic yield of close to 100 %. The EDXS spectra corresponding to Fig. 5.6 e and f are shown in Fig. 5.10 and 5.11, respectively.

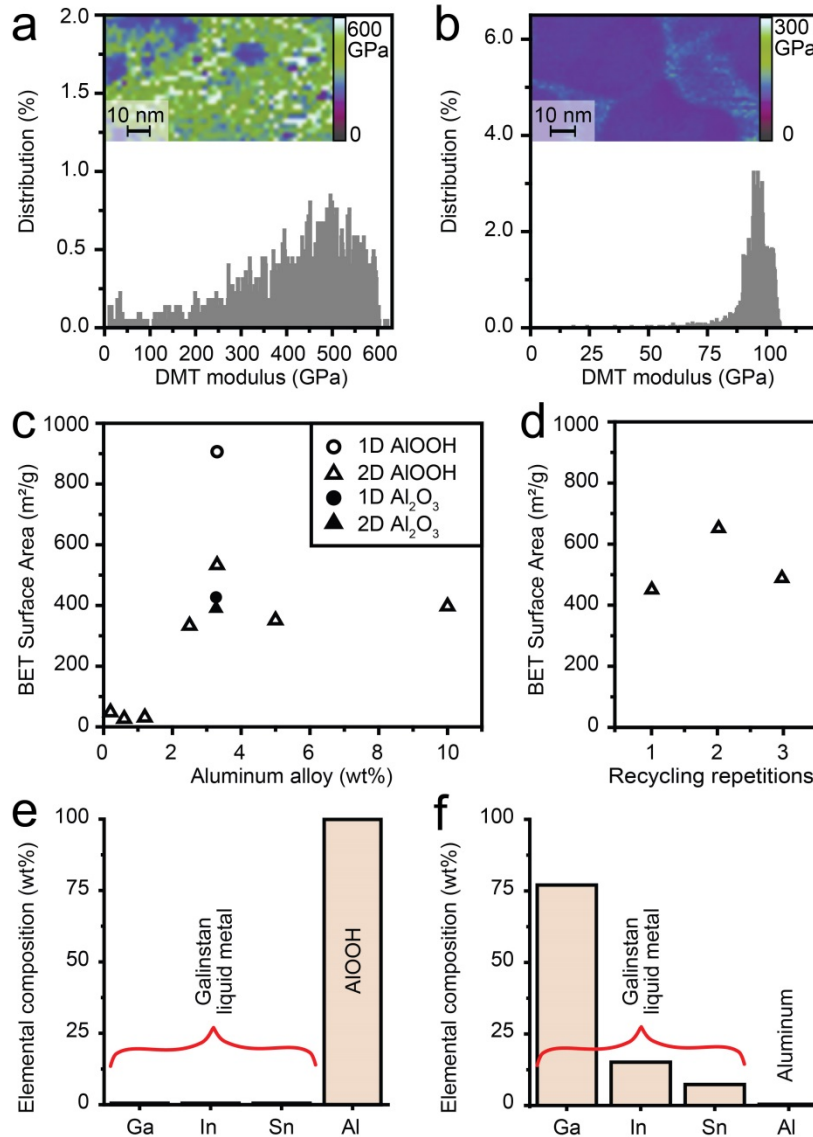


Figure 5.6. (a and b) Peak force quantitative nanomechanical mapping (PF-QNM) AFM characterization of 2D γ -AlOOH and 2D γ -Al₂O₃ flakes, respectively. Corresponding DMT modulus maps are shown above the histogram. (c) Optimisation of the BET of surface area of the 2D γ -AlOOH by changing the aluminium concentration. (d) Green synthesis shown in Fig. 5.1c with three repetitions showing an increase in surface area after two repetitions. (e) EDXS elemental composition results for the low centrifuged products demonstrate no metal inclusions and (f) no aluminium is found on the surface of the liquid metal after completion of three synthesis cycles.

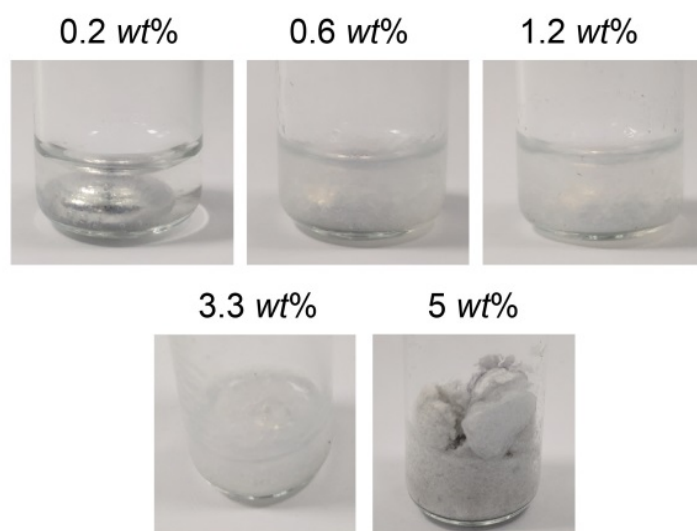


Figure 5.7. Photos of the obtained hydrogels from water based synthesis when the concentration of aluminium in the galinstan liquid metal is changed. Weight percentages of aluminium in galinstan are shown above each photo. Each photo was taken after 30 min from the start of the reaction with DI water. Products from these photos were used for BET analysis and the optimisation of surface area in Fig. 5.6.

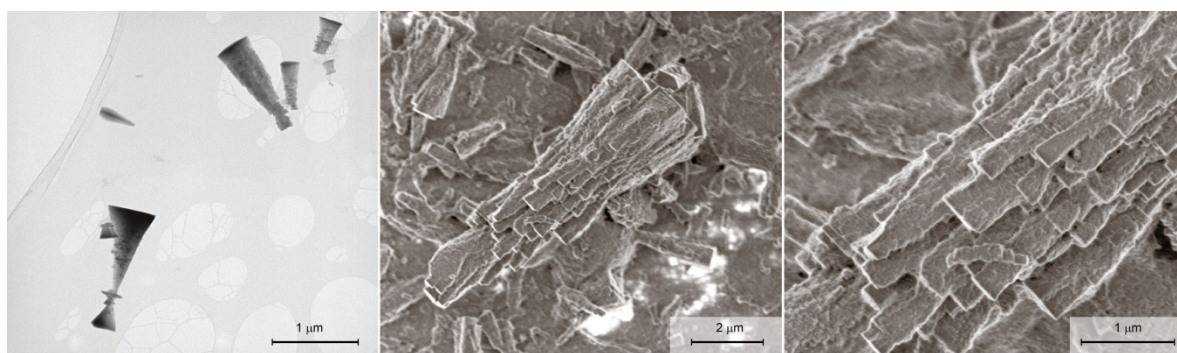


Figure 5.8. TEM image (left) and two high resolutions SEM images (right). Products from higher concentrations of aluminium (≥ 5 wt%). The structures include cone shaped bayerite somatoids¹⁰ in addition to the two-dimensional (2D) sheets.

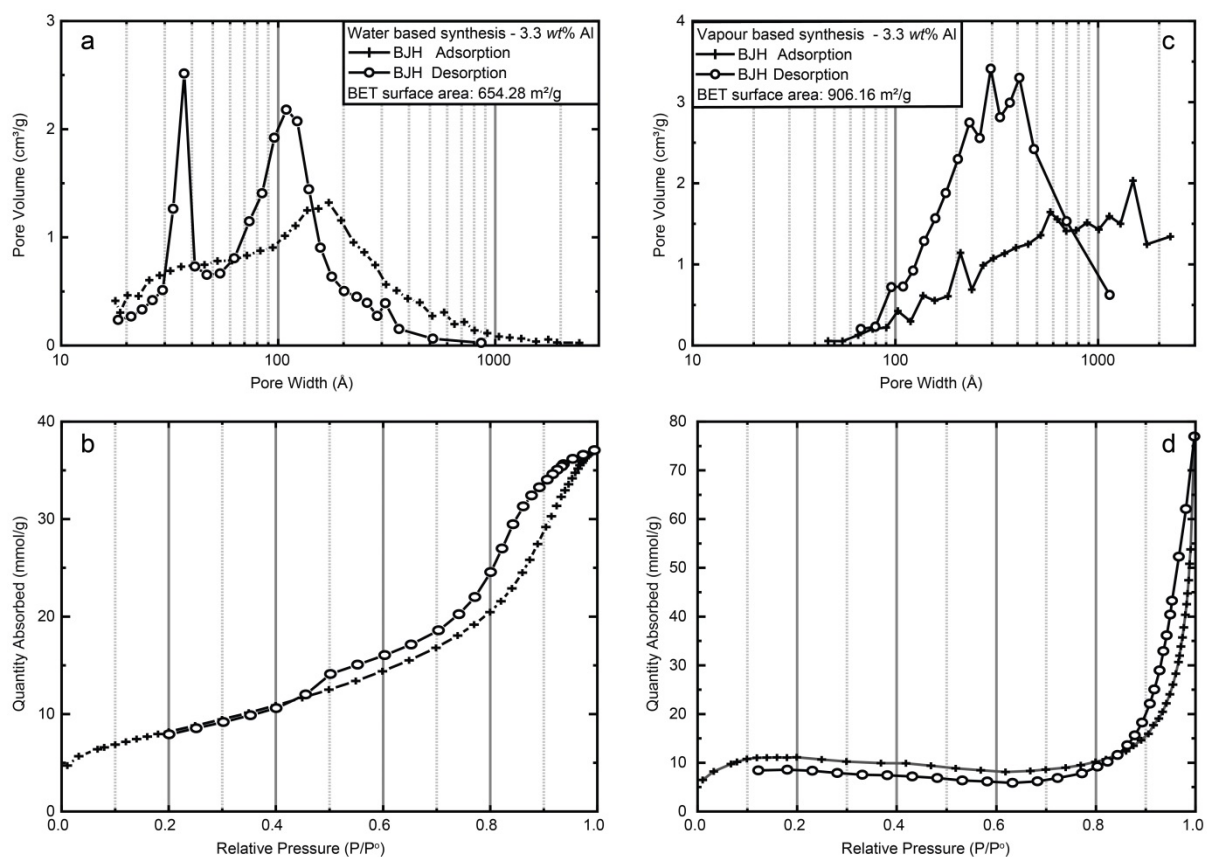


Figure 5.9. (a and b) BJH adsorption, desorption and isotherm plot of the liquid water grown boehmite shown in Fig. 5.6d (second cycle of the synthesis). (c and d) BJH adsorption, desorption and isotherm plot of the vapour grown boehmite. The surface area measurement is shown as a hollow circle in Fig. 5.6c.

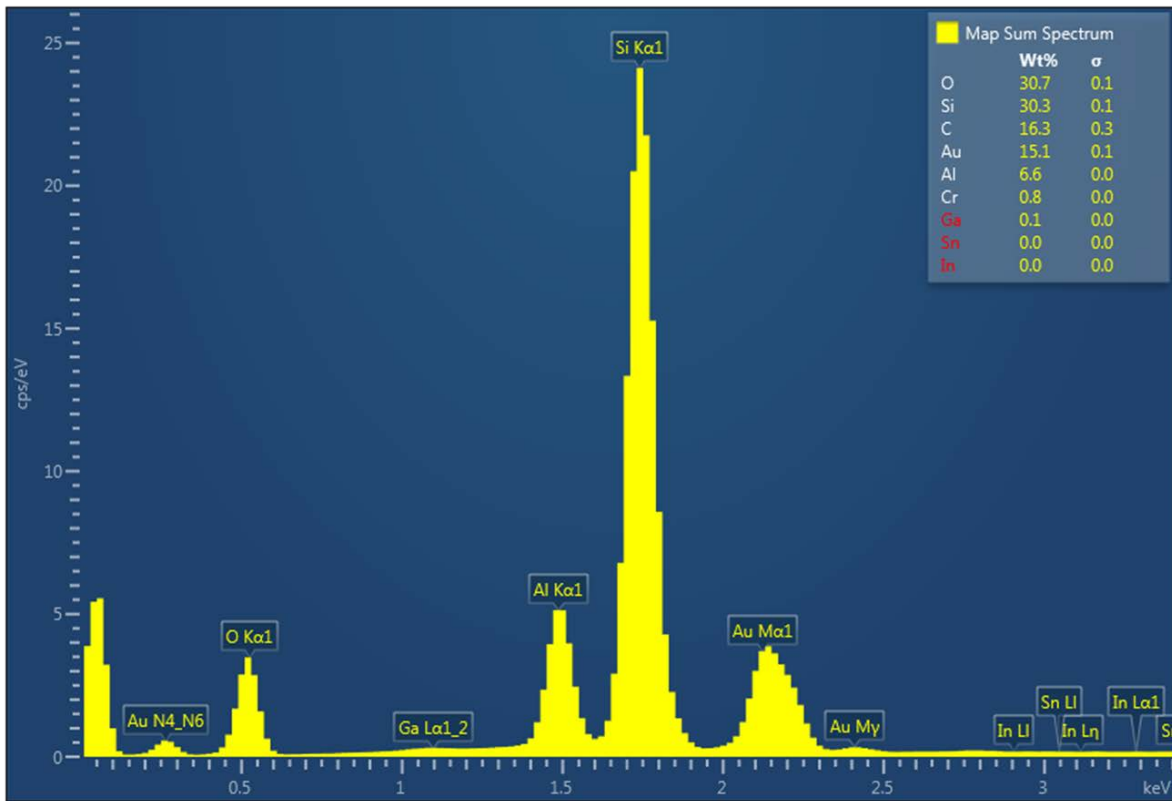


Figure 5.10. Energy-dispersive X-ray spectroscopy (EDXS) of boehmite after centrifuge (Figure 5.6e). Metal inclusions in the product such as liquid metal droplets can be removed by a slow centrifuge at 50 RCF for 15 min. EDXS results show no liquid metal inclusion in supernatant after this protocol. This sample is associated with the Raman analysis in Figure 5.3f. Substrate is Au coated Si substrate with an adhesion layer of Cr which appears in the EDXS spectrum.

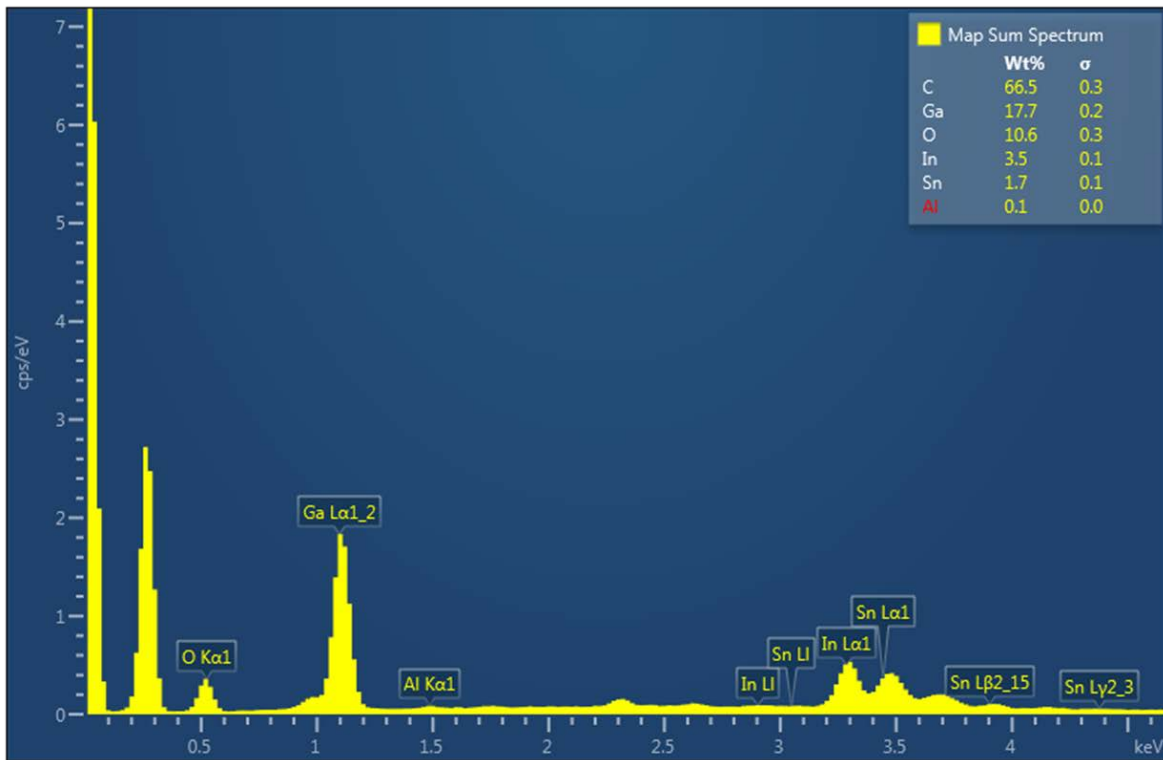


Figure 5.11. EDXS analysis of the galinstan droplet after 3 repetitions in Figure 5.6f shows no detectable aluminium on the surface of the liquid metal.

In addition to possessing a wide band gap, high surface area, excellent mechanical stiffness and room temperature stability,³¹⁻³² γ -AlOOH features further unique properties that may lead to potential industrial applications. Figure 5.12a shows 1D γ -AlOOH aerogel structure that is grown on the surface of a galinstan droplet. The grown sample is evidently mechanically stable and capable to support its own weight. The transparency to visible-light is due to the wide bandgap of boehmite and attests the absence of liquid metal inclusions.

γ -AlOOH is widely used in membrane applications due its ability to adsorb heavy metal ions (including Cr^{3+} , Pb^{2+} , Zn^{2+} , Cd^{2+} , Co^{2+} , Hg^{2+}),^{9, 18-20} sulphate²¹ and phosphates.²³ Figure 5.12b illustrates the approach to fabricate free-standing membranes from delaminated self-assembled 2D sheets of γ -AlOOH. A typical membrane has a thickness of $\sim 28.7 \mu\text{m}$. (Fig 5.12c). Details of membrane preparation are presented in the experimental section 5.2.5. To test the membrane's performance, lead ions are chosen as a water pollutant. A ~ 200 ppb solution containing Pb^{2+} ions (> 13 times above the permitted level of standard drinking water)³³ is prepared and passed through the membrane. Inductively coupled plasma mass spectrometer (ICP-MS) measurements show that the initial ~ 200 ppb concentration of Pb^{2+} is reduced to ~ 2 ppb, thereby removing 99 % of lead ions from the water and reducing the contaminant concentration to a safe drinking level (Fig 5.12c).³³ The membrane is then tested for oil/water separation for a $\sim 40:60$ %wt:wt oil-in-water emulsion as (Fig. 5.12d). Thermal gravimetric analysis (TGA) analysis of the permeate and retentate (Fig. 5.12e) revealed that the developed membrane achieved a 98.5 % rejection rate of oil. Final concentrations of permeate and retentate contain ~ 99.3 wt% water and ~ 97.24 wt% oil, respectively. Both membranes are gravity driven with water fluxes exceeding $8.4 \times 10^4 \text{ Lm}^{-2}\text{h}^{-1}\text{bar}^{-1}$. The excellent pollutant removal capabilities combined with the ease of membrane fabrication highlight the potential of the developed materials for water purification applications. Furthermore, the straightforward synthesis of the nanomaterials with minimal reaction workup and quantitative yield, combined with the direct reusability of the liquid metal, render the process to be highly attractive.

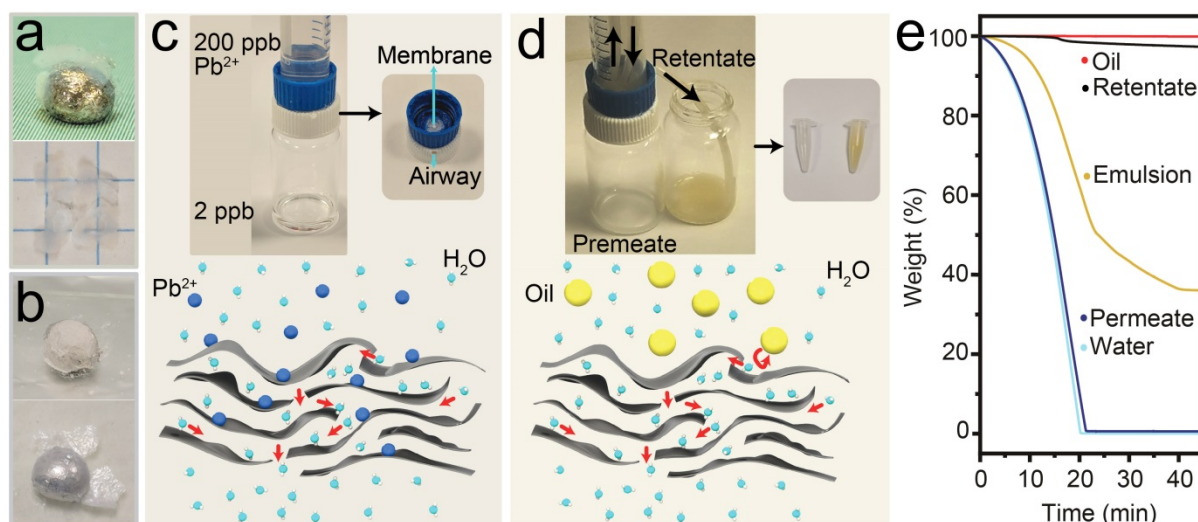


Figure 5.12. (a) Vapour grown and (b) water grown γ -AlOOH self-assembled structures, respectively. As shown in **a**, self-assembled structures grown on a galinstan droplet form 1D fibres of γ -AlOOH which result in a translucent material. The photo on the bottom of **a** demonstrates the transparency of the material on graph paper with 5×5 mm grid sizes. **b** shows the grown and delaminated layers of self-assembled 2D structures of γ -AlOOH. Synthesis process is detailed in section 5.2.5. (c) Schematic of the membrane adsorption of lead ions during filtration and a photo of the experiment and fabricated membrane (top). (d) Schematic of oil-in-water emulsion separation in which water permeates through the membrane however, oil is retained. The photo shows the experimental setup in which the arrows indicate the direction of the flow to/from a multi-channel peristaltic pump. (e) TGA analysis of the oil-in-water emulsion separation performance of the membrane is shown in **d**.

Thermodynamic considerations dictate the reaction and composition at the interface of the gallium liquid metal alloy with an oxygen environment when mixed with different metals.³ When aluminium is alloyed into galinstan, and the melt is kept in an oxidising environment, an oxide of aluminium is preferentially formed on the surface of the liquid metal. The emergence of aluminium oxide on the surface is associated to its lower Gibbs free energy of formation in comparison to gallium, indium and tin oxides.³ Here, the liquid metal is interfaced in an aqueous environment instead of an oxygen containing atmosphere to produce hydroxide and oxide hydroxide of aluminium. The synthesis

requires aluminium and water as the only precursors, with the liquid metal solvent being directly reusable for multiple batches without the need for any purification steps. The synthesised low dimensional γ -AlOOH can be converted to γ -Al₂O₃ by annealing while allowing to retain the morphology of the synthesised structures.

The γ -AlOOH materials feature interesting chemical, optical and mechanical characteristics. Both 1D and 2D γ -AlOOH have high surface areas, while the former is capable of forming highly translucent aerogels, the latter is extremely stiff. The synthesised 2D γ -AlOOH featured an excellent average surface area of ~ 532 m²/g for multiple synthesised batches, and mechanical stiffness of ~ 495.7 GPa, the highest ever reported amongst all studied 2D oxide compounds.

In addition to high surface area and mechanical stiffness, γ -AlOOH also features a layered crystal structure,⁷ and ionic adsorption properties.^{9, 18-23} The synthesised 2D γ -AlOOH sheets could be directly utilised for water decontamination applications and demonstrated to enable high performance heavy metal ion (>99% lead ion collection) and oil removal from water (>98.5% oil content separation). When compared with other 2D material based decontamination membranes, the developed 2D γ -AlOOH based membranes are capable to support a much higher water flux (> 8.4×10^4 Lm⁻²h⁻¹bar⁻¹) (ion filtration) when compared to the highest reported flux of many other layered materials such as MXene, MoS₂, WS₂ and GO, with water fluxes of 6×10^3 , 243, 730 and 71 Lm⁻²h⁻¹bar⁻¹, respectively.³⁴⁻³⁶ The extraordinarily high flux is possibility due to disordered boehmite sheets that are highly wrinkled and allow large openings for water molecules to permeate. Figure 5.9a shows the pore width obtained from BET analysis which suggests pore sizes between 3-20 nm.

It has been shown that GO membranes ion adsorption is significantly improved when combined with alumina.^{26-27, 37} For γ -AlOOH has been suggested to be due to an ion exchange mechanism as reported for phosphates²³, formation of layered double hydroxides (LDH) with divalent metal cations,³⁸ or electrostatic attraction to the hydroxyl (OH) groups on the surface for the adsorption of other types of ions.^{9, 19-21}

5.4. Conclusions

Using gallium liquid metal as a reaction environment offers a green and low cost synthesis approach for 1D and 2D structures of γ -AlOOH. In brief, a green and sustainable synthesis process for producing 1D and 2D structures of boehmite is demonstrated that can be annealed into alumina while maintaining their structural integrity. The 2D sheets are remarkably as small as one unit cell of boehmite crystal, giving the material very high surface area. The Young's modulus of the 2D sheets is very large, resulting in the highest reported mechanical stiffness for 2D oxide sheets to date.¹⁻² Membranes are produced that are able to support extraordinary fluxes for the successful separation of heavy metals and oil from water, as a result of high surface area and the wrinkled nature of the 2D sheets.

Altogether, the liquid metal reaction medium enabled the development of a facile process with close to 100 % quantitative yields for synthesizing low dimensional aluminium oxide compounds. The technique is potentially of significant industrial value, since it can be readily up-scaled, the liquid metal can be re-used, and the process requires very short reaction times and proceeds at low temperatures.

References

1. Ibrahim, I. A.; Mohamed, F. A.; Lavernia, E. J., Particulate reinforced metal matrix composites — a review. *J. Mater. Sci.* **1991**, *26* (5), 1137-1156.
2. Nicholls, J. R.; Hall, D. J.; Tortorelli, P. F., Hardness and modulus measurements on oxide scales. *Mater. High Temp.* **1994**, *12* (2-3), 141-150.
3. Zavabeti, A.; Ou, J. Z.; Carey, B. J.; Syed, N.; Orrell-Trigg, R.; Mayes, E. L. H.; Xu, C.; Kavehei, O.; O'Mullane, A. P.; Kaner, R. B.; Kalantar-Zadeh, K.; Daeneke, T., A liquid metal reaction environment for the room-temperature synthesis of atomically thin metal oxides. *Science* **2017**, *358* (6361), 332-335.
4. Peintinger, M. F.; Kratz, M. J.; Bredow, T., Quantum-chemical study of stable, meta-stable and high-pressure alumina polymorphs and aluminum hydroxides. *J. Mater. Chem. A* **2014**, *2* (32), 13143-13158.
5. Kota, A. K.; Kwon, G.; Choi, W.; Mabry, J. M.; Tuteja, A., Hygro-responsive membranes for effective oil–water separation. *Nat. Commun.* **2012**, *3*, 1025.

6. Wu, J. J.; Liu, S. C., Low-temperature growth of well-aligned ZnO nanorods by chemical vapor deposition. *Adv Mater.* **2002**, *14* (3), 215-218.
7. Iijima, S.; Yumura, T.; Liu, Z., One-dimensional nanowires of pseudoboehmite (aluminum oxyhydroxide γ -AlOOH). *Proc. Natl. Acad. Sci. U.S.A.* **2016**, *113* (42), 11759-11764.
8. Ruan, H. D.; Frost, R. L.; Klopogge, J. T., Comparison of Raman spectra in characterizing gibbsite, bayerite, diaspore and boehmite. *J. Raman Spectrosc.* **2001**, *32* (9), 745-750.
9. Gao, C.; Yu, X.-Y.; Xu, R.-X.; Liu, J.-H.; Huang, X.-J., AlOOH-reduced graphene oxide nanocomposites: one-pot hydrothermal synthesis and their enhanced electrochemical activity for heavy metal ions. *ACS Appl. Mater. Interfaces* **2012**, *4* (9), 4672-4682.
10. Wefers, K.; Misra, C., *Oxides and hydroxides of aluminum*. Alcola laboratories: 1987; Vol. 19.
11. Bell, T. E.; Gonzalez-Carballo, J. M.; Tooze, R. P.; Torrente-Murciano, L., Single-step synthesis of nanostructured γ -alumina with solvent reusability to maximise yield and morphological purity. *J. Mater. Chem. A* **2015**, *3* (11), 6196-6201.
12. Czech, E.; Troczynski, T., Hydrogen generation through massive corrosion of deformed aluminum in water. *Int. J. Hydrog. Energy* **2010**, *35* (3), 1029-1037.
13. Wang, C.; Ding, J.; Zhao, G.; Deng, T.; Liu, Y.; Lu, Y., Microfibrillar-structured Pd/AlOOH/Al-fiber for CO coupling to dimethyl oxalate: effect of morphology of AlOOH nanosheet endogenously grown on Al-fiber. *ACS Appl. Mater. Interfaces* **2017**, *9* (11), 9795-9804.
14. Tonejc, A.; Tonejc, A. M.; Bagović, D.; Kosanović, C., Comparison of the transformation sequence from γ -AlOOH (boehmite) to α -Al₂O₃ (corundum) induced by heating and by ball milling. *Mater. Sci. Eng. A* **1994**, *181-182*, 1227-1231.
15. Young, T. J.; Monclus, M. A.; Burnett, T. L.; Broughton, W. R.; Ogin, S. L.; Smith, P. A., The use of the PeakForce (TM) quantitative nanomechanical mapping AFM-based method for high-resolution Young's modulus measurement of polymers. *Meas. Sci. Technol.* **2011**, *22* (12), 125703.
16. Derjaguin, B. V.; Muller, V. M.; Toporov, Y. P., Effect of contact deformations on the adhesion of particles. *J. Colloid Interface Sci.* **1975**, *53* (2), 314-326.
17. Morales-Rivas, L.; González-Orive, A.; Garcia-Mateo, C.; Hernández-Creus, A.; Caballero, F. G.; Vázquez, L., Nanomechanical characterization of nanostructured bainitic steel: Peak Force Microscopy and Nanoindentation with AFM. *Sci. Rep.* **2015**, *5*, 17164.
18. Wei, Y.; Yang, R.; Zhang, Y.-X.; Wang, L.; Liu, J.-H.; Huang, X.-J., High adsorptive γ -AlOOH(boehmite)@SiO₂/Fe₃O₄ porous magnetic microspheres for detection of toxic metal ions in drinking water. *Chem. Commun.* **2011**, *47* (39), 11062-11064.
19. Salem, M.; Sharawy, H.; Ossman, M., Kinetics modeling and Adsorption isotherm studies for Cr(III) removal using Boehmite Nano-powder. *Int. J. Chem. Biol. Sci.* **2013**, *3*, 9-18.

20. Hota, G.; Kumar, B. R.; Ramakrishna, W. J. N. S., Fabrication and characterization of a boehmite nanoparticle impregnated electrospun fiber membrane for removal of metal ions. *J. Mater. Sci.* **2008**, *43* (1), 212-217.
21. He, T.; Xiang, L.; Zhu, S., Hydrothermal preparation of boehmite nanorods by selective adsorption of sulfate. *Langmuir* **2008**, *24* (15), 8284-8289.
22. Zhang, Y.-X.; Yu, X.-Y.; Jin, Z.; Jia, Y.; Xu, W.-H.; Luo, T.; Zhu, B.-J.; Liu, J.-H.; Huang, X.-J., Ultra high adsorption capacity of fried egg jellyfish-like γ -AlOOH(Boehmite)@SiO₂/Fe₃O₄ porous magnetic microspheres for aqueous Pb(II) removal. *J. Mater. Chem.* **2011**, *21* (41), 16550-16557.
23. Tang, W. P.; Shima, O.; Ookubo, A.; Ooi, K., A kinetic study of phosphate adsorption by boehmite. *J. Pharm. Sci.* **1997**, *86* (2), 230-235.
24. Ku, Y.; Chiou, H.-M., The Adsorption of Fluoride Ion from Aqueous Solution by Activated Alumina. *Water Air Soil Pollut.* **2002**, *133* (1), 349-361.
25. Laurent, C. J. C. M.; Billiet, H. A. H.; de Galan, L., The use of organic modifiers in ion exchange chromatography on alumina. The separation of basic drugs. *Chromatographia* **1983**, *17* (7), 394-399.
26. Kang, H.; Gongping, L.; Yueyun, L.; Ziyue, D.; Jie, S.; Wanqin, J., A graphene oxide membrane with highly selective molecular separation of aqueous organic solution. *Angew. Chem. Int. Ed.* **2014**, *53* (27), 6929-6932.
27. Xu, K.; Feng, B.; Zhou, C.; Huang, A., Synthesis of highly stable graphene oxide membranes on polydopamine functionalized supports for seawater desalination. *Chem. Eng. Sci.* **2016**, *146*, 159-165.
28. Yue-Sheng, L.; J., B. A., Preparation and characterization of high-temperature thermally stable alumina composite membrane. *J. Am. Ceram. Soc.* **1991**, *74* (1), 219-224.
29. Wu, S.; Braschler, T.; Anker, R.; Wildhaber, F.; Bertsch, A.; Brugger, J.; Renaud, P., Composite hydrogel-loaded alumina membranes for nanofluidic molecular filtration. *J. Mem. Sci.* **2015**, *477*, 151-156.
30. Yamaguchi, A.; Uejo, F.; Yoda, T.; Uchida, T.; Tanamura, Y.; Yamashita, T.; Teramae, N., Self-assembly of a silica-surfactant nanocomposite in a porous alumina membrane. *Nat. Mater.* **2004**, *3*, 337-341.
31. Singh, S. S., The formation and coexistence of gibbsite, boehmite, alumina and alunite at room temperature. *Can. J. Soil Sci.* **1982**, *62* (2), 327-332.
32. Zhou, X.; Zhang, J.; Ma, Y.; Tian, H.; Wang, Y.; Li, Y.; Jiang, L.; Cui, Q., The solvothermal synthesis of γ -AlOOH nanoflakes and their compression behaviors under high pressures. *RSC Adv.* **2017**, *7* (9), 4904-4911.

33. Edwards, M.; Triantafyllidou, S.; Best, D., Elevated blood lead in young children due to lead-contaminated drinking water: Washington, DC, 2001–2004. *Environ. Sci. Technol.* **2009**, *43* (5), 1618-1623.
34. Sun, L.; Huang, H.; Peng, X., Laminar MoS₂ membranes for molecule separation. *Chem. Commun.* **2013**, *49* (91), 10718-10720.
35. Sun, L.; Ying, Y.; Huang, H.; Song, Z.; Mao, Y.; Xu, Z.; Peng, X., Ultrafast molecule separation through layered WS₂ nanosheet membranes. *ACS Nano* **2014**, *8* (6), 6304-6311.
36. Ren, C. E.; Hatzell, K. B.; Alhabeab, M.; Ling, Z.; Mahmoud, K. A.; Gogotsi, Y., Charge- and size-selective ion sieving through Ti₃C₂T_x MXene membranes. *J. Phys. Chem. Lett.* **2015**, *6* (20), 4026-4031.
37. Joshi, R. K.; Carbone, P.; Wang, F. C.; Kravets, V. G.; Su, Y.; Grigorieva, I. V.; Wu, H. A.; Geim, A. K.; Nair, R. R., Precise and ultrafast molecular sieving through graphene oxide membranes. *Science* **2014**, *343* (6172), 752-754.
38. Wang, Q.; O'Hare, D., Recent advances in the synthesis and application of layered double hydroxide (LDH) nanosheets. *Chem. Rev.* **2012**, *112* (7), 4124-4155.
39. Abraham, J.; Vasu, K. S.; Williams, C. D.; Gopinadhan, K.; Su, Y.; Cherian, C. T.; Dix, J.; Prestat, E.; Haigh, S. J.; Grigorieva, I. V.; Carbone, P.; Geim, A. K.; Nair, R. R., Tunable sieving of ions using graphene oxide membranes. *Nat. Nanotechnol.* **2017**, *12*, 546-550.
40. O'Hern, S. C.; Boutilier, M. S. H.; Idrobo, J.-C.; Song, Y.; Kong, J.; Laoui, T.; Atieh, M.; Karnik, R., Selective ionic transport through tunable subnanometer pores in single-layer graphene membranes. *Nano Lett.* **2014**, *14* (3), 1234-1241.
41. Hu, M.; Mi, B., Enabling graphene oxide nanosheets as water separation membranes. *Environ. Sci. Technol.* **2013**, *47* (8), 3715-3723.
42. Nair, R. R.; Wu, H. A.; Jayaram, P. N.; Grigorieva, I. V.; Geim, A. K., Unimpeded permeation of water through helium-leak-tight graphene-based membranes. *Science* **2012**, *335* (6067), 442-444.
43. Huang, H.; Song, Z.; Wei, N.; Shi, L.; Mao, Y.; Ying, Y.; Sun, L.; Xu, Z.; Peng, X., Ultrafast viscous water flow through nanostrand-channelled graphene oxide membranes. *Nat. Commun.* **2013**, *4*, 2979.
44. Lee, J.; Chae, H.-R.; Won, Y. J.; Lee, K.; Lee, C.-H.; Lee, H. H.; Kim, I.-C.; Lee, J.-m., Graphene oxide nanoplatelets composite membrane with hydrophilic and antifouling properties for wastewater treatment. *J. Memb. Sci.* **2013**, *448*, 223-230.
45. Sun, P.; Zhu, M.; Wang, K.; Zhong, M.; Wei, J.; Wu, D.; Xu, Z.; Zhu, H., Selective ion penetration of graphene oxide membranes. *ACS Nano* **2013**, *7* (1), 428-437.
46. Zhang, P.; Gong, J.-L.; Zeng, G.-M.; Deng, C.-H.; Yang, H.-C.; Liu, H.-Y.; Huan, S.-Y., Cross-linking to prepare composite graphene oxide-framework membranes with high-flux for dyes and heavy metal ions removal. *Chem. Eng. J.* **2017**, *322*, 657-666.

47. Liu, G.; Han, K.; Ye, H.; Zhu, C.; Gao, Y.; Liu, Y.; Zhou, Y., Graphene oxide/triethanolamine modified titanate nanowires as photocatalytic membrane for water treatment. *Chem. Eng. J.* **2017**, *320*, 74-80.
48. Lim, M.-Y.; Choi, Y.-S.; Kim, J.; Kim, K.; Shin, H.; Kim, J.-J.; Shin, D. M.; Lee, J.-C., Cross-linked graphene oxide membrane having high ion selectivity and antibacterial activity prepared using tannic acid-functionalized graphene oxide and polyethyleneimine. *J. Memb. Sci.* **2017**, *521*, 1-9.
49. Shen, H.; Wang, N.; Ma, K.; Wang, L.; Chen, G.; Ji, S., Tuning inter-layer spacing of graphene oxide laminates with solvent green to enhance its nanofiltration performance. *J. Memb. Sci.* **2017**, *527*, 43-50.
50. Hu, M.; Mi, B., Layer-by-layer assembly of graphene oxide membranes via electrostatic interaction. *J. Memb. Sci.* **2014**, *469*, 80-87.
51. Zavanbeti, A.; Zhang B.Y.; de Castro I.A.; Ou J.Z.; Carey B.J.; Mohiuddin M.; Datta, R.S.; Xu C.; Mouritz A.P.; McConville C.F.; O'Mullane A.P.; Daeneke T.; Kalantar-Zadeh K., *Adv. Funct. Mater.* **2018**, doi:10.1002/adfm.201804057

Chapter 6

Conclusions and Future Work

6.1. Conclusions

The primary focus of this thesis is to investigate the research gaps and overcome challenges outlined in chapter 2. Objectives of this research focus on investigation of the fundamental and theoretical understanding of the surface properties of liquid metals at interface with different electrolyte types and concentrations, oxygen containing environments and water molecules.

The content of this research contributed to understanding of the changes in shapes and surface Marangoni flow of the liquid metal droplets by only changing electrolyte types and concentrations surrounding it. The concept of using liquid metals as a reaction media is further developed to produce surface oxides and oxide hydroxides with desired compositions. The naturally occurring surface oxides and hydroxides feature low dimensional material and demonstrated to be suitable material for applications in electronics and membrane technologies.

The research was organised and presented in the following three stages presented in chapters 3,4 and 5, respectively:

6.2. Stage 1

In the work presented in chapter 3, the author of this thesis fully investigated the effect of electrolytes to study of the autonomous motion of liquid metal droplets in microfluidic channels. Galinstan liquid metal feature large surface area which was shown to be a strong function of electrolytes surrounding it. These properties suggested that an adjustable surface tension gradient could be induced to a liquid metal droplet by exposing each side to two different electrolytes. A microfluidics framework to study the symmetry breaking of droplet was shown by exposing each hemisphere of a droplet to fresh supply of electrolytes. Based on the Lippmann's equations the surface tension gradient induced motion to the droplet. A mathematical model which was referred to as 'deformation ratio' is presented in this research to model the deformation of droplets. Measurements observed by this model was in good agreement with both the demonstrated mathematical model and the Lippmann's equation. The deformation occurs if droplet is retained in a recess however when droplet is free to move, it propels instead. Author of this thesis demonstrated applications of this system such as the pumping and switching. Optimum propelling conditions were measured to produce velocities that exceed 20 mm/s.

In the second distinct dynamics regiment, surface Marangoni flow was observed when electrolyte concentrations were increased. The relationship between measured surface Marangoni flow velocity and electrolyte concentrations were driven mathematically for the first time. In Marangoni flow dominant regiments, increase in Raman intensity for higher concentrations of electrolytes verified increase in the thickness of the oxide hydroxide skin. This oxide hydroxide layer which limits deformation of the droplet was optically visible and could be delaminated from surface of liquid metal.

6.3. Stage 2

In the previous stage, the effect of surface oxide hydroxide on droplet deformation and Marangoni flow was realised. In the work presented in chapter 4, the growth of surface oxides at interface with

air was investigated. The surface oxides were isolated by using two methods. In first method surface oxides were directly deposited onto a substrate *via* van der Waals (vdW) process and in second method surface oxides were collected in an aqueous suspension. Both synthesis methods were scalable and simple. The surface oxides compositions could be modified by alloying elements with more favourable Gibbs free energy for oxide formation. Galinstan liquid metal was used as a base liquid metal and other elements were added using grinding method. Amongst metals in galinstan, gallium has the most negative Gibbs free energy for oxide formation therefore other elements were selected with more favourable oxide formation energies such as hafnium, aluminium and gadolinium. Several techniques were employed to analyse the surface oxides such as atomic force microscopy, high resolution transmission electron microscopy, X-ray photoelectron microscopy and Raman. Results revealed that these oxides feature ultra-thin with thicknesses of 2.8 nm for Ga₂O₃, 0.6 nm for HfO₂, 1.1 nm for Al₂O₃, and 0.5 nm for Gd₂O₃. These naturally formed 2D oxides were consisting of a single metal oxide element, defect free with large lateral dimensions. Synthesis of a monolayer of HfO₂ is demonstrated to produce suitable material for insulating layers for applications in electronics.

6.4. Stage 3

In the previous stage, 2D metal oxides that grow at interface of liquid metal with air were investigated. The compositions of the oxides were modified by alloying elements with more favourable energy of oxide formations and isolated from the surface of liquid metal and used for applications in electronics. In chapter 5, this concept was furthered to investigate liquid metal at the interface with water molecules. Aluminium is an abundant element and its compounds have a high demand in industrial applications. This element can be mixed with gallium liquid metal alloys such as galinstan in high quantities and has more favourable reaction energies compared to the other metals used in galinstan. Galinstan-aluminium alloy was exposed to two different phases of water molecules such as vapour and liquid. Consequently, one-dimensional (1D) and 2D structures of γ -AlOOH were synthesised. 1D structures featured fibres with diameters of 2.3-2.6 nm and lateral dimensions of several microns up to 50 μ m. These structures grew perpendicular to the surface of droplet from nucleation sites of water vapour on the surface of the droplet. In contrary when water in liquid phase

was used 2D sheets grew on the surface of the liquid metal. The 2D structures featured as thin as a unit cell with large lateral dimensions of up to 50 μm . 2D sheets delaminate into the water with formation of hydrogen bubbles. After completion of synthesis galinstan liquid metal remained unchanged and the aluminium was fully consumed. Then galinstan liquid metal was reused for three cycles of synthesis with a negligible weight loss. This process presented a simple and green synthesis approach offering 100% yield without a need for incorporating any other chemicals.

Both 1D and 2D $\gamma\text{-AlOOH}$ were annealed to produce $\gamma\text{-Al}_2\text{O}_3$. TEM and SEM images clearly showed the 1D and 2D morphologies were retained during annealing process. $\gamma\text{-AlOOH}$ and $\gamma\text{-Al}_2\text{O}_3$ are of high technological and industrial importance. The surface areas of 1D and 2D morphologies of both materials measured exceeding 398 m^2/g . Quantitative nanomechanical mapping (QNM) using AFM demonstrated that the 2D morphologies of $\gamma\text{-AlOOH}$ and $\gamma\text{-Al}_2\text{O}_3$ have high mechanical stiffness with Young's modulus distributions centered at 495.7 and 96.2 GPa, respectively. In addition to high mechanical stiffness and surface areas, $\gamma\text{-AlOOH}$ adsorbs heavy metal ions. Considering these properties, free-standing aqueous membranes were made from $\gamma\text{-AlOOH}$. 2D sheets of $\gamma\text{-AlOOH}$ that formed on the surface of liquid metal did not delaminate when there were less water and aluminium left to react at the interface. When the reaction slowed down the self-assembled structures of 2D sheets restack to produce thicker layers of more than 20 μm . Due to the high mechanical stiffness these membranes did not require any structural support. The free-standing membranes were used to purify lead ion contaminated water with 13 times above the standard drinking quantities to safe levels. Membranes demonstrated to separate oil-in-water emulsions with 98.5% oil rejection rates. Membranes demonstrated extraordinary high fluxes of $8.4 \times 10^4 \text{ Lm}^{-2}\text{h}^{-1}\text{bar}^{-1}$ in a gravity driven system. High flux rates were due to the highly wrinkled structures of the self-assembled 2D sheets allowing larger opening and passages for water molecules.

6.5. Future Work

The research demonstrated in this PhD work, presents fundamental and novel outcomes which lead to opportunities for further extending the scope of the investigations. Several new intriguing pathways can be identified for future studies based on the findings of this PhD research.

6.5.1. Kinetics of the EDL

As discussed in chapter 3, when liquid metals are submerged into an electrolyte, an electrical double layer (EDL) forms on their surface. The charges that exist in the electrolyte solution are accumulated within the EDL. This stored energy is then converted into mechanical propulsion. The electrolyte-EDL system can be modelled as a resistor–capacitor (RC) circuit. The author of the thesis hypothesises that for the continuous propulsions of droplets, the EDL has several charge and discharge cycles that may be verified with the RC circuit’s time constant. Since during the propulsion, no mixing of the electrolytes is observed, therefore droplet should change shape to enable continuous propulsion (swimming). When channel length is increased, droplet propels for a longer duration. Hence, for longer channels the propulsion cycles maybe observable from the change in the velocity profile as it could be seen in Fig. 3.13. The possibility of change in shape of a droplet during propulsion has not been explored. Understanding of the droplet dynamics during self-propulsion helps enhance performances of autonomous self-propellers in applications such as drug deliveries and smart micro-actuators.

6.5.2. Marangoni flow regiment applications

The demonstrated framework in chapter 3, focuses on the development of applications in the deformation dominant regimes. However, Marangoni flow regimes also offer unique properties which can potentially be used in microfluidics applications such as autonomous soft sensors and mixers.

6.5.3. Dynamics of liquid metal marbles electrolytes

In chapter 3, the demonstrated framework requires two different types of electrolytes. However, fundamental operation of this method is based on the difference in the potential of zero charge (PZC) at each sides of a droplet. Nanoparticle coatings are shown to alter PZC of the surface of the liquid metals. When liquid metals are coated with different nanoparticles on each side, the symmetry of the droplet will be broken. According to the Lippmann's equation, the difference in PZC on each side will induce surface tension gradient and hypothetically propel droplets inside an electrolyte. Consequently, two different electrolytes will not be required for the symmetry breaking. The proposed framework to functionalise the surface of liquid metals, can potentially offer interesting applications in autonomous sensing/switching and to create sensitivity to other stimuli.

6.5.4. Synthesis of other 2D oxides using other liquid metal melts

Gallium based liquid metal alloys are used, as shown in chapter 4, to produce metal oxides of other elements with more favourable oxidation energies. However, if other metals such as indium, tin, bismuth and zinc are used as the base liquid metal reaction solvents, numerous other 2D oxides will be accessible. In addition to more variety of 2D oxides, characteristics of the synthesised 2D metal oxides such as crystal structures and electronics properties may vary from using one liquid metal solvent to the other. This allows using a specific liquid metal as a reaction solvent to enhance properties of the synthesised 2D materials in a particular application. In addition, to enhance the process technologies should be developed to automate the steps that require manual work such as alloying and large area printing.

6.5.5. Oxide formation fundamentals and growth of other non-oxide materials

There are several variables that influence the outcome of reaction on the surface of the liquid metals. Chapter 4 of this thesis investigated the Gibbs free energy of oxide formation. However, several other influencing factors related to Cabrera-Mott oxidation mechanism such as temperature, intermediate

reaction states, mobility of the ions within the surface oxide and the possibility of creating ternary oxides have not been explored. These oxides that are formed can potentially be converted to non-oxide materials such as sulphides, selenides, tellurides, pnictogens through chemical processes. Obtaining several new materials in 2D morphologies enable significant applications in development of van der Waals hetero structures, batteries, catalysis, optoelectronics, semiconductors and topological insulator based devices.

6.5.6. *Functionalised membranes*

Chapter 5 presents synthesis of free-standing membranes that are suitable for filtration of contaminated water. These membranes can further be functionalised to enhance adsorption kinetics and capacities for wide range of other sources of contaminations. Membranes' performance can be investigated for biological applications and filtration of viruses and bacteria.

6.5.7. *Low dimensional oxide hydroxides of other material*

In chapter 5, aluminium is used as a precursor. However synthesis of low dimensional hydroxides and oxide hydroxides of other metals such as lanthanides should be possible through this synthesis scheme, giving access to several other new low dimensional materials with exciting properties. These new low dimensional metal hydroxides and oxide hydroxides have significant potential applications in polymer composites, catalysis, energy storage and super capacitors.

6.6. Journal Publications

The research conducted by author of this thesis resulted in 19 first-author and co-author publications as below:

6.6.1. First-author Publications (presented in this thesis)

Ionic imbalance induced self-propulsion of liquid metals

A. Zavabeti, T. Daeneke, A. F. Chrimes, A. P. O'Mullane, J. Z. Ou, A. Mitchell, K. Khoshmanesh, K. Kalantar-Zadeh

Nature communications, vol. 7, p. 12402, **2016**.

A liquid metal reaction environment for the room-temperature synthesis of atomically thin metal oxides

A. Zavabeti, J. Z. Ou, B. J. Carey, N. Syed, R. Orrell-Trigg, E. L. H. Mayes, C. Xu, O. Kavehei, A. P. O'mullane, R. B Kaner, K. Kalantar-zadeh, T. Daeneke

Science, vol. 358, pp. 332-335, **2017**.

Green synthesis of low dimensional aluminium oxide hydroxide and oxide using liquid metal reaction media

A. Zavabeti, B. Y. Zhang, I. A. de Castro, J. Z. Ou, B. J. Carey, M. Mohiuddin, R. Datta, C. Xu, A. P. Mouritz, C. F. McConville, A. P. O'Mullane, T. Daeneke, and K. Kalantar-zadeh

Advanced Functional Materials, Doi: 10.1002/adfm.201804057, **2018**

6.6.2. Co-author Publications (not presented in this thesis)

Quasi Physisorptive Two-Dimensional Tungsten Oxide Nanosheets with Extraordinary Sensitivity and Selectivity to NO₂

H. Khan, A. Zavabeti, Y. Wang, C. J. Harrison, B. J. Carey, M. Mohiuddin, A. F Chrimes, I. Alves De Castro, B. Zhang, Y. Mohammad Sabri, S. K Bhargava, J. Zhen Ou, T. Daeneke, S, P Russo, Y, Li, K. Kalantar-zadeh,

Nanoscale, 9, 19162-19175, **2017**.

Sonication-Assisted Synthesis of Gallium Oxide Suspensions Featuring Trap State Absorption: Test of Photochemistry

N. Syed, A. Zavabeti, M. Mohiuddin, B. Zhang, Y. Wang, R. S. Datta, P. Atkin, B. J Carey, C. Tan, J. van Embden, A. SR Chesman, J. Zhen Ou, T. Daeneke, K. Kalantar-zadeh

Advanced Functional Materials, 27, 1702295, **2017**.

Degenerately Hydrogen Doped Molybdenum Oxide Nanodisks for Ultrasensitive Plasmonic Biosensing

B. Yue Zhang, **A. Zavabeti**, A. F. Chrimes, F. Haque, L. A. O'Dell, H. Khan, N. Syed, R. Datta, Y. Wang, A. S. R. Chesman, T. Daeneke, K. Kalantar-zadeh, J. Zhen Ou
Advanced Functional Materials, 28, 1706006, **2018**.

A Gallium-based Magnetocaloric Liquid Metal Ferrofluid

A. de Castro, A. F. Chrimes, **A. Zavabeti**, K. J. Berean, B. J. Carey, J. Zhuang, Y. Du, S. Dou, K. Suzuki, R. Shanks, R. Nixon-Luke, G. Bryant, K. Khoshmanesh, K. Kalantar-Zadeh, T. Daeneke,
Nano Letters, 17(12):7831-7838, **2017**.

Wafer-scale Two-dimensional Semiconductors from Printed Oxide Skin of Liquid Metals

J. Carey, J. Z. Ou, R. M. Clark, K. J. Berean, **A. Zavabeti**, A. S. Chesman, S. P. Russo, D. W. M. Lau, Z. Xu, Q. Bao, O. Kevehei, B. C. Gibson, M. D. Dickey, R. B. Kaner, T. Daeneke, K. Kalantar-Zadeh
Nature communications, vol. 8, p. 14482, **2017**.

Wafer-Scale Synthesis of Semiconducting SnO Monolayers from Interfacial Oxide Layers of Metallic Liquid Tin

T. Daeneke, P. Atkin, R. Orrell-Trigg, **A. Zavabeti**, T. Ahmed, S. Walia, M. Liu, Y. Tachibana, M. Javaid, A. D. Greentree, S. P. Russo, R. B. Kaner, K. Kalantar-Zadeh
ACS nano, 11(11):10974-10983, **2017**.

Surface Water Dependent Properties of Sulfur-Rich Molybdenum Sulfides: Electrolyteless Gas Phase Water Splitting

T. Daeneke, N. Dahr, P. Atkin, R. M. Clark, C. J. Harrison, R. Brkljača, N. Pillai, B. Y. Zhang, **A. Zavabeti**, S. J. Ippolito, K. J. Berean, J. Z. Ou, M. S. Strano, K. Kalantar-zadeh
ACS nano, 11(7), 6782-6794, **2017**.

Highly Active Two-Dimensional α -MoO_{3-x} for Electrocatalytic Hydrogen Evolution Reaction

R. Datta, F. Haque, M. Mohiuddin, B. J. Carey, N. Syed, **A. Zavabeti**, B. Zhang, H. Khan, K. J. Berean, J. Z. Ou, N. Mahmood, T. Daeneke, K. Kalantar-zadeh
Journal of Materials Chemistry A, 5, 24223-24231, **2017**.

Two dimensional PbMoO₄: A photocatalytic material derived from a naturally non-layered crystal

R. S. Datta, J. Zhen Ou, Md. Mohiuddin, B. J. Carey, B. Yue Zhang, H. Khan, N. Syed, **A. Zavabeti**, F. Haque, T. Daeneke, K. Kalantar-zadeh
Nano energy, 49, 237-246, **2018**.

Amorphous MoS_x Coated TiO₂ Nanotube Arrays for Enhanced Electrocatalytic Hydrogen Evolution Reaction

Z. Liu, X. Zhang, B. Wang, M. Xia, S. Gao, X. Liu, **A. Zavabeti**, J. Zhen Ou, K. Kalantar-Zadeh, Y. Wang

The Journal of Physical Chemistry C, 122, 24, 12589-12597, **2018**.

Evolution of 2D tin oxides on the surface of molten tin

P. Atkin, R. Orrell-Trigg, **A. Zavabeti**, N. Mahmood, M. Field, T. Daeneke, I.S. Cole, K. Kalantar-Zadeh

Chemical Communications, 54, 2102-2105, **2018**.

Two dimensional tungsten oxide nanosheets with unprecedented selectivity and sensitivity to NO₂

H Khan, A Zavabeti, JZ Ou, T Daeneke, YX Li, K Kalantar-zadeh

IEEE Sensors, INSPEC No: 17434331, **2017**

Liquid phase acoustic wave exfoliation of layered MoS₂: critical impact of electric field in efficiency

M. Mohiuddin, Y. Wang, **A Zavabeti**, N. Syed, R. S. Datta, H. Ahmed, T. Daeneke, S. P. Russo, A. R. Rezk, L. Y. Yeo, and K. Kalantar-zadeh

Chemistry of Materials, DOI: 10.1021/acs.chemmater.8b01506, **2018**.

Printing two-dimensional gallium phosphate out of liquid metal

N Syed, **A Zavabeti**, J Ou, Md Mohiuddin, N Pillai, B J Carey, B Y Zhang, R S Datta, A Jannat, F Haque, K Messalea, C Xu, S P Russo, C F McConville, T Daeneke, K Kalantar-Zadeh

Nature communications, vol. 9, p. 3618, **2018**.

Exploring electric field assisted van der Waals weakening of stratified crystals

Md Mohiuddin, N Pillai, **A Zavabeti**, N Mahmood, N Syed, R S Datta, D Jampaiah, T Daeneke, J Z Ou, K Kalantar-Zadeh

Applied Materials Today, 12, 359-365, **2018**

Bi₂O₃ monolayers from elemental liquid bismuth

K Messalea, B J Carey, A Jannat, N Syed, M Mohiuddin, B Y Zhang, **A Zavabeti**, T Ahmed, N Mahmood, E D Gaspera, K Khoshmanesh, K Kalantar-Zadeh, T Daeneke

Nanoscale 10(33), 15615-15623, **2018**